



UNIVERSITÀ
DEGLI STUDI
FIRENZE



INTERNATIONAL DOCTORATE IN ATOMIC AND MOLECULAR
PHOTONICS, CICLO XXXI

MIE RESONATORS FOR PHOTONIC
APPLICATIONS AT OPTICAL
FREQUENCIES

SETTORE SCIENTIFICO DISCIPLINARE FIS/03

Supervisors: Prof. Massimo Gurioli
Prof. Marco Abbarchi

Candidate: Simona Checcucci

Coordinator: Prof. Francesco Saverio Cataliotti

2015-2018

Mie resonators for photonic applications at optical frequencies

International Doctorate in Atomic and Molecular Photonics, XXXI cycle

Supervisors: Prof. Massimo Gurioli

Prof. Marco Abbarchi

Università degli Studi di Firenze

Laboratorio Europeo di Spettroscopia Non Lineare

Via Nello Carrara 1, Sesto Fiorentino,

50019 - Firenze, Italy

Aix-Marseille Université

Institut Matériaux Microélectronique et Nanosciences de Provence

Campus de Saint Jérôme - Case 142

Avenue Escadrille Normandie Niemen

F-13397 MARSEILLE Cedex 20, France

Reviewers: Prof. Marco Faustini, Université Pierre et Marie Curie, Paris, France

Dr. Andrea Cattoni, C2N-CNRS, Paris, France

Fuori della grazia di Dio per quella marsina stretta,
aveva invece trovato, nell'irritazione, l'animo e la forza
di ribellarvisi e di trionfarne. - *Luigi Pirandello*

Introduction

Optics and photonics are important fields which permeate not only a big branch of the scientific research but they also play a great and important role in the everyday life. The deep comprehension of these research topics, together with the ultimate control over advanced devices fabrication, allowed, in the last decades, for remarkable progresses in technology leading to a plethora of applications, such as for instance laser-based techniques or optical based communication. Thanks to this growing application potential, great efforts are being spent in finding new and pragmatic ways for manipulation of light at optical frequencies. The present thesis lies within this framework.

This work addresses several features of an emerging field of nano-photonics based on the use of dielectric Mie resonators. These devices, made by high refractive index and low losses materials, exhibit specific features in light management at the micro and nano scales, rendering them a viable alternative to conventional approaches such as plasmonic structures based on metals and photonic crystals. Such dielectric resonators are gaining ground in the photonic community and, in recent years, a plethora of applications exploiting their peculiarities have been showcased accounting for the potential of this approach. However, comparing with photonic crystals or plasmonics, this research field is still in its infancy in terms of large scale exploitation and viable methods for fabrication with bottom-up approach which can guarantee large samples with unexpensive techniques. These last features are indeed of crucial importance for transferring the research ideas to the world of applications. In this thesis we focus our study on three different, novel and alternative methods (with respect to conventional lithography-etching protocols) such as aerosol spray, sol gel dip coating and nano imprint lithography and solid state dewetting for realizing single Mie resonators as well as metasurfaces. All these approaches address the challenge of low cost and scalability.

Beside the fabrication aspects we also deeply investigate the optical response and the possible use of these systems for several different applications.

First, a glance is cast on the general properties of Mie resonators, starting from a general introduction and ending with the obtained scientific results. At the beginning is provided an overture to the physics, applications and possible fabrication techniques of Mie resonators. Far from providing an exhaustive introduction to the subject, the first part aims to escort the readers inside the topic, leaving the task to satisfy the curiosity of the interested ones to the several bibliographic references.

Afterwards, three works are presented, each of those closely related to published or submitted papers. First, it will be presented a work on titania spheres, published on *Advanced Functional Materials* with the title “Titania-based spherical Mie resonators elaborated by high-throughput aerosol spray: single object investigation”. Here, single spherical objects are implemented and investigated both theoretically (with analytical and numerical methods) and experimentally (with spectroscopic techniques). Thanks to the presence of an analytical solution of the Maxwell equation in the spherical case (the Mie problem), this first part of the thesis benchmarks real outputs and results with the theoretical case.

Later on, another and more complex structure is presented: record-size, ordered arrays of Mie resonators, still realized with titania via sol-gel dip coating and nano-imprint lithography. These metasurfaces, made of multiple pillars of different sizes form dielectric ordered matrices which exhibit from one side the typical response of Mie resonators and, from the other side, the characteristic behavior of gratings. Thanks to this feature, this structure can be exploited for different applications spanning from band-pass filters (based on the supported Mie resonances), to refractive index sensing (thanks to the increased sensitivity due to sharp Fano-like resonances). This work is currently under review.

Finally in the last part, is described a work published on *Physical Review Materials* with the title “Self-assembled antireflection coatings for light trapping based on SiGe random metasurfaces”. It is focused on the study of a random metasurface made of SiGe Mie resonators implemented via solid state dewetting-based technique, a purely bottom-up method. The meta-surface presents randomly distributed islands featuring

a large size dispersion and a high geometrical aspect ratio. It acts as an efficient anti-reflection coating in the visible and near infrared region enabling for an efficient light coupling and trapping in the underlying Si substrate.

List of publications

M. Bouabdellaoui, S. Checcucci, T. Wood, M. Naffouti, R. Paria Sena, K. Liu, C. Ruiz, D. Duché, J. Le Rouzo, L. Escoubas, G. Berginc, N. Bonod, M. Zazoui, L. Favre, L. Metayer, A. Ronda, I. Berbezier, D. Grosso, M. Gurioli and M. Abbarchi. **“Self-assembled anti-reflection coatings for light trapping based on SiGe random metasurfaces”**. In: Physical Review Materials (2018), 2 (3), pp. 035203.

S. Checcucci, T. Bottein, J.-B. Claude, T. Wood, M. Putero, L. Favre, M. Gurioli, M. Abbarchi and D. Grosso. **“Titania-based spherical Mie resonators elaborated by high-throughput aerosol spray: single object investigation”**. In: Advanced Functional Materials (2018), pp. 1801958.

S. Checcucci, T. Bottein, M. Gurioli, L. Favre, M. Abbarchi and D. Grosso. **“Multi-functional metasurfaces based on direct nano-imprint of Titania sol gels coatings”**. Accepted for publication in: Advanced Optical Materials.

S. Checcucci, P. Lombardi, S. Rizvi, F. Sgrignuoli, N. Gruhler, F. B. C. Dieleman, F. S. Cataliotti, W. H. P. Pernice, M. Agio and C. Toninelli **“Beaming light from a quantum emitter with a planar optical antenna”**. In: Light: Science & Applications (2017), 6, pp. e16245.

S. Checcucci, P. Lombardi, S. Rizvi, F. Sgrignuoli, M. Agio and C. Toninelli **“Device for the beaming of light emitted by light sources, in particular fluorescence of molecules ”**. Patent nr. 10201590234418 (2015), PCT extension nr. WO

2016166130 A1 (2016).

F. Gabelloni, F. Biccari, G. Andreotti, D. Balestri, S. Checcucci, A. Milanesi, N. Calisi, S. Caporali, A. Vinattieri **“Recombination dynamics in CsPbBr₃ nanocrystals: role of surface states”**. In: Optical Materials Express (2017), 7 (12), pp. 4367

D. Balestri, M. Petruzzella, S. Checcucci, F. Intonti, N. Caselli, F. Sgrignuoli, F. W. M. van Otten, A. Fiore and M. Gurioli **“Mechanical and Electric Control of Photonic Modes in Random Dielectrics”**. In: Advanced Materials (2019), pp. 1807274

Constructive and destructive interference

Every story ever told is the result of all the lessons experienced, the constructive ones and the destructive others.

This thesis represents for me the epitome of these two different kind of contributions, being born from the breakup of a previous collaboration. Destructive interference.

In chronological order, I would like to acknowledge Dr. Toninelli and Prof. Agio to have me shown, clearly, a bit of compromise required in a *banana republic*. Unfortunately, “marsina stretta” is not a dress I like and so I moved. Then, according to tradition, I would like to acknowledge Prof. Inguscio for believing in my determination. “Are you still here?”. “Yes, sure”. Not completely destructive interference.

And so I moved to join Prof. Massimo Gurioli’s group. Constructive interference. I will always think the world of his deep scientific knowledge and his integrity.

I would like to thank Prof. Marco Abbarchi, who supervised my thesis together with Massimo. His unrelenting enthusiasm in research and in life gave me the best working experience that I could have hoped for.

I wish also underline that this work is the fruitful result of many scientific contributions and I really had the invaluable chance to collaborate with an incredible team.

Above all, Prof. Francesca Intonti and Prof. David Grosso. They taught me, respectively, to take care of all details in a scientific experiment and to work things out when such details do not perfectly fit. Absolutely constructive interference, result of different approaches.

I will always be grateful to the young “crew” of PhD students at IM2NP of Marseille: Jean-Benoit Claude, Thomas Bottein, Agathe Bouvet-Marchand, Mohmmmed

Bouabdellaoui, Jerome Loizillon and Olivier Dalstein made the *marseillais* period the richest of my PhD.

Thanks to Dr. Niccolò Caselli, Prof. Cefe López and Prof. Alvaro Blanco for stimulating discussions at Instituto de Ciencia de Materiales de Madrid. Thanks to Prof. Anna Vinattieri for her pragmatism in physics and into things, I would have learned more from her. I wish also to acknowledge the ever present support of Dr. Giacomo Mazzamuto, Dr. Fabrizio Sgrignuoli and Dr. Francesco Biccari.

And I saved for last the most important ones to me, Dr. Pietro Lombardi and Dario Balestri. To Pietro I owe the most of what I learned to do in a lab. To him I wish to dedicate this thesis, a little sad that I didn't share this work with him. Dario still amazes me with his brilliant mind and his profound attitude: he manages bright and dark tones to completely constructive interference.

My bigger and heartfelt thanks to my **F**riends. Nicola and Pier Paolo, Eleonora, Dario, Costanza and Francesco, Sara, Coscì, Lucia, Francesco, Floris and Cate, Gabriele and Frank. They enrich all my joyful moments and they always care for me.

Thanks to my family, my parents and my brother, constantly and critically on my side: my self-confidence and my self-esteem.

Mes plus précieux remerciements à Raphaele et Thierry pour mes plus beaux souvenirs de Marseille.

To Niccolò, my never enough gratitude. For his unconditional love.

Table of contents

Introduction	i
List of publications	v
Constructive and destructive interference	vii
1 Mie resonators: an overview	1
1.1 All-dielectric nanophotonics: beyond photonic crystals and metallic nanoparticles	1
1.2 Mie resonances of dielectric nanoparticles	2
1.2.1 Directional scattering and Kerker conditions	7
1.3 Magnetic light: experimental demonstrations at optical frequencies	9
1.3.1 Dielectric Mie resonators in presence of a substrate	11
1.4 Functional nanophotonics with Mie resonators: the state of the art	15
1.4.1 Dielectric metasurfaces	15
1.4.2 Tunable and nonlinear applications	20
1.5 Outline of possible fabrication techniques	23
1.5.1 Lithography	24
1.5.2 Chemical methods	26
1.5.3 Solid state dewetting	28
1.5.4 Laser-assisted methods	29
1.5.5 Comparison between different fabrication techniques	32
1.6 Summary and conclusions	34
References	36

2	Spherical TiO₂ Mie resonators: single object investigation	47
2.1	Introduction	47
2.2	Results and discussion	49
2.3	Conclusions	58
2.4	Methods	59
	References	63
3	Multifunctional photonic devices with Titania-based metasurfaces	71
3.1	Introduction	71
3.2	Results	74
3.3	Discussion	82
3.4	Conclusion	84
3.5	Methods	85
3.5.1	Soft-NIL	85
3.5.2	Characterization	85
	References	87
4	SiGe-based Mie resonators as antireflection elements	95
4.1	Introduction	96
4.2	Solid state dewetting for SiGe-based Mie resonators	97
4.3	Optical characterization and simulations	100
4.4	Discussion	111
4.5	Conclusions	113
4.6	Methods	113
4.6.1	Samples' fabrication	113
4.6.2	Morphological characterization techniques	115
4.6.3	Spectroscopic techniques	117
4.6.4	Theoretical simulations	118
	References	120
5	Ongoing activities	127
5.1	Integrated all-dielectric photonic with perovskite nano-crystals	128
5.2	Solid state dewetting combined with soft nano-imprint transfer	131

References	135
Conclusions and prospectives	137

Chapter 1

Mie resonators: an overview

This chapter provides a general introduction to the physics, fabrication processes and applications of dielectric Mie resonators. In the beginning a brief explanation outlines the main reasons rendering these devices a fascinating and reliable method to manipulate light at micro- and nano-scales. Then, details are provided deeply describing the electromagnetic resonant modes inside Mie resonators, showing how this class of resonant particles can be located in the middle between metallic nano-particles and dielectric resonant cavities. Furthermore, this chapter addresses the state of the art of the mostly used fabrication processes, including top-down and bottom-up approaches. Finally, the last section gives a general overview of the most relevant applications involving the use of Mie resonators in photonics.

1.1 All-dielectric nanophotonics: beyond photonic crystals and metallic nanoparticles

Manipulation of light at micro and nanoscale is the purpose of an ever increasing field of optics: the nanophotonics.

Since thousands years B.C., our forefathers were used to play and interact with light, and metallic mirrors are the most evident and familiar result of their knowledge [1]. From such ancient times, great progresses in understanding the interaction of light with metallic elements have been done and devices such as optical metallic cavities arose, with physical configuration that span from simple Fabry-Perot to more exotic

geometries.

In a nutshell, nanophotonics, which basically studies the resonant behaviour of light, with its multiple and variegated configurations and applications, is a world populated by mirrors. In fact, being resonant frequencies the main topic of photonics, most of the light-interacting elements, when we are not speaking of emitters, can be simply seen as mirrors.

During the last century, this mirror-populated world has seen an increasing evolution and dielectric reflectors have joined side by side their metallic counterparts. Bragg mirrors and total internal reflection-based devices, as for instance whispering gallery resonators, are the most relevant example of such dielectric mirrors. Recently, a new and rapidly developing area of nano-optics utilizes the resonant behavior of high-index low-loss dielectric nanoparticles, the Mie resonators [2].

Located in-between photonic crystal cavities and plasmonic nanoparticles, Mie resonators offer an alternative way to enhance light-matter interaction at the nanoscale. Photonic crystals exhibit resonances with high quality factors and large modal volumes [3], while plasmonic nanoparticles are characterised by smaller quality factors and tiny modal volumes [4], but losses in metals optical cavities are a critical factor that limits their performances. This fundamental challenge can be overcome using all-dielectric nanoparticles made of high-index semiconducting materials, such as silicon, germanium or tellurium [5]. All-dielectric high-index resonators support resonances with frequency below or near the bandgap frequency of the constituent material. The distribution of the electromagnetic field of such resonances makes the high refractive-index nanoparticle behave like a magnetic dipole (first Mie resonance) and an electric dipole (second Mie resonance) [6]. This particular feature of Mie resonators opens the road to several interesting applications.

1.2 Mie resonances of dielectric nanoparticles

Light scattering and absorption by a single sphere, i.e., electromagnetic radiation, is a widely studied canonical problem encountered in both applied and theoretical sciences [7]. The sphere is one of the few three-dimensional bounded geometrical shapes

that possess a closed-form analytical solution either in the electrostatic or the electrodynamic domain. Thus, a sphere can be arguably perceived as an archetype of a scatterer for the extraction of valuable insights regarding the scattering problem by bounded objects and it is commonly used as a reference for any kind of electromagnetic scattering theory and applications [8].

The problem of light scattering by small (relative to the incident light wavelength) spherical particles can be solved thanks to the exact Mie solution of the diffraction problem [6]. Let's consider a non-absorbing dielectric sphere of radius r_0 and relative refractive index n under plane wave illumination, and assume linearly polarized light. The field scattered by the sphere can be decomposed into a multipole series, the so-called Mie's expansion, characterized by the electric and magnetic Mie coefficients a_m and b_m , respectively:

$$a_m = \frac{n\psi_m(nx)\psi'_m(x) - \psi_m(x)\psi'_m(nx)}{n\psi_m(nx)\xi'_m(x) - \xi_m(x)\psi'_m(nx)} \quad (1.1)$$

$$b_m = \frac{\psi_m(nx)\psi'_m(x) - n\psi_m(x)\psi'_m(nx)}{\psi_m(nx)\xi'_m(x) - n\xi_m(x)\psi'_m(nx)} \quad (1.2)$$

where $x = k_0r_0$, k_0 is the free-space wavenumber, and $\psi_m(x)$ and $\xi_m(x)$ are the Riccati-Bessel functions. The primes indicate derivation with respect to the arguments. In these equations a_1 and b_1 result proportional to the contribution of the electric and magnetic dipoles respectively, a_2 and b_2 to the quadrupoles, and so on. We shall find useful to write the Mie coefficients in terms of the scattering phase-shifts α_n and β_n [9]:

$$a_m = \frac{1}{2} \left(1 - e^{-2i\alpha_m} \right) = i \sin \alpha_m e^{-i\alpha_m} \quad (1.3)$$

$$b_m = \frac{1}{2} \left(1 - e^{-2i\beta_m} \right) = i \sin \beta_m e^{-i\beta_m} \quad (1.4)$$

In absence of absorption, i.e. for real n , the phase angles α_n and β_n are real, then the extinction and scattering cross sections, σ_{ext} and σ_S , respectively, have the same form [9]

$$\begin{aligned}
 \sigma_S = \sigma_{ext} &= \frac{2\pi}{k^2} \sum_{m=1}^{\infty} (2m+1) [\sin^2 \alpha_m + \sin^2 \beta_m] \\
 &= \sum_{m=1}^{\infty} [\sigma_{E,m} + \sigma_{M,m}]
 \end{aligned} \tag{1.5}$$

In the small particle limit ($r_0 \ll \lambda$) and large particle permittivities ($n \gg 1$) the extinction cross section presents characteristic sharp resonance peaks. The values of size parameter $q = nx$ at which the angles α_n and β_n are $\pi/2, 3\pi/2, \dots$, etc, define the resonance points. At each resonance, the extinction cross section is of the order of $\lambda/2$ and it is independent of either the particle size or the refractive index [9].

$$\sigma_S^{res} = \sigma_{ext}^{res} \circ \frac{2\pi}{k^2} (2m+1) \tag{1.6}$$

Asymptotically, the first resonance peak occurs when the size parameter is equal to π (i.e. $\lambda = 2nr_0$) corresponding to the magnetic dipole term of coefficient b_1 . In fig. 1.1a is shown the scattering cross section map of a non-absorbing Mie sphere as a function of the refractive index n and the size parameter, $q = n(r_0 2\pi/\lambda)$. Brightness in the colormap is proportional to σ_{ext} while color code represents the contribution of electric and magnetic dipoles to the total cross section. The RGB (Red, Green, Blue) code is formed by taking $RGB = \sigma_{E,1}R + \sigma_{M,1}G + \sigma_{res}B$, with $\sigma_{res} = \sqrt{\sigma_{ext}^2 - \sigma_{E,1}^2 - \sigma_{M,1}^2}$. The whole map is normalized to avoid over-saturation. Hence, green areas correspond to parameter ranges where the magnetic dipole contribution dominates the total scattering cross section, while red areas represent regions where the electric dipole contribution is dominating. The remaining blue-saturated areas are dominated by higher order multipoles.

To better understand the meaning of the so called dielectric and magnetic behaviour of such high refractive index particles, let's consider in the following some generalities of their scattering properties (for a deeper discussion the interested reader can have a look to the work of Garcìa-Extarri et al. [10]). When an electromagnetic wave impinges a dielectric particles, dipole moments are induced, proportional to the external (polarizing) fields, \mathbf{E} and \mathbf{B} ; the particle electric and magnetic polarizabilities α_E and

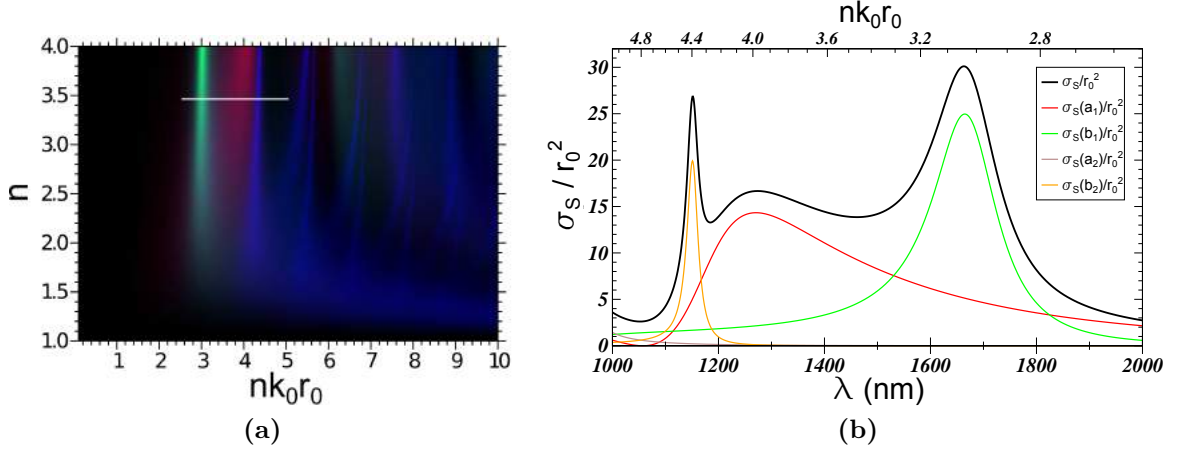


Figure 1.1: Scattering cross section map of a non-absorbing Mie sphere as a function of the refractive index n and the size parameter $q = nk_0 r_0 = n(r_0 2\pi/\lambda)$. Green areas correspond to parameter ranges where the magnetic dipole contribution dominates the total scattering cross section, while red areas represent regions where the electric dipole contribution is dominating. The remaining blue-saturated areas are dominated by higher order multipoles. Brightness in the color-map is proportional to the total cross section. The white horizontal line represent the y-range covered by **b**). **b**) Scattering cross-section σ_S versus the wavelength λ for a 230 nm Si sphere (the refraction index $n = 3.5$ is constant and real in this wavelength range). The contribution of each term in the Mie expansion is also shown. The green line corresponds to the magnetic dipole contribution. Reproduced from [10].

α_M constitute the proportionality coefficients

$$\mathbf{p} \propto \alpha_E \mathbf{E} \quad \mathbf{m} \propto \alpha_M \mathbf{B} \quad (1.7)$$

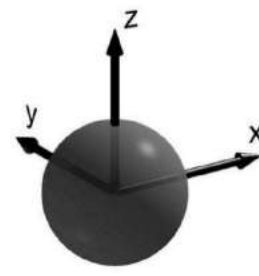
These electric and magnetic dipoles result proportional to the electric and magnetic dipole terms of eq. 1.1 and 1.2, that is a_1 and b_1 , respectively. Taking into account this relation, the scattering cross section σ_S can be expressed in terms of α_E and α_M :

$$\sigma_S = \frac{k^4}{6\pi} \left[|\alpha_E|^2 + |\alpha_M|^2 \right] \quad (1.8)$$

In the Rayleigh limit, when the size parameter $q \ll 1$, the magnetic polarizability is negligible. Very small particles always behave as point electric dipoles.

However, for particle sizes that are not extremely subwavelength (as q increases, i.e. λ decreases), there is a crossover from electric to magnetic behavior as shown by fig. 1.1b for a Si particle. Near the first b_1 -resonance, the particle essentially behaves like a

Configuration of the incident field vector



$\lambda = 1250 \text{ nm}$

$\lambda = 1680 \text{ nm}$

$\lambda = 1525 \text{ nm}$

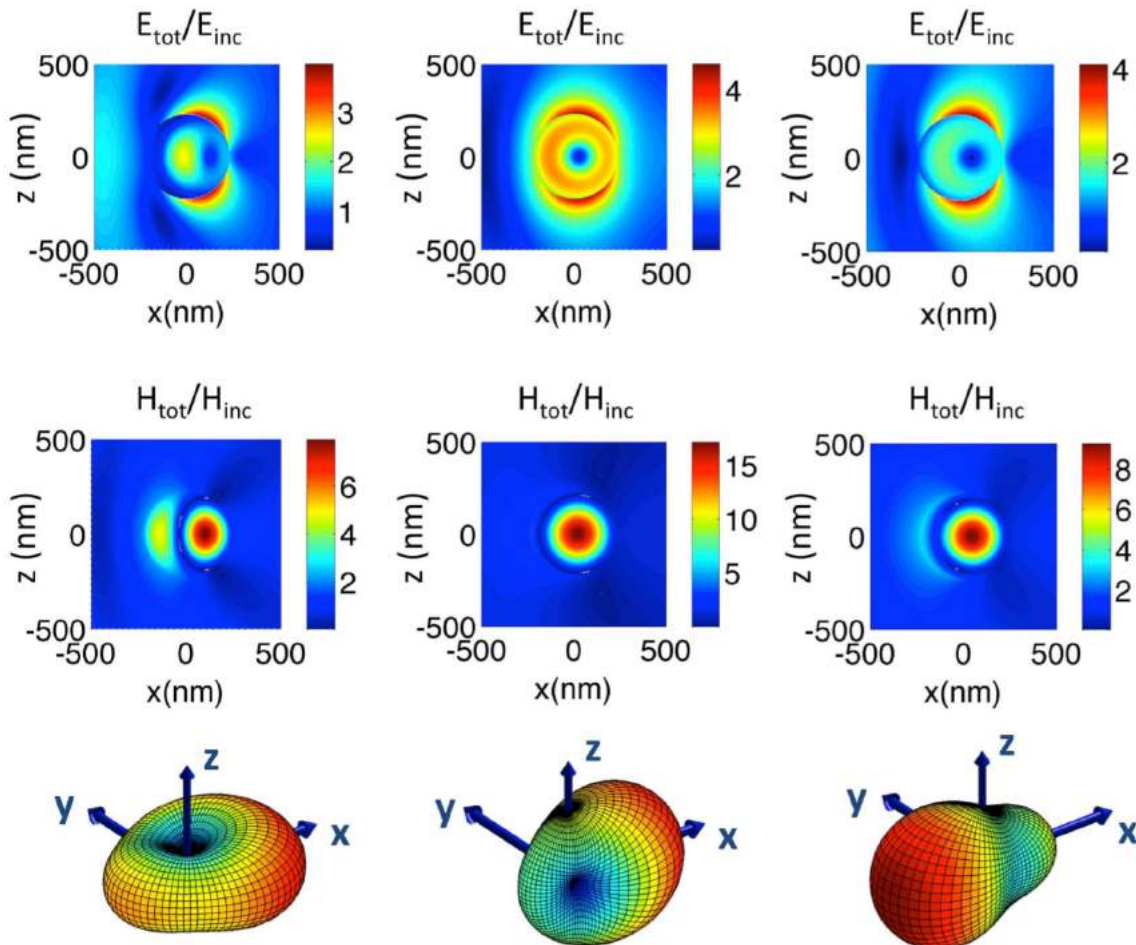


Figure 1.2: Maps for the modulus of the total electric and magnetic vectors normalized to the incoming electric and magnetic field respectively (E_{tot}/E_{inc} and H_{tot}/H_{inc}), for a Si nanoparticle of radius $r_0 = 230 \text{ nm}$ under plane wave illumination (top inset). XZ planes crossing $y = 0$ are displayed. The left and central panels correspond to $\lambda = 1250 \text{ nm}$ and $\lambda = 1680 \text{ nm}$ of the electric and magnetic resonance peaks of fig. 1.1b, respectively. The right panel corresponds to the situation where the electric and magnetic resonances contribute equally to the scattering cross section ($\lambda = 1525 \text{ nm}$). The corresponding far field scattering radiation patterns for the three wavelengths are shown in the bottom row. Reproduced from [10].

magnetic dipole (cf. fig. 1.1a). If λ decreases further, a_1 peak dominates and the sphere becomes again an electric dipole. Notice however that, due to the overlap between the electric and magnetic responses, the radiation field near the resonances does not correspond to a fully pure electric or a fully pure magnetic dipolar excitation. Yet, as seen in fig. 1.1a for the aforementioned Si sphere, the magnetic dipole contribution is, at its peak, about five times larger than the electric dipole one.

In fig. 1.2 (left and central panels) both the near field amplitude maps in the XZ plane crossing the origin of coordinates ($y = 0$ nm) and far field radiation patterns at the resonant peaks of a_1 and b_1 , (cf. fig. 1.1b), numerically calculated from the full Mie solution. The magnetic and electric nature of both resonances is clearly supported by these near and far field maps. For $\lambda = 1250$ nm (left column), the electric field map shows the typical two-lobe distribution corresponding to an electric dipole oriented along the z axis. The far-field radiation pattern also presents the characteristic donut-like shape of a dipole oriented along the z-axis with a slight distortion originated by the weaker contribution of the magnetic dipole. For $\lambda = 1680$ nm, the circular distribution of the electric field enhancement inside the sphere (mid-top panel) is a clear signature of the magnetic dipole oriented along the direction normal to the plane (y direction). The corresponding far field radiation pattern (mid-bottom panel) is also consistent.

For a general wavelength, different modes contribute to the optical response of the system. In the right panel of fig. 1.2 is shown this effect for the special case where both the electric and magnetic resonances contribute equally to the scattering cross section of the Si nanosphere (cf. fig. 1.1b). This particular situation is known as Kerker condition, as we will treat in the following section.

1.2.1 Directional scattering and Kerker conditions

The presence of strong Mie-type resonances of both electric and magnetic character opens up interesting opportunities for directional scattering effects. This can be intuitively understood from examining the emission characteristics of an electric and a magnetic oscillating dipole as displayed in fig. 1.3.

While the emission patterns of the two dipoles exhibit the same characteristic donut-shaped profile, the orientation of their electric and magnetic field components is differ-

1. Mie resonators: an overview

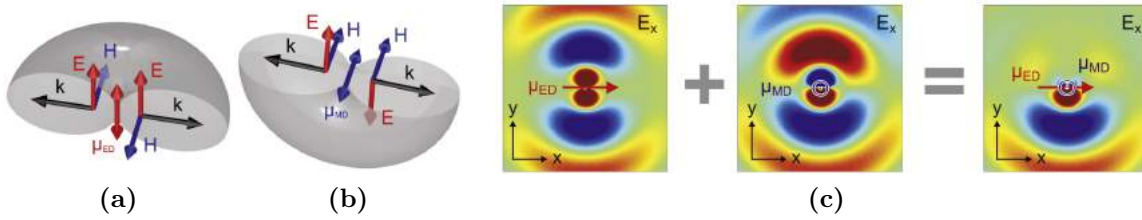


Figure 1.3: Visualization of the field polarization characteristics of **a)** an electric and **b)** a magnetic oscillating dipole. Reprinted from [11]. **c)** Illustration of how the in-phase superposition of an electric and a magnetic dipole source with the same frequency leads to constructive interference in one direction and to destructive interference in the opposite direction. Reprinted from [11].

ent (see figs. 1.3a and 1.3b: for the electric dipole, the electric fields of light propagating in opposite directions are oriented parallel and the magnetic fields are oriented antiparallel. For the magnetic dipole, the situation is the converse. Thus, by superimposing a crossed electric and magnetic dipole oscillating at the same frequency and in phase, the emitted fields interfere constructively in one direction and destructively in the opposite direction. This is illustrated in fig. 1.3c showing two-dimensional finite-difference time-domain simulations of the x-polarized electric field component of an individual x-polarized electric dipole (left), of an individual z-polarized magnetic dipole (middle), and of the superposition of both dipoles (right). Such a crossed electric and magnetic dipole source is called a Huygens source [12].

By analogy, as we have seen in the previous section, directional scattering from a nanoparticle exhibiting both electric and magnetic dipolar response can be established, since such particles exhibit in the far field a dipole-like behavior. When the electric-like and magnetic-like scattering amplitudes are equal, light is scattered in forward direction, whereas in backward direction the scattered fields interfere destructively. It's important to notice that the direction of this scattered light totally depends from the direction of the impinging light, being the orientation of the induced dipole moments inside the particle determined by the electric and magnetic incident fields. This phenomenon, known as first Kerker condition [13], was experimentally found at optical frequencies for nanoparticles composed of silicon [14] and gallium arsenide [15].

Analogously, a minimum of scattered field in the forward direction is predicted by the second Kerker condition and a zero-forward scattering is reached if some degree of

absorption is present in the scatterer. As the resonances are dispersive, different conditions for forward- and backward-scattered light can be fulfilled at different wavelengths for the same nanoparticle. Therefore, nanoparticles with both electric and magnetic response show different colors depending on the direction from which they are observed [14].

1.3 Magnetic light: experimental demonstrations at optical frequencies

As discussed in the previous section, in the case of lossless and dielectric materials, their scattering properties depend only on two parameters: the refractive index n and a size parameter q that is proportional to the ratio between the nanoparticle radius r_0 and the wavelength of light λ . This is clearly shown in fig. 1.1a, where the scattering cross section is reported as a function of these two parameters, n and q . In this map, one can easily find that, for the same size parameter, the scattering cross section and then the scattering efficiency, increases while increasing the refractive index of the nanoparticle and resonances became sharper and brighter. It is not, therefore, surprising that the first experimental demonstrations of Mie resonances in dielectric materials came for particles working at gigahertz frequencies, where materials with extremely high refractive index up to several tens of refractive index units (RIU) exist [16].

Experimental observation of both electric and magnetic resonances in dielectric particles at optical frequencies (mid-infrared) was reported in the work by Schuller et al. for silicon carbide microrods [17]. Later, dielectric and semiconductor microrods and nanorods were observed to exhibit scattering resonances in the visible and near-IR spectral range (see, e.g., [18–20]). It was also theoretically pointed out [10, 21] that silicon nanospheres with sizes ranging from 100 to 300 nm support strong magnetic and electric dipole scattering resonances in the visible and near-IR spectral range. Although silicon is not a completely loss-free material, its absorption in the visible spectrum is much lower than that of metals, making it a good material for the study of Mie resonances. An experimental demonstration of electric and magnetic dipole

1. Mie resonators: an overview

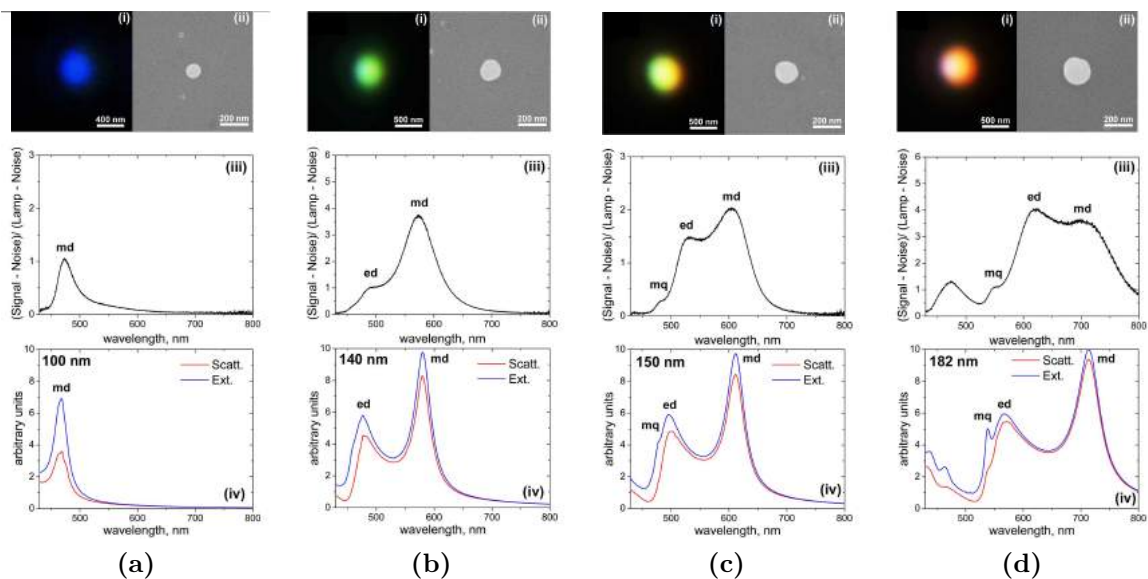


Figure 1.4: Close-view dark-field microscope (i) and SEM (ii) images of the single nanoparticles selected on the sample. (iii) Experimental dark-field scattering spectra of the nanoparticles. (iv) Theoretical scattering and extinction spectra calculated by Mie theory for spherical silicon nanoparticles of different sizes in free space. Corresponding nanoparticle sizes are defined from the SEM images (ii) and noted in each figure. **a)** to **d)** correspond to nanoparticles of 100 nm, 140 nm, 150 nm and 182 nm diameters, respectively. (Reprinted from [23].)

resonances at visible wavelengths was first reported for spherical Si nanoparticles by Evlyukhin [22] and Kuznetsov [23]. In these works, they show how silicon spheres, whose diameters span over hundreds of nanometers, can support and tune resonances which are related to the 2^m -pole terms of the scattered magnetic field (eq. eq. (1.2)) predicted by Mie theory.

In both works, scattering spectra from Si nanoparticles of various sizes are collected and compared to the dimensions of the spheres and the corresponding theoretical predictions from Mie theory. Thanks to the analytical Mie solution for scattered field, the observed spectra can be split into separate contributions of different multipole modes and a clear picture of the field distribution inside the particle at each resonance maximum comes. In fig. 1.4 is shown a complete analysis done for different particles' sizes, with experimental and theoretical scattering spectra. According to this analysis the first strongest resonance of these nanoparticles appearing in the longer wavelength part of the spectrum corresponds to magnetic dipole response (md). Magnetic dipole resonance is the only peak observed in the visible spectral range for the smallest

nanoparticles (fig. 1.4a). At increased nanoparticle size (fig. 1.4b-1.4c) electric dipole (ed) resonance also appears at the blue part of the spectra, while magnetic dipole shifts to the red. For relatively small nanoparticles, the observed colour is mostly defined by the strongest resonance peak and changes from blue to green, yellow, and red when magnetic resonance wavelength shifts from 480 nm to 700 nm (fig. 1.4a-1.4d).

To refer to these magnetic scattering resonances at visible frequencies, Kuznetsov et al. coined the term “magnetic light”.

The visible differences between experimental and theoretical spectra are ascribed to the presence of silica substrate, which is not taken into account in the simple Mie theory solution shown in fig. 1.4 (iv). As pointed out in ref. [24] electric and magnetic dipoles exhibit different behaviours in presence of a substrate: shows the distribution of the radiation pattern of horizontal electric and magnetic dipoles above a high-permittivity substrate and reveals that magnetic dipole radiates mostly to free space, while electric dipole radiates mostly into the substrate. Moreover, Refs.[25, 26] evince that the electric polarizability of the sphere is modified in the presence of the substrate, resulting in a red shift of the measured electric dipole resonance (with respect to the Mie theory solution in free space). This phenomenon is known as the “surface dressing effect”.

1.3.1 Dielectric Mie resonators in presence of a substrate

The problem involving the presence of a substrate is a main topic when considering dielectric Mie-type optical resonators, since most of practical applications require particles placed on a surface. Moreover, in most cases, strong interaction to the substrate is even desired (e.g. absorption in photodiodes [27], solar cells [28, 29], etc.). This interaction with the substrate strongly influences the resonant behavior, as well as the interaction between the magnetic and electric resonances.

The study by van de Groep et al. [30] highlights how the presence of a substrate influences the resonant properties of dielectric Mie resonators, as well as the interplay between the different eigenmodes. This analysis is performed in relation to the particle’s shape: a cylinder, a sphere and a cube are taken as examples. The refractive index of the substrate n_{sub} is varying from 1 RIU (which corresponds to a dielectric resonator in air) to 3.5 RIU, while as refractive index of the particle n_{part} is taken the refractive

1. Mie resonators: an overview

index of silicon at visible and infrared frequencies. Scattering properties are given by looking at the normalized scattering cross section (scattering cross section normalized to geometrical cross section) $Q_{scat} = \sigma_{scatt}/\sigma_{geo}$.

Figure 1.5a shows Q_{scat} for a Si cylinder with $d = 100$ nm and $h = 100$ nm on a semi-infinite substrate with an index in the range $1 \leq n_{sub} \leq 3.5$, varying in steps of 0.25 RIU. Three characteristic features can be observed. First, increasing n_{sub} from 1 to 3.5 gradually broadens the resonance peaks (due to an increasing of the possible radiative states) and causes the ED and MD peaks to overlap spectrally, such that the ED mode becomes a shoulder of the MD mode for high n_{sub} . For $n_{sub} > 2.25$, the ED is no longer visible as a separate peak. Second, a significant increase in Q_{scat} is observed for increasing n_{sub} , which is attributed to the increase in the local density of states (LDOS) at the position of the particle. Third, a small red-shift is observed with increasing n_{sub} : $\lambda_{MD} = 499$ nm for $n_{sub} = 1$ and $\lambda_{MD} = 515$ nm for $n_{sub} = 3.5$. This is caused by the index experienced by the near-field of the resonance. This small shift of only 16 nm is in sharp contrast with the dramatic 600 nm red-shift observed for a plasmonic dipolar resonance of a similar cylinder made of Ag [31]. This contrast is a direct result of the different nature of the resonance. While in plasmon resonances most light is concentrated at the interface (in direct contact with the substrate), in case of dielectric particles most light is concentrated inside the resonator, making it less sensitive to substrate index.

To investigate the influence of particle shape, fig. 1.5b shows Q_{scat} as a function of wavelength for the same cylinder as in 1.5a (red), a $d = 114$ nm sphere (green), and a cube with sides of length $l = 92$ nm (blue). These particles have the same volume, are all made of Si and the geometries are shown below (fig. 1.5a and fig. 1.5b). The dashed lines in fig. 1.5b correspond to particles in air, the solid line to particles on a semi-infinite substrate with $n_{sub} = 3.5$. Note that the sphere is sticking 7 nm into the substrate (center is at 50 nm height above the substrate) to prevent unphysical hot spots at the infinitely sharp contact area (see sketched geometry). Figure 1.5b shows that both in air and on a substrate, the shape of the particle has only a small influence on the resonance wavelengths of the ED and MD modes. Both resonances are supported for all shapes, and the cylinder proves to be the most efficient scatterer.

1.3 Magnetic light: experimental demonstrations at optical frequencies

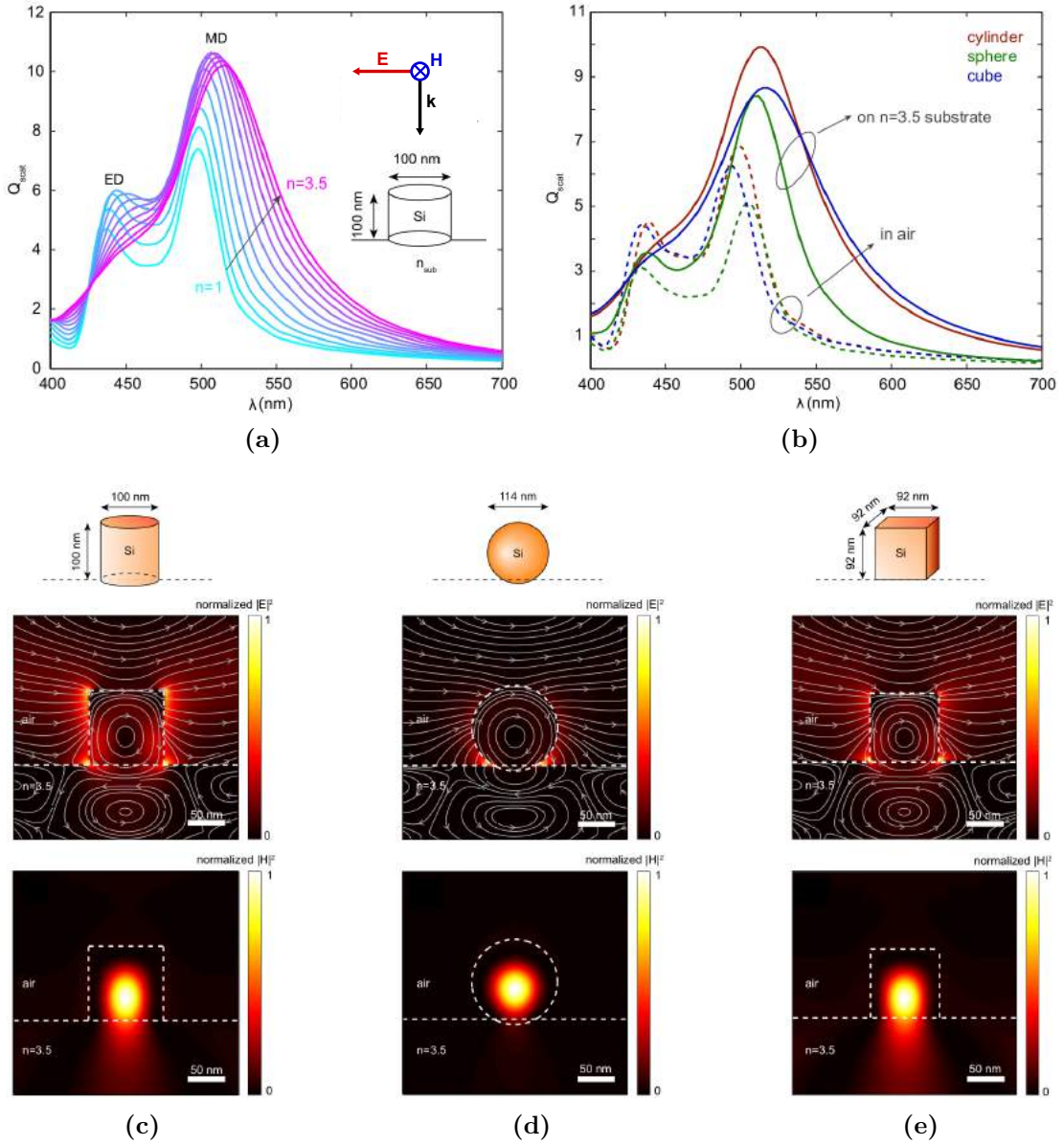


Figure 1.5: **a)** Q_{scat} as a function of wavelength for a Si cylinder with $h=100$ nm, $d=100$ nm, on a semi-infinite substrate with $1 \leq n_{sub} \leq 3.5$, in index steps of 0.25. The geometry is shown as an inset, as the configuration of excitation. **b)** Q_{scat} for the same cylinder (red), a $d=114$ nm sphere (green), and a $l=92$ nm cube (blue) in air (dashed), all on a $n_{sub}=3.5$ semi-infinite substrate (solid). All particles consist of Si and have the same volume. The three geometries are sketched below (a) and (b). Note that the sphere sticks 7 nm into the substrate to prevent an infinitely sharp contact area. **c-e)** Vertical crosscuts through the center of all three particles in the plane parallel to the E -field of the source, showing the normalized $|E|^2$ (color) and electric field lines (gray). The particle surroundings and air-substrate interface are indicated with white dashed lines. The respective geometries are shown above the figures. The displacement current loops are clearly visible. In the bottom, the same crosscuts as above, now showing the normalized $|H|^2$ (color) of the MD modes. The magnetic field lines are not plotted since $H \sim 0$ in this plane (perpendicular to source). (Reprinted from [30])

1. Mie resonators: an overview

Furthermore, for all shapes Q_{scat} increases significantly due to the enhanced LDOS, when put onto a substrate. However, comparing the solid lines with the dashed lines shows that both the cylinder (red) and the cube (blue) show the dramatic broadening of the ED and MD resonances when compared to the case in air, causing the ED to appear as a shoulder on top of the MD mode. For the sphere (green), the broadening is significantly less and the ED remains to be a separate peak.

Vertical crosscuts (parallel to the E-field of the driving field) through the center of all particles on the $n_{sub} = 3.5$ semi-infinite substrate, at the MD resonance wavelength allow in understanding this difference. Figures 1.5c to 1.5e show both the normalized $|E|^2$ (color) and the electric field lines (gray) and the normalized $|H|^2$ (color), in the middle and in the bottom parts, respectively. The magnetic field lines are not plotted because $H \sim 0$ in this plane, which is perpendicular to the H-field orientation of the driving field. The electric field lines clearly show the displacement current loops that induce the magnetic dipole \vec{m} of the MD mode. Both the distribution of $|E|^2$ and $|B|^2$ show that for the cylinder and the cube a significant fraction of the displacement current loop extends into the substrate. For the sphere, despite the fact that it sticks into the substrate, this effect is much smaller.

As a result, the coupling to the substrate is much weaker for the sphere than for the cylinder and cube. This is also clearly observable in the distribution of $|B|^2$ (bottom sections of figs. 1.5c to 1.5e), which show that the magnetic field profile of the MD mode inside the substrate is much brighter for the cylinder and the cube, when compared to the sphere. The contact area of the resonator with the substrate is thus very important to get an efficient coupling of the impinging light to the substrate and provides tunability of the radiation rate into the substrate. Note that in figs. 1.5c to 1.5e a second (reversed) current loop can be observed in the substrate below the particles. This is attributed to image dipoles induced by the dipole moments in the particles.

This relevance of the substrate in determining the properties of Mie resonances can be exploited, for instance, for sensing application whenever the substrates were porous, an example of this will be given in chapter 3.

1.4 Functional nanophotonics with Mie resonators: the state of the art

During the last decades, great efforts were spent in understanding the optical properties of metallic nanoparticles, driven by their application potential. Plasmonic nanoantennas constitute a simple but remarkable example of the capability of metallic nanostructures to strongly enhance the interaction of light at the nanoscale [32]. Manipulation of light via two-dimensional metasurfaces is another possible application of metallic devices, that allows to interact with the polarization, the spectrum or the wavefront of an incident light wave [33]. Even though these topics still remain fruitful fields of research, plasmonic nanostructures suffer from the strong absorption losses of metals at optical frequencies, as has already been previously highlighted. A possible approach to overcome this problem, lies in exploring the electric and magnetic Mie-type resonances from all-dielectric nanoparticles. Such all-dielectric nanoparticles, while exhibit low losses at optical frequency, can be applied in direct analogy to metallic nanoparticles for most of specific applications. Nevertheless, high-permittivity all-dielectric nanoparticles do not “just” provide a low-loss implementation of many concepts that have been previously explored for nanoplasmonic structures, but they offer additional and fundamentally new opportunities based on the multipolar properties of their electric and magnetic eigenmodes.

This section overviews the state of the art of research into high-index dielectric nanoparticle structures and on how to utilize their properties for functional photonic nanostructures.

1.4.1 Dielectric metasurfaces

A dielectric metasurface is a two-dimensional arrangement of designed dielectric building blocks, called meta-atoms, on a subwavelength scale. The subwavelength arrangement with regard to the wavelength of operation ensures that only the zeroth diffraction order can propagate, as pioneering demonstrated in 1996 by Chen and colleagues [34]. Diffractive optics was in fact the precursor field in the development of dielectric metasurfaces [35–37]. In such arrangements, the metasurface optical properties are

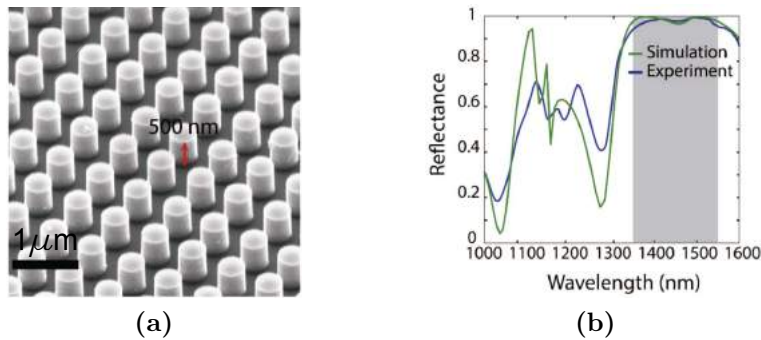


Figure 1.6: *a)* Scanning electron micrograph and *b)* measured and calculated reflectance of a Mie-resonant silicon mirror. The average reflectance exceeds 98% in the gray-shaded region. Reprinted from [38].

dominated by the optical response, in our case usually the Mie-type resonances, of the individual building blocks. Dielectric metasurfaces offer a formidable design freedom of the resonant meta-atoms and their arrangement, thereby enabling the implementation of a myriad of transformations. Several of these possibilities will be discussed in the following.

Dielectric mirrors. Reflectors were among the first functional dielectric metasurface devices that were realized [38, 39]. In fact, a subwavelength arrangement of high-index dielectric scatterers can have a reflectivity close to unity at the spectral position of both its electric and magnetic resonances (fig. 1.6). Consequently, Mie-resonant dielectric metasurfaces act as frequency-dependent mirrors. The frequency dependence can be tailored via the nanoresonator geometry and arrangement. Interestingly, while in the electric resonance the metasurface acts very similarly to a conventional metallic mirror, where the phase of the electric field is reversed upon reflection, in the magnetic resonance the metasurface becomes a “magnetic mirror” [40–43], which does not reverse the phase of the reflected electric field. Instead, the phase of the reflected magnetic field is reversed.

Sharp Fano resonances. While broad resonances leading to large bandwidths are desirable for the dielectric metasurfaces mirrors, several other potential applications are interested in resonances as sharp as possible. In dielectric Mie resonators, thanks to their low absorption losses, the line width of the resonances are mainly attributed to radiative losses, consequently narrow bandwidth can be obtained by tailoring radiative resonant interactions [44]. One type of such interactions is associated with Fano

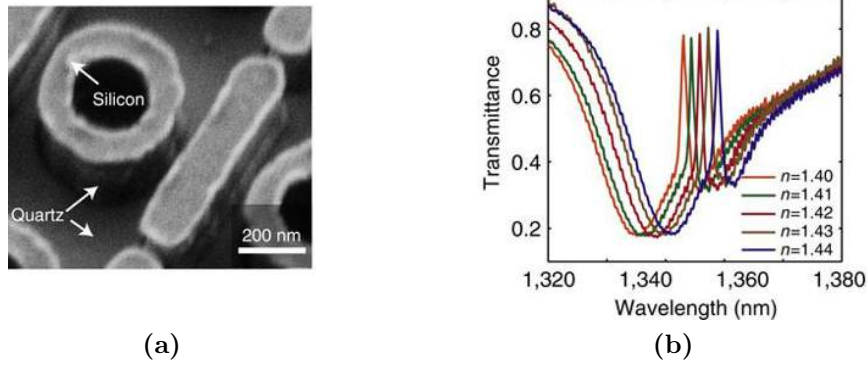


Figure 1.7: **a)** SEM image of the sample. **b)** Measured transmittance spectra of the metasurface when immersed in oil with refractive index ranging from 1.40 to 1.44. Reprinted from [50].

resonances, widely studied in many branches of physics including nanophotonics [45]. An attractive generality of the physics of Fano resonances comes from its interference origin between a continuum (or broad) state and a discrete (or narrow) state [46]. This feature is observed in many wave scattering processes and occurs due to the coexistence of at least two scattering channels, one of them being a resonant one. Then, in the vicinity of the resonant frequency, the interaction between the two scattering channels holds to both constructive and destructive interference with a sharp variation of the scattering profile.

Very recently, Fano resonances were studied in dielectric Mie resonators, which do not suffer from metal losses [47, 48]. In this case, Mie-type resonances in dielectric nanostructures can provide both broad and narrow modes [49]. For example, a broad dipolar resonance can interact with a higher-order, narrow Mie resonance to induce a Fano resonance. These dielectric Fano structures can exhibit sharp optical spectra together with strong field enhancement and steep spectral dispersion at the resonance frequencies.

From an application point of view, the sharp spectral features associated with Fano resonances in photonic nanostructures can be exploited for sensitivity refractive-index sensing, as the line width $\Delta\lambda$ of the resonance directly enters the expression for the sensing figure of merit defined as $FOM = S \Delta\lambda$, where S stands for the spectral shift of the resonance frequency per refractive-index unit change ($S = \delta\lambda_r/\delta n$) [51]. In Yang et al. [50], a silicon metasurface with a FOM of 103 was demonstrated, far

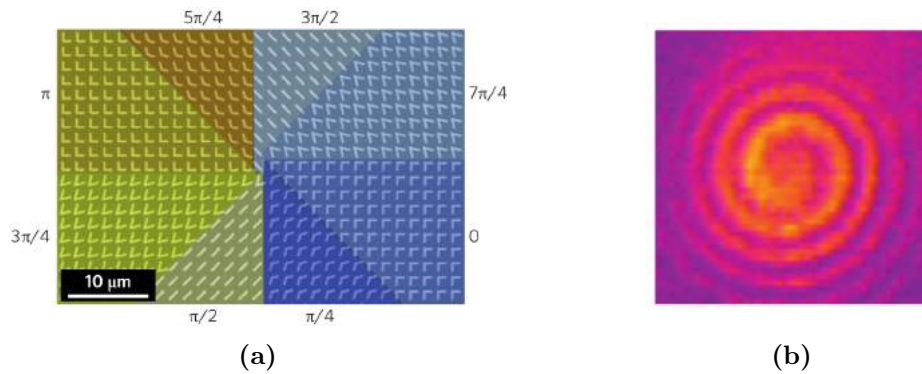


Figure 1.8: **a)** SEM image of a mid-infrared metasurface phase plate able to generate optical vortex beams. The plate comprises eight regions, each occupied by one V-antenna type. The antennas are arranged to create a phase shift that varies azimuthally from 0 to 2π , thus producing a helicoidal scattered wavefront corresponding to an orbital angular momentum $L = 1$. **b)** Spiral interferogram created by the interference between a vortex beam created by the plate in panel **a)** and a co-propagating Gaussian beam. The size of the interferogram is about $30\ \text{mm} \times 30\ \text{mm}$. Reprinted from [53].

exceeding the current record for Fano-resonant plasmonic sensors. In fig. 1.7 is shown the realized structure with the relative transmittance spectra which, thanks to the Fano resonances, allow for detecting refractive index changes. In Wu et al. monolayer sensing with a Fano-resonant silicon metasurface was discussed as an example for the detection of a single sheet of graphene [52]. Furthermore, sharp spectral features facilitate the tuning and switching of the metasurface response with high switching contrast, as small changes in the resonance position lead to strong changes in the level of transmission and reflection. In this thesis we addressed an example of tunable dielectric metasurface, discussed in chapter 3.

Wavefront control. A wide range of other possible functionalities for dielectric metasurfaces rises when the metasurface design and thus the optical response depend on the in-plane position. In particular, spatially variant phase shift of the incident wavefront is the most prominent example and can be achieved by tailoring the resonant properties of the metasurface as a function of the in-plane position, as shown in fig. 1.8 [53]. This way, functionalities like beam deflection, beam shaping and focusing rise due to propagation through or reflection at a sheet of just nanoscale thickness. This is in stark contrast to conventional optical devices, which have to accumulate a propagation phase over a macroscopic distance in order to obtain the same effect. Moreover, the phase shift acquired thanks to dielectric metasurfaces can be different for different

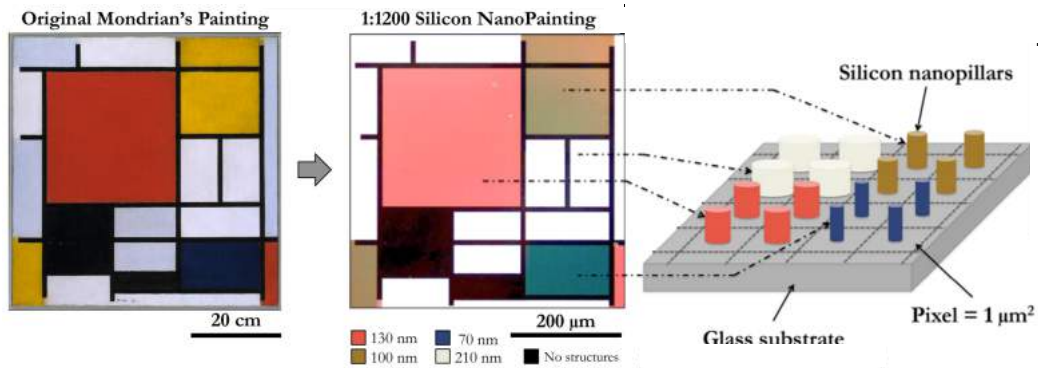


Figure 1.9: On the left, the original Mondrian painting “Composition in red, yellow, blue and black”, 1921 ($59.5 \times 59.5 \text{ cm}^2$). In the center, the micropainting reduction (1:1200, $500 \times 500 \mu\text{m}^2$) made with silicon nanoparticles on glass. On the right, a sketch of the geometries of the resonators. Reprinted from [60].

polarization of the incoming light, therefore polarization-dependent wavefront control can be reached.

Huygens metasurfaces. Another application of high refractive index nanoresonators is in the emerging field of Huygens metasurfaces [53–56], that allow for full phase control and high transmission efficiency. For this application, low-loss dielectric nanoresonators are designed to emulate the behavior of the forward-propagating elementary wavelets following Huygens’ principle [53]. With an appropriate design of dielectric metasurfaces the scattering in the backward direction can be completely suppressed and all the light is scattered in the forward direction, leading to ideally unity transmission. As was analyzed in section 1.2.1 for the complete directional scattering coming from the combination between two in phase electric and magnetic dipole, this characteristic behavior is largely conserved for a realistic dielectric nanostructure, where high-index dielectric nanoparticle can be carefully designed to behave as the magnetoelectric dipole scatterers [57–59].

Structural colors. Photonics engineering can be also used to imprint colors without the use of pigments or organic colors [61]. The color “arises” from the photonic response and can be tuned via the shape and composition of the nanostructures; this effect is also denominated structural color. High refractive index resonators have been proposed to improve the versatility, sustainability, and reliability of structural colors [62]. Thanks to the fact that subwavelength silicon particles exhibit well defined electric and magnetic Mie resonances in the visible spectrum [10, 63], they provide structural

1. Mie resonators: an overview

colors that can be controlled when modifying the shape and the crystallinity of silicon [22, 64], when observed in dark-field spectroscopy.

To summarize, low-loss dielectric devices based on Mie resonators has been demonstrated to have the ability to transform a given incident light field into a desired output light field with engineered spectrum, wave-front, and polarization characteristics. The metasurface concept also offers a range of possibilities for wavefront shaping devices, which are not possible or are difficult to obtain with conventional optics, such as chromatically corrected collimators and imaging systems [65], and can also be used as polarization or color filters or in related applications. Moreover, metasurface-based devices, such as lenses, polarizers or beam deflectors, can be lightweight and compact, making them interesting e.g. for space flight applications as well as for portable and integrated optoelectronic devices.

1.4.2 Tunable and nonlinear applications

As dielectric nanosurfaces start to be exploited for practical applications, the capability of actively controlling their optical properties becomes increasingly important. The ability to dynamically and reversibly shift the spectral position of the metasurface resonances as a function of an externally controllable parameter is essential for the realization of, for example, tunable spectral filters, spontaneous emission control, and dynamically adjustable flat optical components such as lenses, beam shapers, and

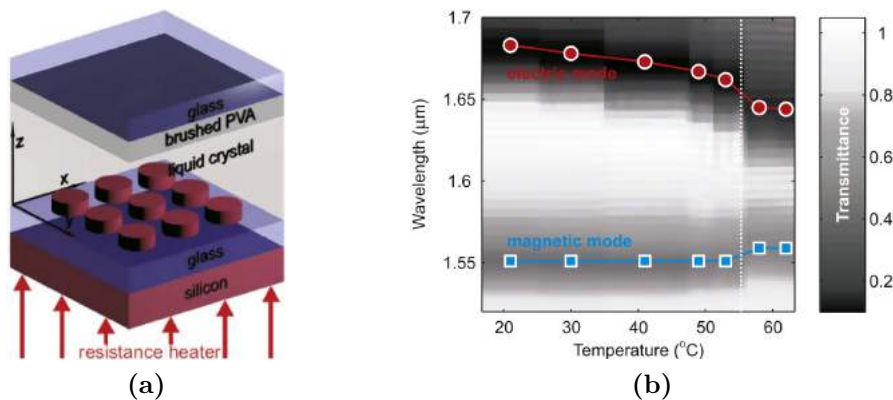


Figure 1.10: a) Sketch of a silicon nanodisk metasurface integrated into a liquid crystal cell b) Temperature controlled tuning of the resonant optical response on the liquid-crystal embedded metasurface. Reprinted from [66].

holograms. Since high-index dielectric nanoparticle structures provide the capability to tailor the optical near- and far-field response via the shape, symmetry, arrangement and material composition of the meta-atoms, they offer control over the properties of the light fields that drive the light-matter interaction processes. Thanks to the resonant nature of the optical response of high-index dielectric nanoparticles, a dynamic tuning and switching of the optical response is facilitated, as small changes in the excitation conditions can lead to strong changes in the optical response.

Recent advances in tunable and switchable dielectric metasurfaces are reviewed in the following.

Dynamic tuning of the spectral positions of the electric and magnetic dipole resonances of all-dielectric silicon metasurfaces was first demonstrated based on the temperature-dependent refractive-index change of a nematic liquid crystal surrounding the dielectric nanoresonators [66] (see fig. 1.10a).

An applied voltage can also be used as an external control parameter instead of temperature.

Moreover, an alternative to liquid crystal tuning and switching, which was recently demonstrated for dielectric metasurfaces [67], is mechanical tuning. By embedding the dielectric meta-atoms in an elastomeric matrix, the optical response of the metasurface can be dynamically tuned by stretching the substrate [67]. In their article, Gutruf et al. demonstrate that, subject to the uniaxial strain, the elastomeric array shows a clear resonance shift toward longer wavelengths for the excitation perpendicular to the strain direction and toward shorter wavelengths for the excitation polarized along the strain direction, as shown in fig. 1.11.

Mie resonances, thanks to their capability to enhance light-matter interaction at the nanoscale, can be exploited also for nonlinear optical effects. In the first experiment investigating nonlinear effects in such systems, silicon nanodisks on a silicon oxide substrate were addressed by an intense femtosecond laser pulse train with frequency ω close to the magnetic dipole resonance [68]. As a result of the high silicon third-order susceptibility, the transmitted signal contains pulses of the tripled fundamental frequency 3ω . Since the third-harmonic signal is proportional to the third power of the local field intensity, when the frequency of the fundamental wave coincides with

1. Mie resonators: an overview

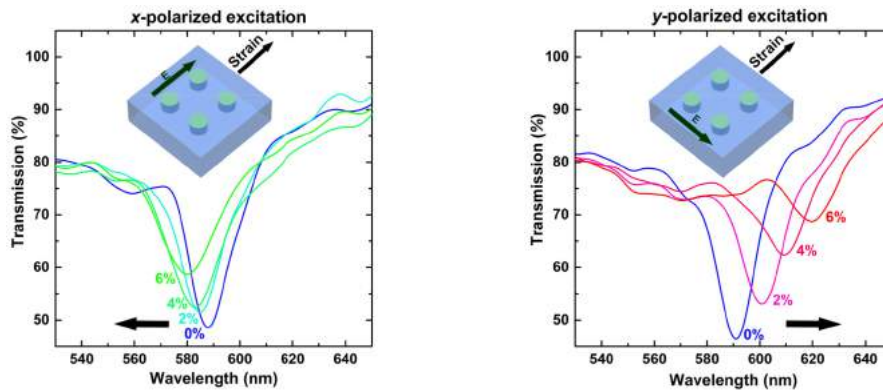


Figure 1.11: Polarization-dependent transmission spectra of the metasurfaces with increasing applied strain. **a)** *y*-Polarization excitation transverse to applied strain. **b)** *x*-Polarization excitation parallel to applied strain. Reprinted from [67].

a Mie resonance, an enhancement of the third harmonic process in the nanodisks was observed, reaching two orders of magnitude with respect to bulk silicon for excitation at the magnetic dipole resonance frequency. The maximum infrared-to-visible conversion efficiency was found to be comparable to that achieved by slow light in photonic crystal waveguides.

The substantially low quality factor of the Mie resonance can offer a route for ultrafast all-optical switching. Accounting that the energy of fundamentals dipolar resonances is stored in the resonator only for a short time before it is radiated, fast switching processes are possible with switching times established by the driven non-linear processes. For instance, Shecherbakov and colleagues [69] demonstrated fast switching of transmission through a Mie resonators metasurface at resonant frequencies. Here, using pump-probe measurements, pulse-limited switching times as short as 65 fs are achieved thanks to two photon absorption process.

All-optical switching effects in dielectric nanoparticles were also suggested for inducing an ultrafast change of the scattering pattern of the nanoparticle [70], opening up interesting possibilities for ultrafast all-optical routing. The dynamic tuning of the optical response and the enhanced optical non-linearity of Mie resonators are still in its infancy with respect to other photonic platforms, such as photonic crystals and/or plasmonics. Still, their peculiarities fit a large variety of applications where low losses and broad band optical resonators are the needed. Last but not least advantage of Mie platform is related to possible bottom up fabrication approaches, which would fits

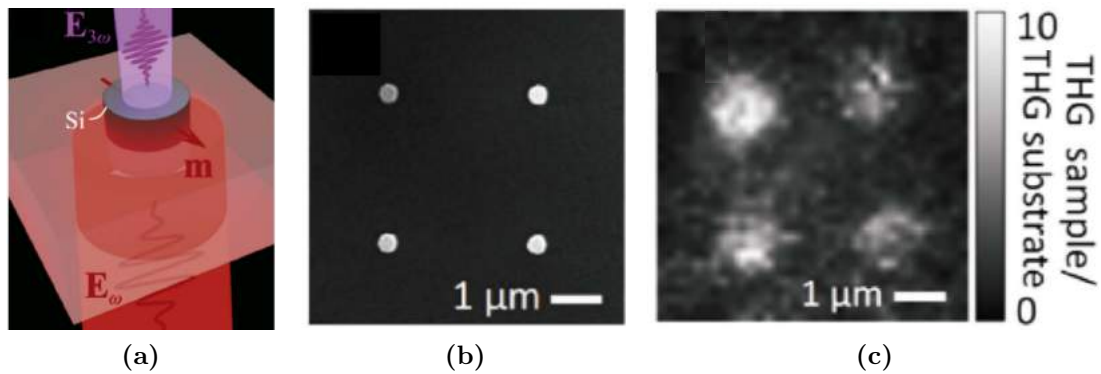


Figure 1.12: *a)* Schematic of third-harmonic generation from silicon nanodisk resonators. *b)* Electron micrograph of a sample with a sparse arrangement of silicon nanodisk resonators. *c)* Third-harmonic microscopy image with the same field of view as *b)*. The third-harmonic signal from the individual nanodisks appears as bright spots. Reprinted from [68].

the large scale and low cost requirements needed for mass production applications; the next paragraph is therefore dedicated a brief overview of fabrication techniques.

1.5 Outline of possible fabrication techniques

Nowadays, rapid progresses in nanotechnology allow for multiple and alternative choices for semiconductor nanoparticle fabrication.

From a historical point of view, silicon was the most frequently used high-index material in the visible and IR ranges owing to its relatively low cost and low imaginary part of the refractive index [71], and it has represented for long time the most illustrative example. Therefore, methods of fabrication of silicon nanostructures have been the first employed. Starting from silicon several different methods of fabrication have been developed also for other high-index dielectric materials.

Since in the context of nanophotonic applications, the main required aims are nanoparticles supporting magnetic and electric resonances in the visible or near-IR region, nanoparticles' size and shape are the first requirement when a fabrication method is chosen. However, this is not the only aim of all these techniques, but also the repeatability and throughput of fabrication methods, precise control of nanoparticle geometry, simplicity of the fabrication procedure (quantity of steps involved in the fabrication process), and manipulation of nanoparticle space arrangement play a role when con-

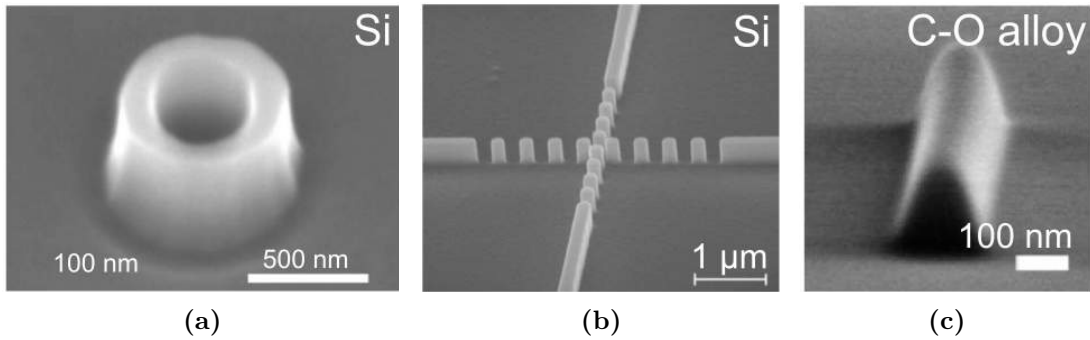


Figure 1.13: Examples of high-index dielectric nanostructures fabricated by lithography. **a)** Scanning electron microscopy (SEM) image of hollow Si cylinder. (Reprinted from [72]) **b)** Periodic dielectric waveguide crossing. (Reprinted from [73]) **c)** SEM image of carbonaceous dielectric nanorod antenna fabricated by electron-beam-induced deposition. (Reprinted from [74])

sidering the efficiency of the fabrication technique.

Therefore, in the last decades, a plethora of methods have been developed for the realization of Mie-resonant high-index nanoparticles and here is presented an overview of these methods as well as their applicability to different high-index dielectric materials.

1.5.1 Lithography

The most straightforward methods for fabrication of nanostructures involve lithography, since it provides high repeatability and flexibility to fabricate nanostructures of complicated shapes. The conventional lithographic methods have been successfully applied for the fabrication of single nanoparticles of different shapes. The geometry of these structures (the outer diameter, height, and wall thickness) can be varied to control the resonant wavelength and relative spectral spacing and composition of the modes.

Figure 1.13 shows some examples of possible design for single dielectric nanostructures made by lithographic techniques. Combining electron beam lithography (EBL) and reactive ion etching (RIE), silicon nanoresonators consisting of hollow nanocylinders can be made; the outer diameter spans from 108 to 251 nm, depending on the desired supported resonances, and with an inner gap of >20 nm (fig. 1.13a) [72]. In Ref. [73], the intersection region of two silicon waveguides was replaced by an array of silicon cylinders (fig. 1.13b). Silicon is not the only high-index dielectric material

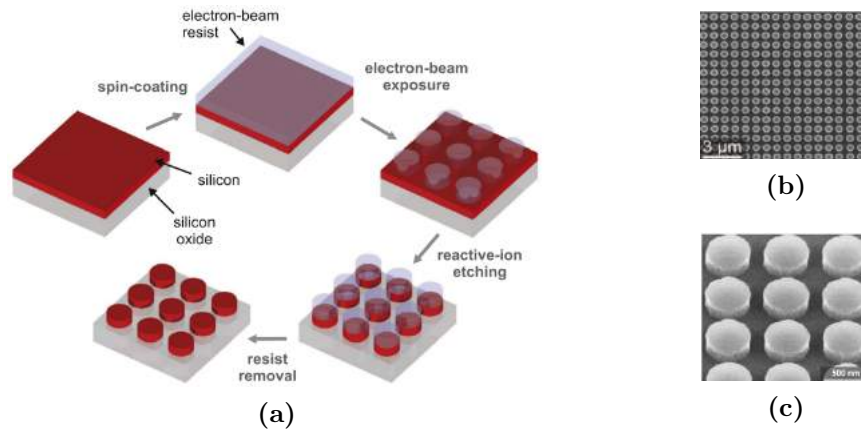


Figure 1.14: a) Sketch of the steps performed during conventional electron-beam lithography based fabrication of high-index dielectric nanoresonators. (Reprinted from [16, 63–65]) b) Scanning electron micrograph of a typical silicon nanodisk sample.

etched by lithographic methods: amorphous alloys with C and O can be fabricated via electronbeam- induced deposition, as it is the single dielectric nanorod antenna shown in fig. 1.13c [74]. In this work, the control of nanoantenna geometry via fabrication process was applied for resonant light scattering manipulation over the whole visible wavelength range.

Lithographic micro/nanofabrication processing techniques are proven to be effective also in terms of large-scale nanostructure array fabrication. This is very important for the creation of high-index metasurfaces setting higher demands for the precision and reproducibility of nanostructures. The controllable fabrication of silicon nanoparticle arrays was achieved by a multistep method, illustrated in fig. 1.14a. The wafers are spin-coated by a negative-tone electronbeam resist and EBL is used to define the desired two dimensional pattern, providing extraordinary in-plane design freedom and precision control (fig. 1.14c). After exposure and development, the resulting resist pattern is directly employed as an etch mask in a reactive ion etch of the silicon thin film and residual resist is removed by oxygen plasma. While EBL is the tool of choice for scientific studies, where typically only few samples of a kind are realized, this general fabrication scheme can be readily up-scaled to large areas by replacing the time-consuming and expensive EBL procedure with scalable lithographic approaches, such as UV lithography, nanoimprint lithography, interference lithography, or nanosphere lithography [38].

In the framework of this thesis, soft nanoimprint lithography has been investigated

for the realization of large-surface arrays of titania-based resonators. This technique allows to obtain several replicas of a master sample following a simple chemical procedure, thus reducing the costs and the processing time. In chapter 3 will be outlined fabrication's details and practical potential of this procedure.

Furthermore, it was recently demonstrated that the equipment-intensive reactive ion etching step can be substituted by a low-cost wet etch with alkaline solutions [75].

Similar fabrication schemes to the one described for silicon-based structures have also been demonstrated for other high refractive index materials, including tellurium [40, 76, 77], gallium arsenide [15], silicon carbide [78], and titanium oxide [79, 80].

Thus, lithographic methods remain more reliable for high-index nanostructure fabrication combining three important qualities: high reproducibility for the nanostructure arrays, an ability to fabricate the nanostructures with complex shape, and high resolution. It should be mentioned that in spite of these advantages, lithographic methods can hardly be applied for the creation of spherical nanoparticles, which represent interest not only for fundamental but also for applied sciences. Moreover, the multiple steps that are often required for high-index nanostructure fabrication, as well as the complexity and high cost of equipment motivate researchers to look for novel fabrication methods.

1.5.2 Chemical methods

Chemical methods offer a different and promising approach for high-index nanoparticles' fabrication. The main advantages of these methods consist on a higher throughput with respect to lithographic methods, flexibility and relative simplicity in synthesis of materials and compatibility with other methods of solid material synthesis.

Chemical vapor deposition is an example of such chemical methods, enabling for the fabrication of silicon nanoparticles of different sizes, from hundreds nanometers to few micrometers. Spherical silicon nanoparticles can arise from decomposition of disilane gas (Si_2H_6) at high temperatures into solid silicon and hydrogen [81, 82].

Another viable technique to obtain spherical nanoparticles is aerosol generation method on silicon. This method consists in atomizing a hydro-alcoholic solution in a carrying air flux, obtaining a gaseous solution where the size of the droplets varies

between tenths to several microns. The suspended microdroplets/air mixture passed within a circular furnace to complete the evaporation the dry particles. This mixture was then accelerated at the furnace output and impacted over the target surface. Densification and crystalization of the spheres is then achieved via a further heating step. More details of this technique will be given in chapter 2, where an experimental demonstration of its potentiality is presented.

Alkaline chemical etching combined with electronic lithography is another possible way for fabricating crystalline silicon Mie resonators [75]. This method allows for eliminating reactive-ion etching and both silicon nanoresonators and oligomers can be created. Monodispersed silicon colloid can be achieved via decomposition of trisilane (Si_3H_8) at high temperature [83]. Particles size can be controlled by changing the trisilane concentration and reaction temperature. Large ensembles of similar silicon nanoparticles can be obtained; the size dispersion lies in the range of several percents, and particles can be ordered into hexagonal lattice by self-assembly. The main disadvantage of this technique is the porosity and high hydrogen content of nanoparticles, as well as the necessity of additional patterning methods to fabricate functional structures. The chemical procedures can be easily combined with lithography. The combination of lithography and oxidization in air allows for fabrication of periodic nanobeam arrays for active photocatalytic material creation supporting optical Mie resonances [84]. Moreover chemical methods can be combined with standard commercial products to generate nanostructures for new dielectric metamaterial designs. An example is Sol-Gel process, which is used to obtain metal oxides, as silica (SiO_2) and titania (TiO_2) [85]. The process involves conversion of monomers into a colloidal solution (sol) that acts as the precursor for an integrated network (or gel) of either discrete particles or network polymers. By sol-gel technique, durable thin films with a variety of properties can be deposited on a substrate by spin-coating or dip-coating. When the “sol” is cast into a mold, a “wet gel” will form and with further drying and heat treatment, the “gel” is converted into dense materials. Chapter 3 will give further details on this technique, by proving its performances in realizing large arrays of Titania based Mie resonators.

In conclusion, although chemical waste, possible contamination of fabricated nano-materials, additional steps for generation nanostructures constitute disadvantages of

chemical methods and impose constraints on the possible application areas, the chemical techniques provide large opportunities for the fabrication of nanostructures exhibiting Mie resonances.

1.5.3 Solid state dewetting

Thin films are generally metastable in the as-deposited state and will dewet or agglomerate to form arrays of islands when heated, then dewetting is another viable technique to obtain on a large scale high-index dielectric nanoparticles. Dewetting process can happen well below a film's melting temperature so that it occurs while the film remains in the solid state. The driving force for dewetting is minimization of the total energy of the free surfaces of the film and substrate, and of the film-substrate interface and this driving force increases with decreasing film thickness, as well as the rate of dewetting is accelerated. As a consequence, the temperature at which dewetting occurs decreases with film thickness [86]. The main controlling parameters in this method are the heating temperature and properties of the thin film (thickness, presence of defects, and initial patterns).

Silicon nanoparticles with different size and shape are obtained from dewetting of thin crystalline [87] or amorphous [88] silicon films. Silicon monocrystalline resonators assemble together to form complex disordered structures (fig. 1.15a). Nanoparticles size and location control can be achieved only by using additional lithographic methods. In spite of this fact, dewetting allows for very high productivity of Mie-like resonators and can be applied to several materials.

By changing dewetting parameters, as for instance the substrate temperature during the growth process, different assemblies can be achieved, such as needlelike Te crystallites reported in ref. [90]. Thermal dewetting has been explored also for generating two-component SiGe nanoparticles. In ref. [89], a thin Ge layer is epitaxially grown on 9 nm-thick Si film, showing that Ge layer lowers the dewetting temperature and makes possible the creation of SiGe nanoparticles (fig. 1.15b). A further potential of joining silicon dewetting with germanium deposition is presented in chapter 4 of this thesis, where is highlighted how this technique allows a modification of the size distribution and the shape of the dewetted particles.

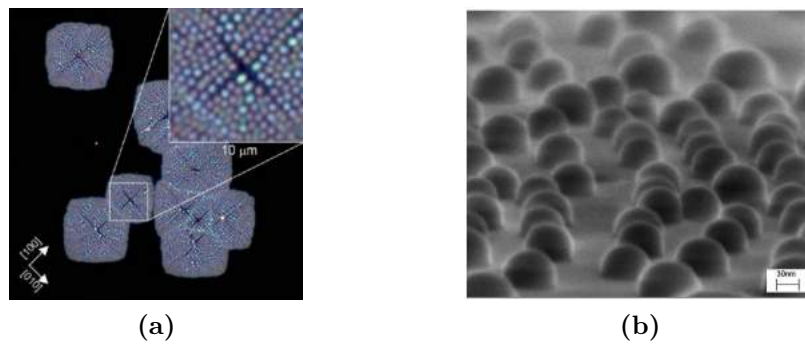


Figure 1.15: **a)** Dark-field optical image of silicon nanoparticles obtained by thin film dewetting. Reprinted from [87]. **b)** Thermal dewetting and agglomeration of 4ML Ge/9 nm Si in SOI. Grazing-takeoff-angle SEM image of the agglomeration region near a dewetting initiation site. Reprinted from [89].

To conclude dewetting constitute a simple and highly productive method for the fabrication of high-index nanoparticles. On the other hand, controllable arrangement of size and shape of the particles on the sample is still a problem for this method and can be reached only through addition methods, as for instance lithography or others laser-assisted methods.

1.5.4 Laser-assisted methods

Due to their material selectivity, submicron resolution and high energy density, laser-assisted methods are applied in different nanofabrication processes, especially where high precision in fabrication is required. For a start, laser-assisted methods were proven to be effective for the fabrication of nanoparticles with diameters less than 100 nm. Laser ablation in liquids allows for realizing colloids of chemically pure nanoparticles, with the great advantage of relatively high productivity and lack of harmful chemical wastes. Laser-assisted methods have recently been applied for the generation of nanoparticles with sizes larger than 100 nm supporting Mie resonances in the visible and near-IR regions, satisfying the growing interest in the fabrication of high-index nanoparticles. Due to the recent application of laser-assisted methods in the fabrication of high-index nanoparticles, they have been so far applied mostly to silicon.

Ablation of bulk materials. The first experiments towards fabrication of high-index nanoparticles using laser-assisted methods were conducted by direct laser ablation: Si nanoparticles of various sizes were fabricated by femtosecond laser ablation

1. Mie resonators: an overview

of a silicon wafer. A glass substrate was placed on top of the wafer. The laser beam passed through the glass substrate and ablated the surface on the target. Ablated silicon nanoparticles were collected and solidified on the glass substrate [14]. Laser ablation was also successfully implemented for the fabrication of single-crystalline sub-micron- and micron-sized ZnO, CdSe, ZnSe, and CeO₂ microspheres [91], proving the effectiveness of this technique for the fabrication of high-index nanoparticles with optical response in the visible and IR spectral ranges. The work of Lewi et al. [92] shows the possibility to tune by small temperature modulation, high-quality-factor Mie-resonances of PbTe Mie spherical nanoresonators.

However, the inability to control by laser-ablation the fabricated nanoparticle sizes and their locations constitutes a problem to the extension of this approach to most applications.

Laser-induced transfer. To produce nanoparticles by laser-induced transfer (LIT) methods, laser radiation is focused on the interface between the printed mate-

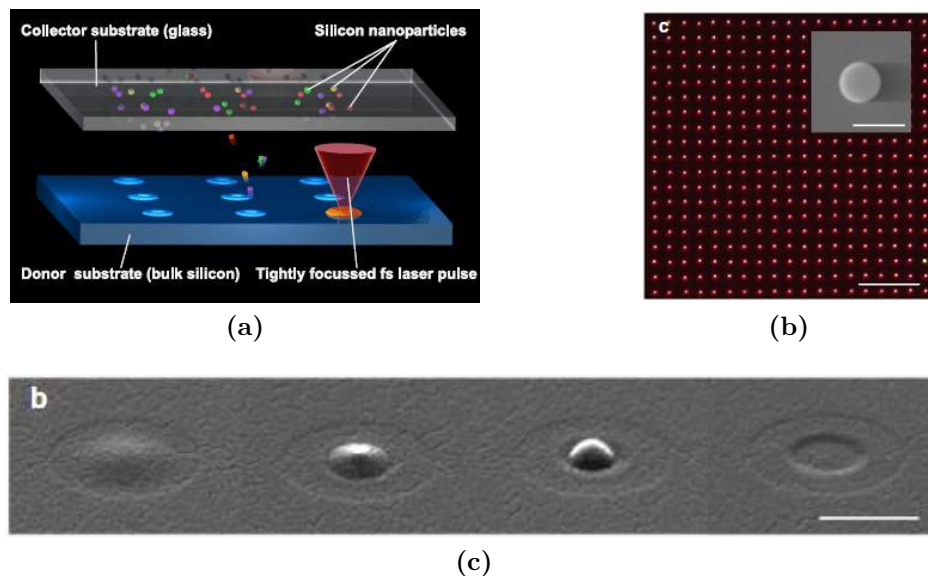


Figure 1.16: **a)** Schematic illustration of laser generation process of Si nanoparticles using Gaussian intensity distribution on the target surface. **b)** Array of several hundreds of amorphous Si nanoparticles (diameter of ~160 nm) fabricated by this method and visualized with dark-field microscopy (scale bar, 20 μm). The insert shows a SEM image of a single Si nanoparticle in this array (scale bar, 200 nm). **c)** SEM images of the target before and after nanoparticle-ejection process from the SOI substrate. From left to right, the laser pulse energy is gradually increased. The last image shows the remaining hole in the silicon layer after the nanoparticle ejection (scale bar, 400 nm). Reprinted from [93].

rial and transparent donor substrate providing material transfer onto another receiver substrate placed in close contact with the donor sample (fig. 1.16a). This method was firstly demonstrated in the 80s by Bohandy et al. [94] for metallic nanoparticles and had briefly become a promising approach for laser printing of nanoparticles from different materials: metals and semiconductors. LIT methods have just recently demonstrated to be effective for the implementation on Si-based Mie resonators at visible frequencies [93]. The realized structures are shown in fig. 1.16b; highly ordered arrays of nanoparticles can be produced by this technique, and dimers consisting of submicron crystalline silicon nanoparticles with different interparticle distances, ranging from 5 to 375 nm, have been demonstrated [95].

Moreover, laser annealing can be applied for post-processing of laser-printed semiconductor nanoparticles to controllably change their phase from an initially amorphous state to a crystalline state. This allows tailoring their optical properties [93].

Laser-induced dewetting. Laser radiation can be applied for patterning of thin films of high index materials by their controlled dewetting into nanoscale structures. This can provide routes to controlled self-organization to obtain desirable patterns formed by solid-state dewetting and a number of studies have demonstrated how surfaces can be intentionally patterned to produce artificial periodic features on dewetted films [86].

Belov and colleagues demonstrated fabrication of arrays of crystalline silicon nanoparticles from amorphous silicon films, fabricated by direct laser writing on amorphous Si-layers without applying initially crystalline materials or any additional annealing steps [96].

Focused ion beam etching has been proved to be effective on SiGe films; Wood et al. realized ordered arrays of SiGe islands which radii span from 70 to 150 nm [97]. This approach made possible fabrication of ordered resonator arrays in a large scale (fig. 1.17a) functioning as color pass-band filters across the full visible spectral range.

The use of donut-shaped laser beam for annealing of amorphous silicon thin films was demonstrated in ref. [98]. Here morphological modification of the film into a nanodome during thermocapillary-induced dewetting led to phase transformation from amorphous to crystalline structure in the laser focus area (fig. 1.17b).

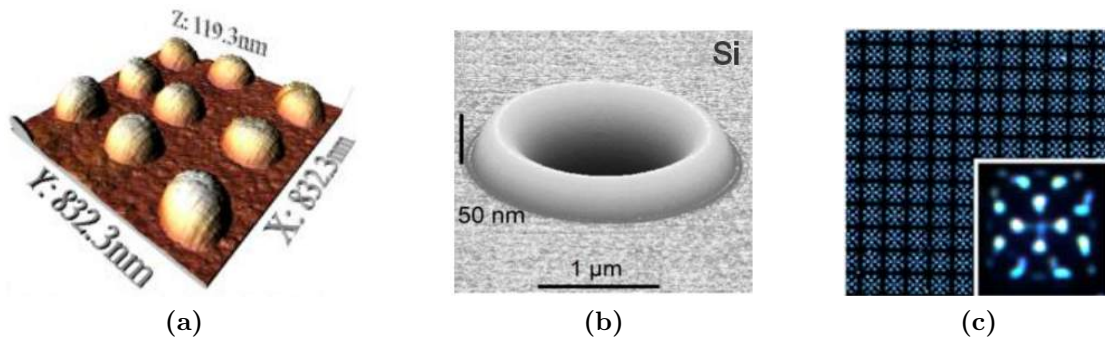


Figure 1.17: **a)** AFM image of SiGe islands in an ordered array. Reprinted from [97]. **b)** SEM image of typical laser dimples on c-Si. Reprinted from [98]. **c)** Optical dark-field microscopy images of controlled dewetted Si on SiO₂. The panel displays the full patterned area while the bottom right inset displays an enlarged view of a single dewetted patch [99].

To conclude, thanks to its ability to combine the advantages of dewetting and direct laser patterning, laser-assisted dewetting can be considered as a promising method for large-scale fabrication of high-index nanoparticles.

Summarizing this part, it should be noted that laser-assisted methods require high-quality laser radiation (high laser pulse stability, perfect beam shape, and excellent focusing), including high precision and reliability of the position systems. However, these constraints do not lessen the basic advantages of the laser-assisted methods (single-step process, high repeatability, modification of nanoparticles' crystalline phase, space arrangement of the fabricated nanoparticles), which all are important for the realization of nanophotonic devices.

1.5.5 Comparison between different fabrication techniques

In the previous sections, different techniques to realize high-index dielectric resonators have been analyzed, showcasing their performances and limitations. By summarizing, one can identify some representative parameters of the efficiency of such fabrication techniques as repeatability, productivity, resolution, positioning control (possibility to place a nanostructure at a certain position immediately during fabrication), and method complexity [2]. Figure 1.18 sketches different fabrication techniques, exemplifying them in terms of these five parameters, thus highlighting their inherent pros and cons. Therefore, it is not surprising that the choice of a fabrication method of

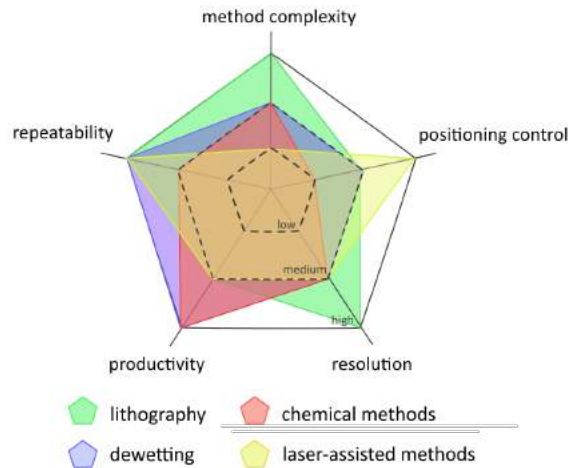


Figure 1.18: Schematic comparison of fabrication techniques of high-index nanostructures. Reprinted from [2].

high-index nanoparticles is determined by the objectives of the investigation and the applicability of these methods should be carefully considered for each special situation.

For instance, when high precision in positioning nanostructures is required and typically only few samples of a kind are realized, laser-assisted methods are preferable. In contrast, if high productivity is a cornerstone, chemical methods will be considered as more preferable ones or scalable lithographic approaches, such as nanoimprint lithography, can replace time-consuming and expensive laser assisted or lithographic methods, as will be demonstrated in chapter 3.

Another important issue is the capability to access different shapes and arrangements of dielectric resonators. For instance, the archetypical Mie resonator of spherical (or ellipsoidal) shape is not easily accessible by standard two-dimensional lithographic approaches. An alternative fabrication method, which enables the realization of nearly perfectly shaped silicon nanospheres, is laser printing, described in section 1.5.4.

In this thesis different fabrication approaches, with relative applications, have been investigated. In the next chapters we are going to present the realization of spherical nanoparticles by chemical aerosol technique, large arrays of pillars obtained with soft nanoimprint lithography and random metasurfaces of silicon-germanium resonators achieved by solid state dewetting. Skipping the idea of describing and summarizing all the used experimental and theoretical tools in separated chapters, we will present the

various works closing all sections with a Methods paragraph where technical details are reported.

1.6 Summary and conclusions

Mie-type resonances of high refractive index dielectric nanoparticles and their assemblies can show complex and peculiar interactions with light. They combine low absorption losses with a strong resonant optical response and the ability to tailor the resonance properties by the size, shape, material composition, and arrangement of the nanoparticles. Importantly, both electric and magnetic multipolar scattering features are supported in high-index dielectric nanoparticles, even for basic nanoresonator shapes. Based on these properties, a plethora of photonic functionalities were implemented based on Mie-resonant subwavelength nanoparticles.

We have discussed how silicon and silicon oxide have historically been the main constituent materials, capitalizing on the good optical properties and technological relevance, such as CMOS compatibility, of this material system. However, while the linear optical losses in silicon are negligible at telecom frequencies, for wavelengths below its indirect electronic bandgap at $1.1 \mu\text{m}$, absorption starts to become significant and increases further with decreasing wavelength. Consequently, for highly efficient (low-loss) dielectric nanostructures operating in the visible spectral range, a different material is needed. The requirements for such a material are a large real part of the refractive index and a small imaginary part of the refractive index in the visible spectral range. Figure 1.19 shows how a range of materials perform with respect to the desired properties, such as refractive index and absorption. While these requirements regarding the characteristic of their complex refractive index are essential, they are not sufficient. In addition, the material should also be suitable for nanostructuring, stable at ambient conditions and ideally non-toxic.

Within the framework of this thesis, different dielectric materials will be presented, going beyond the performances of silicon and showing as different material choices can match with different and specific practical applications. In the following chapters three works on Mie resonators are going to be discussed and doing this, we aim to present

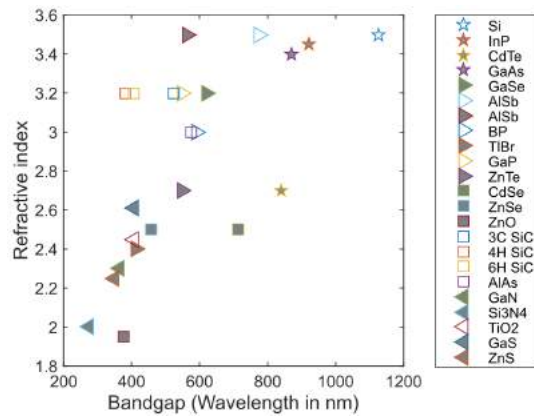


Figure 1.19: b) Evaluation of various materials with regard to their typical refractive index and electronic bandgap, which determines the onset of absorption. Materials with a direct bandgap are represented by filled symbols. Reprinted from [11].

these dielectric nanostructures as a suitable platform for nanophotonics and future real-world applications.

References

- [1] J. M. ENOCH. “History of Mirrors Dating Back 8000 Years”. In: *Optometry and Vision Science* 83.10 (Oct. 2006), pp. 775–781.
- [2] D. G. Baranov, D. A. Zuev, S. I. Lepeshov, O. V. Kotov, A. E. Krasnok, A. B. Evlyukhin, and B. N. Chichkov. “All-dielectric nanophotonics: the quest for better materials and fabrication techniques”. In: *Optica* 4 (2017), p. 814.
- [3] K. J. Vahala. “Optical microcavities”. In: *Nature* 424 (2003), pp. 839–846.
- [4] J. A. Fan, C. Wu, K. Bao, J. Bao, R. Bardhan, N. J. Halas, V. N. Manoharan, P. Nordlander, G. Shvets, and F. Capasso. “Self-Assembled Plasmonic Nanoparticle Clusters”. In: *Science* 328 (2010), pp. 1135–1138.
- [5] J. S. and J. Z. “All-dielectric metamaterials”. In: *Nat. Nanotechnol.* 11 (2016), pp. 23–36.
- [6] G. Mie. “Beiträge zur Optik trüber Medien, speziell kolloidaler Metallösungen”. In: *Annals of Physics* 330 (1908), pp. 377–445.
- [7] J. D. Jackson and R. F. Fox. “Classical Electrodynamics, 3rd ed.” In: 67 (1999), pp. 841–842.
- [8] Q. Zhao, J. Zhou, F. Zhang, and D. Lippens. “Mie resonance-based dielectric metamaterials”. In: *Scientific Reports* 12 (2009), pp. 60–69.
- [9] H. C. van de Hulst. *Light Scattering by Small Particles*. Ed. by Dover. 1981.
- [10] A. García-Etxarri, R. Gómez-Medina, L. S. Froufe-Pérez, C. López, L. Chantada, F. Scheffold, J. Aizpurua, M. Nieto-Vesperinas, and J. J. Sáenz. “Strong magnetic response of submicron silicon particles in the infrared”. In: *Optics express* 19.6 (2011), pp. 4815–4826.
- [11] M. Decker and I. Staude. “Resonant dielectric nanostructures: a low-loss platform for functional nanophotonics”. In: *Journal of Optics* 18.10 (Sept. 2016), p. 103001.
- [12] A. D. Yaghjian. “Increasing the supergain of electrically small antennas using metamaterials”. In: *2009 3rd European Conference on Antennas and Propagation*. Mar. 2009, pp. 858–860.

-
- [13] M. Kerker, D.-S. Wang, and C. Giles. “Electromagnetic scattering by magnetic spheres”. In: *JOSA* 73.6 (1983), pp. 765–767.
- [14] Y. H. Fu, A. I. Kuznetsov, A. E. Miroschnichenko, Y. F. Yu, and B. Luk’yanchuk. “Directional visible light scattering by silicon nanoparticles”. In: *Nature Communications* 4 (2013).
- [15] S. Person, M. Jain, Z. Lapin, J. J. Saenz, G. Wicks, and L. Novotny. “Demonstration of zero optical backscattering from single nanoparticles”. In: *Nano letters* 13.4 (2013), pp. 1806–1809.
- [16] Q. Zhao, L. Kang, B. Du, H. Zhao, Q. Xie, X. Huang, B. Li, J. Zhou, and L. Li. “Experimental Demonstration of Isotropic Negative Permeability in a Three-Dimensional Dielectric Composite”. In: *Physical Review Letters* 101 (2008).
- [17] J. A. Schuller, R. Zia, T. Taubner, and M. L. Brongersma. “Dielectric metamaterials based on electric and magnetic resonances of silicon carbide particles”. In: *Physical review letters* 99.10 (2007), p. 107401.
- [18] L. Cao, P. Fan, E. S. Barnard, A. M. Brown, and M. L. Brongersma. “Tuning the Color of Silicon Nanostructures”. In: *Nano Letters* 10.7 (July 2010), pp. 2649–2654.
- [19] G. Brönstrup, N. Jahr, C. Leiterer, A. Csáki, W. Fritzsche, and S. Christiansen. “Optical Properties of Individual Silicon Nanowires for Photonic Devices”. In: *ACS Nano* 4.12 (Nov. 2010), pp. 7113–7122.
- [20] K. Seo, M. Wober, P. Steinvurzel, E. Schonbrun, Y. Dan, T. Ellenbogen, and K. B. Crozier. “Multicolored Vertical Silicon Nanowires”. In: *Nano Letters* 11.4 (Apr. 2011), pp. 1851–1856.
- [21] A. B. Evlyukhin, C. Reinhardt, A. Seidel, B. S. Luk’yanchuk, and B. N. Chichkov. “Optical response features of Si-nanoparticle arrays”. In: *Physical Review B* 82.4 (2010), p. 045404.
- [22] A. B. Evlyukhin, S. M. Novikov, U. Zywiets, R. L. Eriksen, C. Reinhardt, S. I. Bozhevolnyi, and B. N. Chichkov. “Demonstration of magnetic dipole resonances of dielectric nanospheres in the visible region”. In: *Nano letters* 12.7 (2012), pp. 3749–3755.

- [23] A. I. Kuznetsov, A. E. Miroshnichenko, Y. H. Fu, J. Zhang, and B. Luk'yanchuk. “Magnetic light”. In: *Scientific Reports* 2 (2012).
- [24] W. Lukosz. “Light emission by magnetic and electric dipoles close to a plane dielectric interface III Radiation patterns of dipoles with arbitrary orientation”. In: *Journal of the Optical Society of America* 69 (1979), p. 1495.
- [25] M. Xiao. “Imaging with reflection near-field optical microscope in light of evanescent dipole radiation”. In: *Optics Communications* (1996).
- [26] A. B. Evlyukhin and S. I. Bozhevolnyi. “Point-dipole approximation for surface plasmon polariton scattering: Implications and limitations”. In: *Physical Review B* 71 (2005).
- [27] P. Fan, K. C. Y. Huang, L. Cao, and M. L. Brongersma. “Redesigning Photodetector Electrodes as an Optical Antenna”. In: *Nano Letters* 13 (2013), pp. 392–396.
- [28] P. Spinelli, M. Verschuuren, and A. Polman. “Broadband omnidirectional antireflection coating based on subwavelength surface Mie resonators”. In: *Nature Communications* 3 (2012), p. 692.
- [29] P. Spinelli, B. Macco, M. A. Verschuuren, W. M. M. Kessels, and A. Polman. “Al₂O₃/TiO₂ nano-pattern antireflection coating with ultralow surface recombination”. In: *Applied Physics Letters* 102 (2013), p. 233902.
- [30] J. van de Groep and A. Polman. “Designing dielectric resonators on substrates: Combining magnetic and electric resonances”. In: *Optics Express* 21 (2013), p. 26285.
- [31] P. Spinelli, C. van Lare, E. Verhagen, and A. Polman. “Controlling Fano line-shapes in plasmon-mediated light coupling into a substrate”. In: *Optics Express* 19 (2011), A303.
- [32] P. Bharadwaj, B. Deutsch, and L. Novotny. “Optical Antennas”. In: *Advances in Optics and Photonics* 1 (2009), p. 438.
- [33] N. Meinzer, W. L. Barnes, and I. R. Hooper. “Plasmonic meta-atoms and meta-surfaces”. In: *Nature Photonics* 8 (2014), pp. 889–898.

-
- [34] F. T. Chen and H. G. Craighead. “Diffractive lens fabricated with mostly zeroth-order gratings”. In: *Optics Letters* 21.3 (1996), p. 177.
- [35] P. Lalanne, S. Astilean, P. Chavel, E. Cambril, and H. Launois. “Design and fabrication of blazed binary diffractive elements with sampling periods smaller than the structural cutoff”. In: *Journal of the Optical Society of America A* 16.5 (1999), p. 1143.
- [36] P. Lalanne, S. Astilean, P. Chavel, E. Cambril, and H. Launois. “Blazed binary subwavelength gratings with efficiencies larger than those of conventional échellette gratings”. In: *Optics Letters* 23.14 (1998), p. 1081.
- [37] P. Lalanne. “Waveguiding in blazed-binary diffractive elements”. In: *Journal of the Optical Society of America A* 16.10 (1999), p. 2517.
- [38] P. Moitra, B. A. Slovick, W. li, I. I. Kravchenko, D. P. Briggs, S. Krishnamurthy, and J. Valentine. “Large-Scale All-Dielectric Metamaterial Perfect Reflectors”. In: *ACS Photonics* 2 (2015), pp. 692–698.
- [39] P. Moitra, B. A. Slovick, Z. G. Yu, S. Krishnamurthy, and J. Valentine. “Experimental demonstration of a broadband all-dielectric metamaterial perfect reflector”. In: *Applied Physics Letters* 104 (2014), p. 171102.
- [40] S. Liu, M. B. Sinclair, T. S. Mahony, Y. C. Jun, S. Campione, J. Ginn, D. A. Bender, J. R. Wendt, J. F. Ihlefeld, P. G. Clem, J. B. Wright, and I. Brener. “Optical magnetic mirrors without metals”. In: *Optica* 1 (2014), p. 250.
- [41] M. Esfandyarpour, E. C. Garnett, Y. Cui, M. D. McGehee, and M. L. Brongersma. “Metamaterial mirrors in optoelectronic devices”. In: *Nature Nanotechnology* 9 (2014), pp. 542–547.
- [42] A. S. Schwanecke, V. A. Fedotov, V. V. Khardikov, S. L. Prosvirnin, Y. Chen, and N. I. Zheludev. “Optical magnetic mirrors”. In: *Journal of Optics A: Pure and Applied Optics* 9 (2007), pp. L1–L2.
- [43] V. A. Fedotov, A. V. Rogacheva, N. I. Zheludev, P. L. Mladyonov, and S. L. Prosvirnin. “Mirror that does not change the phase of reflected waves”. In: *Applied Physics Letters* 88 (2006), p. 091119.

- [44] A. E. Miroshnichenko and Y. S. Kivshar. “Fano Resonances in All-Dielectric Oligomers”. In: *Nano Letters* 12 (2012), pp. 6459–6463.
- [45] B. Lukýanchuk, N. I. Zheludev, S. A. Maier, N. J. Halas, P. Nordlander, H. Giessen, and C. T. Chong. “The Fano resonance in plasmonic nanostructures and metamaterials”. In: *Nature Materials* 9 (2010), pp. 707–715.
- [46] A. E. Miroshnichenko, S. Flach, and Y. S. Kivshar. “Fano resonances in nanoscale structures”. In: *Reviews of Modern Physics* 82 (2010), pp. 2257–2298.
- [47] M. Pu, M. Song, H. Yu, C. Hu, M. Wang, X. Wu, J. Luo, Z. Zhang, and X. Luo. “Fano resonance induced by mode coupling in all-dielectric nanorod array”. In: *Applied Physics Express* 7 (2014), p. 032002.
- [48] M. Song, H. Yu, C. Wang, N. Yao, M. Pu, J. Luo, Z. Zhang, and X. Luo. “Sharp Fano resonance induced by a single layer of nanorods with perturbed periodicity”. In: *Optics Express* 23 (2015), p. 2895.
- [49] E. Lee, I. C. Seo, S. C. Lim, H. Y. Jeong, and Y. C. Jun. “Active switching and tuning of sharp Fano resonances in the mid-infrared spectral region”. In: *Optics Express* 24.22 (2016), p. 25684.
- [50] Y. Yang, I. I. Kravchenko, D. P. Briggs, and J. Valentine. “All-dielectric meta-surface analogue of electromagnetically induced transparency”. In: *Nature Communications* 5 (2014).
- [51] K. M. Mayer and J. H. Hafner. “Localized Surface Plasmon Resonance Sensors”. In: *Chemical Review* 111 (2011), pp. 3828–3857.
- [52] C. Wu, N. Arju, G. Kelp, J. A. Fan, J. Dominguez, E. Gonzales, E. Tutuc, I. Brener, and G. Shvets. “Spectrally selective chiral silicon metasurfaces based on infrared Fano resonances”. In: *Nature Communications* 5 (2014).
- [53] N. Yu and F. Capasso. “Flat optics with designer metasurfaces”. In: *Nature Materials* 13 (2014), pp. 139–150.
- [54] C. Pfeiffer and A. Grbic. “Metamaterial Huygens’ Surfaces: Tailoring Wave Fronts with Reflectionless Sheets”. In: *Physical Review Letters* 110 (2013).

-
- [55] M. Decker, I. Staude, M. Falkner, J. Dominguez, D. N. Neshev, I. Brener, T. Pertsch, and Y. S. Kivshar. “High-Efficiency Dielectric Huygens’ Surfaces”. In: *Advanced Optical Materials* 3 (2015), pp. 813–820.
- [56] A. V. Kildishev, A. Boltasseva, and V. M. Shalaev. “Planar Photonics with Metasurfaces”. In: *Science* 339 (2013), pp. 1232009–1232009.
- [57] E. Pshenay-Severin, M. Falkner, C. Helgert, and T. Pertsch. “Ultra broadband phase measurements on nanostructured metasurfaces”. In: *Applied Physics Letters* 104.22 (June 2014), p. 221906.
- [58] K. E. Chong, I. Staude, A. James, J. Dominguez, S. Liu, S. Campione, G. S. Subramania, T. S. Luk, M. Decker, D. N. Neshev, I. Brener, and Y. S. Kivshar. “Polarization-Independent Silicon Metadevices for Efficient Optical Wavefront Control”. In: *Nano Letters* 15.8 (2015), pp. 5369–5374.
- [59] K. E. Chong, L. Wang, I. Staude, A. R. James, J. Dominguez, S. Liu, G. S. Subramania, M. Decker, D. N. Neshev, I. Brener, and Y. S. Kivshar. “Efficient Polarization-Insensitive Complex Wavefront Control Using Huygens’ Metasurfaces Based on Dielectric Resonant Meta-atoms”. In: *ACS Photonics* 3.4 (Mar. 2016), pp. 514–519.
- [60] J. Proust, F. Bedu, B. Gallas, I. Ozerov, and N. Bonod. “All-Dielectric Colored Metasurfaces with Silicon Mie Resonators”. In: *ACS Nano* 10 (2016), pp. 7761–7767.
- [61] D. Kim, A. L. Giermann, and C. V. Thompson. “Solid-state dewetting of patterned thin films”. In: *Applied Physics Letters* 95.25 (Dec. 2009), p. 251903.
- [62] A. S. Roberts, A. Pors, O. Albrektsen, and S. I. Bozhevolnyi. “Subwavelength Plasmonic Color Printing Protected for Ambient Use”. In: *Nano Letters* 14.2 (Jan. 2014), pp. 783–787.
- [63] A. B. Evlyukhin, C. Reinhardt, and B. N. Chichkov. “Multipole light scattering by nonspherical nanoparticles in the discrete dipole approximation”. In: *Physical Review B* 84 (2011).

- [64] U. Zywiets, C. Reinhardt, A. B. Evlyukhin, T. Birr, and B. N. Chichkov. “Generation and patterning of Si nanoparticles by femtosecond laser pulses”. In: *Applied Physics A* 114 (2014), pp. 45–50.
- [65] F. Aieta, M. A. Kats, P. Genevet, and F. Capasso. “Multiwavelength achromatic metasurfaces by dispersive phase compensation”. In: *Science* 347.6228 (Feb. 2015), pp. 1342–1345.
- [66] J. Sautter, I. Staude, M. Decker, E. Rusak, D. N. Neshev, I. Brener, and Y. S. Kivshar. “Active Tuning of All-Dielectric Metasurfaces”. In: *ACS Nano* 9.4 (Mar. 2015), pp. 4308–4315.
- [67] P. Gutruf, C. Zou, W. Withayachumnankul, M. Bhaskaran, S. Sriram, and C. Fumeaux. “Mechanically Tunable Dielectric Resonator Metasurfaces at Visible Frequencies”. In: *ACS Nano* 10.1 (Dec. 2015), pp. 133–141.
- [68] M. R. Shcherbakov, D. N. Neshev, B. Hopkins, A. S. Shorokhov, I. Staude, E. V. Melik-Gaykazyan, M. Decker, A. A. Ezhov, A. E. Miroshnichenko, I. Brener, A. A. Fedyanin, and Y. S. Kivshar. “Enhanced Third-Harmonic Generation in Silicon Nanoparticles Driven by Magnetic Response”. In: *Nano Letters* 14 (2014), pp. 6488–6492.
- [69] M. R. Shcherbakov, P. P. Vabishchevich, A. S. Shorokhov, K. E. Chong, D.-Y. Choi, I. Staude, A. E. Miroshnichenko, D. N. Neshev, A. A. Fedyanin, and Y. S. Kivshar. “Ultrafast All-Optical Switching with Magnetic Resonances in Nonlinear Dielectric Nanostructures”. In: *Nano Letters* 15 (2015), pp. 6985–6990.
- [70] S. Makarov, S. Kudryashov, I. Mukhin, A. Mozharov, V. Milichko, A. Krasnok, and P. Belov. “Tuning of Magnetic Optical Response in a Dielectric Nanoparticle by Ultrafast Photoexcitation of Dense Electron–Hole Plasma”. In: *Nano Letters* 15.9 (Aug. 2015), pp. 6187–6192.
- [71] I. Staude and J. Schilling. “Metamaterial-inspired silicon nanophotonics”. In: *Nature Photonics* 11.5 (2017), p. 274.
- [72] M. A. van de Haar, J. van de Groep, B. J. Brenny, and A. Polman. “Controlling magnetic and electric dipole modes in hollow silicon nanocylinders”. In: *Optics express* 24.3 (2016), pp. 2047–2064.

-
- [73] E.-K. Lee, J.-H. Song, K.-Y. Jeong, J.-H. Kang, H.-G. Park, and M.-K. Seo. “Resonant light scattering from a single dielectric nano-antenna formed by electron beam-induced deposition”. In: *Scientific Reports* 5 (2015).
- [74] J. Feng, Q. Li, and S. Fan. “Compact and low cross-talk silicon-on-insulator crossing using a periodic dielectric waveguide”. In: *Optics Letters* 35 (2010), p. 3904.
- [75] J. Proust, F. Bedu, S. Chenot, I. Soumahoro, I. Ozerov, B. Gallas, R. Abdeddaim, and N. Bonod. “Chemical Alkaline Etching of Silicon Mie Particles”. In: *Advanced Optical Materials* 3 (2015), pp. 1280–1286.
- [76] J. C. Ginn, I. Brener, D. W. Peters, J. R. Wendt, J. O. Stevens, P. F. Hines, L. I. Basilio, L. K. Warne, J. F. Ihlefeld, P. G. Clem, and M. B. Sinclair. “Realizing Optical Magnetism from Dielectric Metamaterials”. In: *Physical Review Letters* 108 (2012).
- [77] S. Liu, J. F. Ihlefeld, J. Dominguez, E. Gonzales, J. E. Bower, B. D. Burckel, M. B. Sinclair, and I. Brener. *Realization of Tellurium-based all Dielectric Optical Metamaterials using a Multi-cycle Deposition-etch Process*. 2013.
- [78] C. Zou, W. Withayachumnankul, M. Bhaskaran, S. Sriram, and C. Fumeaux. “Dielectric Resonator Nanoantennas: A Review of the Theoretical Background, Design Examples, Prospects, and Challenges”. In: *IEEE Antennas and Propagation Magazine* 59 (2017), pp. 30–42.
- [79] M. Khorasaninejad, W. T. Chen, R. C. Devlin, J. Oh, A. Y. Zhu, and F. Capasso. “Metalenses at visible wavelengths: Diffraction-limited focusing and sub-wavelength resolution imaging”. In: *Science* 352.6290 (2016), pp. 1190–1194.
- [80] R. C. Devlin, M. Khorasaninejad, W. T. Chen, J. Oh, and F. Capasso. “Broadband high-efficiency dielectric metasurfaces for the visible spectrum”. In: *Proceedings of the National Academy of Sciences* 113.38 (2016), pp. 10473–10478.
- [81] R. Fenollosa, F. Meseguer, and M. Tymczenko. “Silicon Colloids: From Microcavities to Photonic Sponges”. In: *Advanced Materials* 20 (2008), pp. 95–98.

- [82] L. Shi, T. U. Tuzer, R. Fenollosa, and F. Meseguer. “A New Dielectric Metamaterial Building Block with a Strong Magnetic Response in the Sub-1.5-Micrometer Region: Silicon Colloid Nanocavities”. In: *Advanced materials* 24.44 (2012), pp. 5934–5938.
- [83] L. Shi, J. T. Harris, R. Fenollosa, I. Rodriguez, X. Lu, B. A. Korgel, and F. Meseguer. “Monodisperse silicon nanocavities and photonic crystals with magnetic response in the optical region”. In: *Nature communications* 4 (2013).
- [84] S. J. Kim, I. Thomann, J. Park, J.-H. Kang, A. P. Vasudev, and M. L. Brongersma. “Light Trapping for Solar Fuel Generation with Mie Resonances”. In: *Nano Letters* 14 (2014), pp. 1446–1452.
- [85] S. P. Sajjadi. “Sol-gel process and its application in Nanotechnology”. In: *Journal of Polymer Engineering and Technology* 13 (Sept. 2005), pp. 38–41.
- [86] C. V. Thompson. “Solid-state dewetting of thin films”. In: *Annual Review of Materials Research* 42 (2012), pp. 399–434.
- [87] M. Abbarchi, M. Naffouti, B. Vial, A. Benkouider, L. Lermusiaux, L. Favre, A. Ronda, S. Bidault, I. Berbezier, and N. Bonod. “Wafer scale formation of monocrystalline silicon-based mie resonators via silicon-on-insulator dewetting”. In: *ACS nano* 8.11 (2014), pp. 11181–11190.
- [88] M. Naffouti, T. David, A. Benkouider, L. Favre, A. Ronda, I. Berbezier, S. Bidault, N. Bonod, and M. Abbarchi. “Fabrication of poly-crystalline Si-based Mie resonators via amorphous Si on SiO₂ dewetting”. In: *Nanoscale* 8.5 (2016), pp. 2844–2849.
- [89] P. P. Zhang, B. Yang, P. P. Rugheimer, M. M. Roberts, D. E. Savage, F. Liu, and M. G. Lagally. “Influence of germanium on thermal dewetting and agglomeration of the silicon template layer in thin silicon-on-insulator”. In: *Journal of Physics D: Applied Physics* 42 (2009), p. 175309.
- [90] E. J. Weidmann and J. C. Anderson. “Structure and growth of oriented tellurium thin films”. In: *Thin Solid Films* 7 (1971), pp. 265–276.

-
- [91] S. Okamoto, K. Inaba, T. Iida, H. Ishihara, S. Ichikawa, and M. Ashida. “Fabrication of single-crystalline microspheres with high sphericity from anisotropic materials”. In: *Scientific Reports* 4 (2015).
- [92] T. Lewi, H. A. Evans, N. A. Butakov, and J. A. Schuller. “Ultrawide Thermo-optic Tuning of PbTe Meta-Atoms”. In: *Nano Letters* 17 (2017), pp. 3940–3945.
- [93] U. Zywietz, A. B. Evlyukhin, C. Reinhardt, and B. N. Chichkov. “Laser printing of silicon nanoparticles with resonant optical electric and magnetic responses”. In: *Nature Communications* 5 (2014).
- [94] J. Bohandy, B. F. Kim, F. J. Adrian, and A. N. Jette. “Metal deposition at 532 nm using a laser transfer technique”. In: *Journal of Applied Physics* 63 (1988), pp. 1158–1162.
- [95] U. Zywietz, M. K. Schmidt, A. B. Evlyukhin, C. Reinhardt, J. Aizpurua, and B. N. Chichkov. “Electromagnetic Resonances of Silicon Nanoparticle Dimers in the Visible”. In: *ACS Photonics* 2 (2015), pp. 913–920.
- [96] P. A. Dmitriev, S. V. Makarov, V. A. Milichko, I. S. Mukhin, A. S. Gudovskikh, A. A. Sitnikova, A. K. Samusev, A. E. Krasnok, and P. A. Belov. “Laser fabrication of crystalline silicon nanoresonators from an amorphous film for low-loss all-dielectric nanophotonics”. In: *Nanoscale* 8 (2016), pp. 5043–5048.
- [97] T. Wood, M. Naffouti, J. Berthelot, T. David, J.-B. Claude, L. Métayer, A. Delobbe, L. Favre, A. Ronda, I. Berbezier, et al. “All-dielectric color filters using SiGe-based Mie resonator arrays”. In: *ACS photonics* 4.4 (2017), pp. 873–883.
- [98] J.-H. Yoo, J. B. In, C. Zheng, I. Sakellari, R. N. Raman, M. J. Matthews, S. Elhadj, and C. P. Grigoropoulos. “Directed dewetting of amorphous silicon film by a donut-shaped laser pulse”. In: *Nanotechnology* 26 (2015), p. 165303.
- [99] M. Naffouti, R. Backofen, M. Salvalaglio, T. Bottein, M. Lodari, A. Voigt, T. David, A. Benkouider, I. Fraj, L. Favre, et al. “Complex dewetting scenarios of ultrathin silicon films for large-scale nanoarchitectures”. In: *Science advances* 3.11 (2017), eaao1472.

Chapter 2

Spherical TiO₂ Mie resonators: single object investigation

In the framework of photonics with all-dielectric nanoantennas, sub-micrometric spheres can be exploited for a plethora of applications including vanishing back-scattering, enhanced directivity of a light emitter, beam steering, and large Purcell factors. Here, the potential of a high-throughput fabrication method based on aerosol-spray is shown to form quasi-perfect sub-micrometric spheres of polycrystalline TiO₂. Spectroscopic investigation of light scattering from individual particles reveals sharp resonances in agreement with Mie theory, neat structural colors, and a high directivity. Owing to the high permittivity and lossless material in use, this method opens the way toward the implementation of isotropic metamaterials and forward-directional sources with magnetic responses at visible and near-UV frequencies, not accessible with conventional Si- and Ge-based Mie resonators.

2.1 Introduction

Dielectric Mie resonators represent a young and promising research topic, with large potentials in photonics, optics, and derived applications [1–3]. Based on sub-micrometric particles that are capable of light manipulation at visible and near-infrared frequencies, these systems offer convenient and ultrathin alternatives to replace complex and bulky optical elements. This ability is due to strong modifications of the local density of

2. Spherical TiO₂ Mie resonators: single object investigation

optical states occurring in sub-micrometric objects made of materials featuring high dielectric constant and sufficiently small absorption losses.

Most studies over the last years have mainly addressed silicon- [4–8] and germanium-based [9–11] Mie resonators, demonstrating that, in several important applications, they could compete with their metallic counterpart supporting localized plasmonic resonances. However, the large absorption of group IV semiconductor compounds at short wavelengths induces strong optical losses, limiting their potential applicability as efficient devices especially at blue and near-UV frequencies [12, 13] (e.g. at 450 nm: $n_{Si} = 4.5$, $k_{Si} = 0.13$; $n_{Ge} = 4.0$, $k_{Ge} = 2.24$). Furthermore, with a few exception based on colloids [14–16] and solid state dewetting [17–20], typical nanofabrication methods of Si(Ge)-based Mie resonators rely on top-down technologies that are not easy to scale-up at affordable prices. TiO₂-based optical devices are an interesting alternative to Si, since Titania has a relatively high refractive index and is fully transparent up to UV frequencies [24,25] (e.g.: at 450 nm: $n_{TiO_2} = 2.55$, $k_{TiO_2} = 1.2 \cdot 10^{-5}$; at 370 nm: $n_{TiO_2} = 2.83$, $k_{TiO_2} = 1 \cdot 10^{-3}$) rendering it, for instance, a strategic material to manipulate the light emitted by conventional GaN-based blue LEDs (at about 450 nm). TiO₂ can be prepared by high-throughput chemical processes, which is a prerequisite for applications requiring large surface systems. It also has many other advantages over Si and metals that are its high chemical, mechanical, and thermal stability, nontoxicity, and relative natural abundance.

To date, several groups have studied the properties of Titania particles as dielectric resonators prepared using conventional top-down microfabrication technologies [21–25] or soft-nanoimprint lithography [26, 27]. They all confirmed that electromagnetic resonances could be generated within these metal oxide objects. However, the limited exploitation of this material is mainly due to the difficulty in applying conventional top-down fabrication methods to TiO₂. Additionally, such approaches do not allow the preparation of spherical resonators [28], which may be interesting for many applications with effective metamaterials, such as beam steering and back-scattering-free optics [9, 29–37], enhanced light extraction [38], resonant transmission [39], manipulation with optical tweezers [40], light detectors [15], directional Fano resonances [41, 42], and much more.

Here, we focus on the investigation of the scattering properties of individual, dense, spherical TiO_2 particles of different sizes. The particles were prepared by a high throughput aerosol generation method on silicon. Their structural properties were characterized by scanning electron microscopy and X-ray diffraction, whereas their scattering properties were assessed using dark-field microscopy and spectroscopy. The optical resonances observed in experiments are interpreted on the basis of analytical solutions of Mie scattering from a sphere in vacuum allowing detailed calculation of the spectral dependence and angular pattern. However, the analytical model neglects the effects of the resonance coupling with the underlying substrate; thus, the validity of this hypothesis is benchmarked by finite differencetime domain simulations in vacuum, on silica and on silicon. Finally, these simulations are compared with experimental scattering spectra of particles on high and low refractive index substrates. We demonstrate that spherical Titania particles are efficient scattering objects and can be tuned in size to scatter in a relatively broad range of frequencies (from blue to near-infrared).

2.2 Results and discussion

Supported spherical TiO_2 particles were prepared through atomization of a sol-gel solution and deposition by direct impaction onto the surface of a silicon wafer (at 450 nm $n_{\text{Si}} = 4.6$) before calcination at 600 °C to ensure densification. The particles were then characterized by high-resolution scanning electron microscopy (SEM) and X-ray diffraction (GIXRD). Systematic structural and spectroscopic measurements of light scattering were performed on particles formed on silicon. Finally, in order to assure a direct comparison of the same object on high and low refractive substrates, some particles were transferred from the Si wafer to a PDMS slice (polydimethylsiloxane, PDMS; at 450 nm $n_{\text{PDMS}} = 1.42$). The elaboration protocol is illustrated in fig. 2.1a whereas the associated details are provided in section 2.4.

SEM investigation revealed that the Titania particles on Si have a spherical shape (as evidenced in Figures 2.1b and 3.5a). This is ascribed to the fact that aerosol generation atomizes liquid, spherical, microdroplets that keep their morphology upon evaporation of water and ethanol within the furnace. This fast evaporation also initiates

2. Spherical TiO₂ Mie resonators: single object investigation

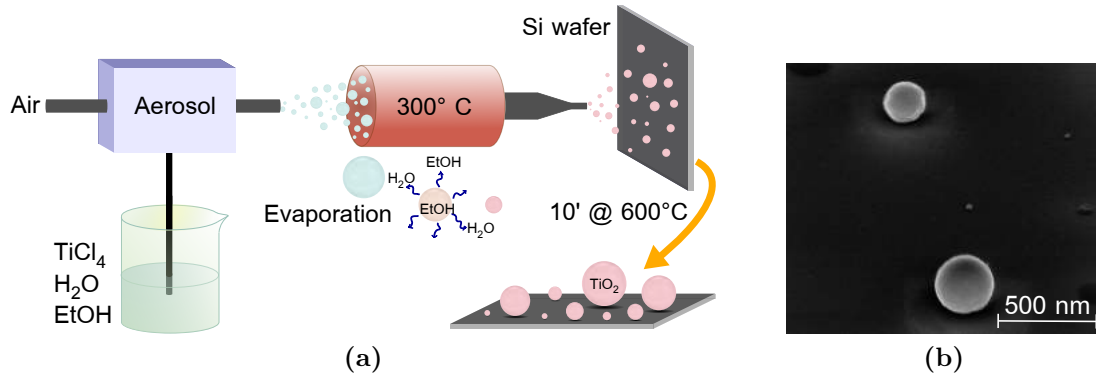


Figure 2.1: **a)** Schematic representation of the process used to prepare dense TiO₂ anatase particles on a Si wafer. **b)** SEM image of two distinct spheres deposited on Si taken at 55° tilting angle.

the poly-condensation of the Titania precursors. As a consequence, a stiff shell is formed on the spheres skin, preventing their collapse upon impaction on the receiving surface and keeping a small contact point with the underlying substrate. The GIXRD pattern measured on a substrate with densely packed spheres reveals that they have crystallized under anatase structure (2.2a). With the GIXRD geometry used for this analysis the Si(311) Bragg reflection is also detectable around $2\theta = 55^\circ$. This is ascribed to the X-ray beam average divergence and to the huge substrate signal. From the fitting of the anatase Bragg reflection, the broadening of the peak corrected from the beam footprint was calculated to be $H_c = 0.29^\circ$, giving an average crystallite size of 27 ± 3 nm. More details are provided in section 2.4.

These spheres are thus composed of densely packed particles building blocks with a size of the order of tens of nanometers as also confirmed by the SEM images (fig. 2.2b). Thus, the surface roughness SR is estimated to be much lower than the wavelength in the visible range ($SR \approx \lambda/50$), so that the sphere surface can be considered as smooth, with negligible influence on the Mie scattering features.

The optical constants of the material composing the particles cannot be measured directly on the spheres. Thus, they were deduced from ellipsometry investigation on a thin, plain film. The ellipsometric ϕ and Δ curves have been fitted with a Cauchy dispersion with $k = 0$ and $n(\lambda) = A + B/\lambda^2$ (with $A = 2.007$, $B = 0.058$), which gives $n = 2.293$ at 450 nm.

Due to such relatively high index of refraction combined with a high transparency window for wavelength longer than 350 nm and interband transitions outside the visible

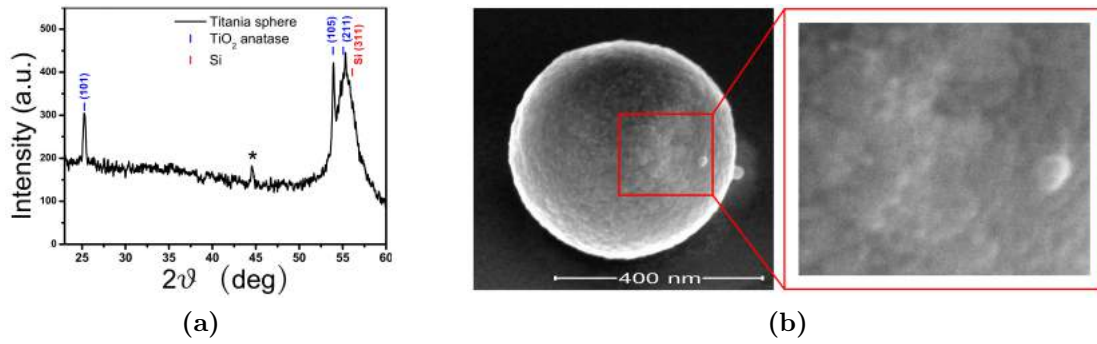


Figure 2.2: **a)** GIXRD pattern of Titania spheres deposited onto a Si (001) substrate. The diffraction pattern is indexed with PDF #00-021-1272 for the TiO_2 anatase phase. The peak indexed with a star likely corresponds to a parasite peak due to unknown impurities from the process. **b)** High-resolution SEM image at high magnification of a typical crystalline Titania sphere.

spectral range, TiO_2 spheres are expected to show Mie resonances in the visible range for dimensions above 200 nm in diameter [6, 31]. Therefore, spheres featuring diameters ranging from about 200 to 500 nm were first spotted by SEM, then imaged in dark-field optical microscopy. Thus, the corresponding scattering spectra were collected via confocal microscopy.

SEM images of TiO_2 spheres on Si with their measured radius (r), corresponding DF images, as well as experimental and theoretical scattering spectra are displayed in figs. 3.5a to 3.5d. The excitation/collection geometry used in experiments and theory is shown in figs. 2.3e and 2.3f. This analysis shows that, when increasing the size of the particle, the wavelength of the corresponding fundamental resonance (the broader and more intense peak in the spectrum) red-shifts accordingly. This behavior is also reflected on the optical appearance of the spheres (fig. 3.5b), where one can observe a marked change of color corresponding to a shift of the fundamental resonance.

Multiple and sharper peaks emerge in the spectra at shorter wavelength with respect to the main resonance (starting from $r = 126$ nm), accounting for the onset of higher order modes within the Titania spheres with Q factor exceeding 20 (Q is defined here as the central wavelength of the resonance divided by its FWHM). Finally, for larger particles ($r > 180$ nm) the fundamental mode shifts to near-infrared frequencies (nonaccessible with our spectroscopic setup).

This picture corresponds fairly well to that of a dielectric sphere scattering the

2. Spherical TiO₂ Mie resonators: single object investigation

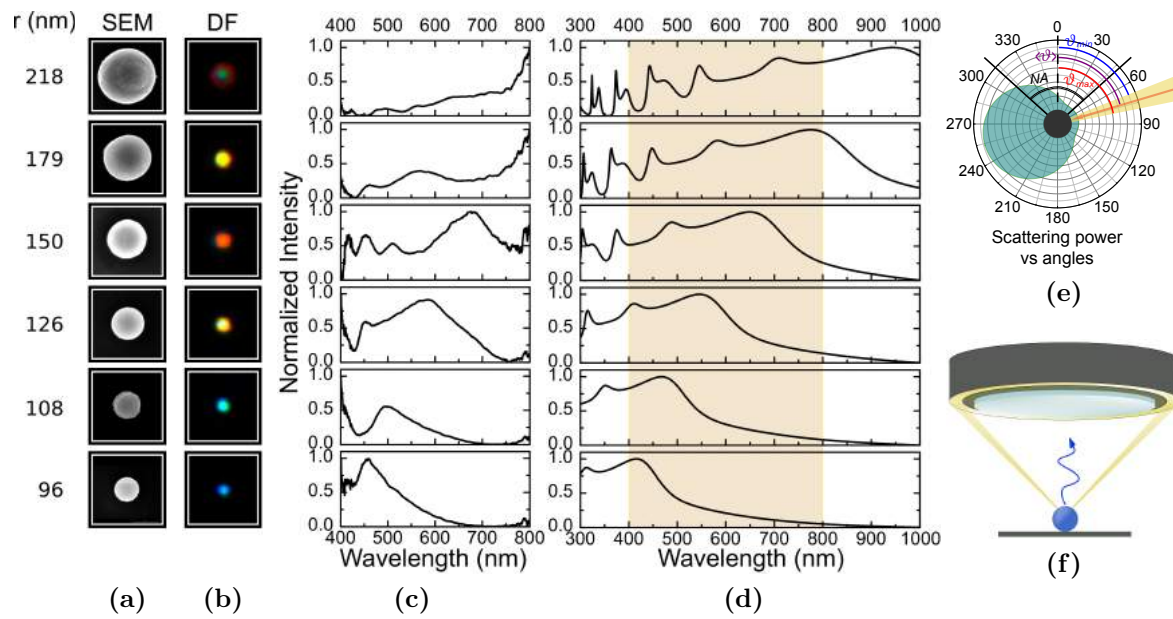


Figure 2.3: **a)** From bottom to top: high-resolution SEM images of TiO₂ spheres on a Si substrate with increasing radius size. The scale bar corresponds to 200 nm. **b)** From bottom to top: dark-field optical microscope images of the TiO₂ spheres shown in **a)**. The scale bar corresponds to 500 nm. **c)** From bottom to top: scattering spectra produced by the TiO₂ spheres shown in **a)** and **b)**. **d)** Analytical models of the scattering spectra of TiO₂ spheres in vacuum for radii corresponding to those shown in **a)**, **b)** and **c)**. The shaded area highlights the spectral range accessible in experiments. **e)** Scheme of the excitation/collection geometry used in experiments. NA is the numerical aperture of the objective lens spanning over an angle of 48.6°; $\langle \theta \rangle$ is the average illumination angle determined by the condenser of the microscope (see **f)** for details). **f)** Polar diagram highlighting the excitation and collection geometry used in experiments and analytical theory (the TiO₂ sphere is represented as the black circle at the center of the polar diagram). The theoretical excitation angle was chosen to be the average between the maximum and minimum experimental excitation angles (respectively θ_{max} and θ_{min}). The collection angle within the NA of the objective lens is also highlighted.

impinging light in the far-field as magnetic or electric multipolar modes: the lowest order resonance is ascribed to the magnetic dipole, expected at a wavelength of about $\lambda_{MD} \approx 2r \cdot n$ [5, 6]. As an example, for a sphere featuring a radius of 96 nm and $n = 2.3$, λ_{MD} is expected at about 440 nm, not far from the peak measured in the experimental case at about 460 nm (bottom panel of Figure 3c). At shorter wavelength with respect to λ_{MD} is found the electric dipolar mode, followed by higher order modes such as magnetic and electric quadrupols.

In support of these experimental results, we calculated the analytical scattering spectra (fig. 3.5d) taking into account the excitation/collection geometry (figs. 2.3e

and 2.3f). At this stage, the spheres are assumed to be in vacuum. Thus, the presence of the Si substrate is completely neglected. In the investigated range of spheres size, the fundamental resonance shifts from blue to near-infrared frequencies, together with the onset of several other peaks of increasingly higher Q-factor. This behavior is expected when moving from the Mie scattering approximation toward the whispering-gallery resonator picture [43] and, despite the oversimplified model, corresponds fairly well to the experimental findings at least for particles radius below 150 nm.

These results account for the possibility to exploit our particles for efficient light manipulation from near-UV up to near-infrared frequencies, confirming the relevance of these spherical Titania-based resonators so far limited to terahertz frequencies [44, 45]. The resonances found in experiments fairly agree with a very simple, analytical model for isolated perfect spheres predicting a red-shift of the resonances and the appearance of multiple peaks at shorter wavelength featuring higher Q factors, when the radius increases. The discrepancies between experiments and theory are likely to be ascribed to small deviations from a perfect spherical shape and, above all, to the presence of the partially reflecting and high-refractive index, silicon substrate, as discussed in more detail later [7, 46, 47].

For a deeper understanding of the nature and appearance (e.g., the color) of the different resonant modes found within a particle, we model the scattering spectra and corresponding angular distribution in the far-field for s and p polarizations (i.e., with the electric field perpendicular and parallel to the scattering plane, respectively). We take into account the case of a TiO_2 sphere having $r = 150$ nm (fig. 3.6 and fourth panel from the bottom in figs. 3.5a to 3.5d). Within the collection angle allowed by the numerical aperture of the microscope objective lens in use (highlighted by dashed lines in the polar plot in figs. 2.4f and 3.6b to 3.6d), the spectra of s and p polarizations are rather different (respectively blue and red spectra in fig. 3.6a). The relatively large angular aperture and intensity of the first two resonances ($\lambda = 656$ nm and $\lambda = 486$ nm, figs. 2.4f and 3.6d) lead to a better coupling within the NA of the microscope with respect to higher order modes, and thus determine the main color registered in our spectra and seen in dark-field images. Higher order modes ($\lambda = 377$ nm and $\lambda = 324$ nm, figs. 3.6b and 3.6c) show a more complex behavior characterized by an overall

2. Spherical TiO₂ Mie resonators: single object investigation

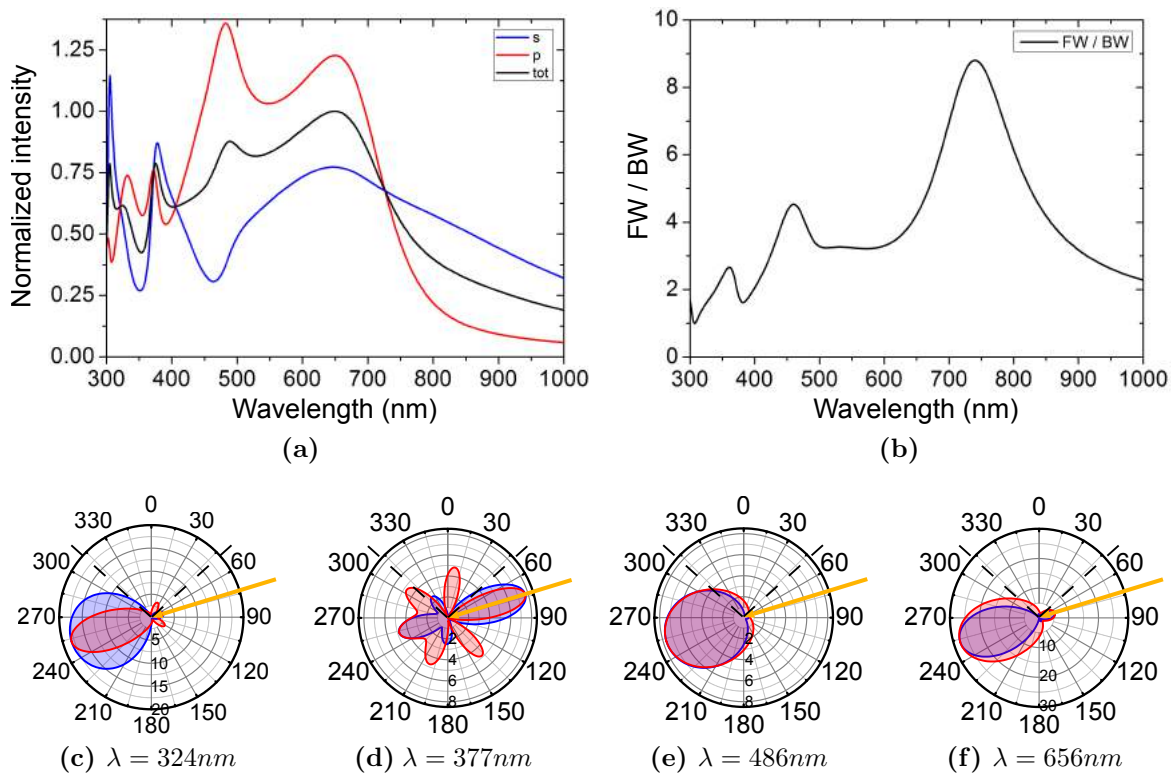


Figure 2.4: **a)** Analytical calculation of the scattering spectrum as a function of wavelength for a TiO₂ sphere having radius $r = 150$ nm in vacuum (see also the corresponding panels in figs. 3.5a to 3.5d). s and p polarizations are represented respectively as red and blue lines whereas their average is in black. The detection conditions are the same as those of the experimental case, as shown in figs. 2.3e and 2.3f. **b)** Forward to backward scattering intensity ratio (FW/BW) as a function of wavelength. **c-f)** Polar plots of the far-field scattering intensity for s (red) and p (blue) polarizations at the wavelength corresponding to the main peaks seen in **a)**. The yellow arrow highlights the wave-vector of the incident light; the dashed lines highlight the collection angle determined by the numerical aperture of the objective lens used in experiments (see also the diagram in figs. 2.3e and 2.3f).

larger angular aperture and the onset of multiple lobes specific of each polarization channel. From the same analysis it is possible to assess the overall properties of the scattering intensity in the far field. Interestingly, for the first two resonances it is mostly forward-like for both s and p polarizations and it shows lobes with rather similar angular apertures, which corresponds to an almost isotropic behavior. Thus, we evaluate the forward to backward ratio ($R = FW/BW$) averaging the two polarization channels (fig. 2.4b): in the investigated spectral range, R stays above 1 and it features strong fluctuations. In particular, a peak of $R \approx 9$ is observed at about 740 nm.

These theoretical predictions show a good directivity and polarization isotropy of

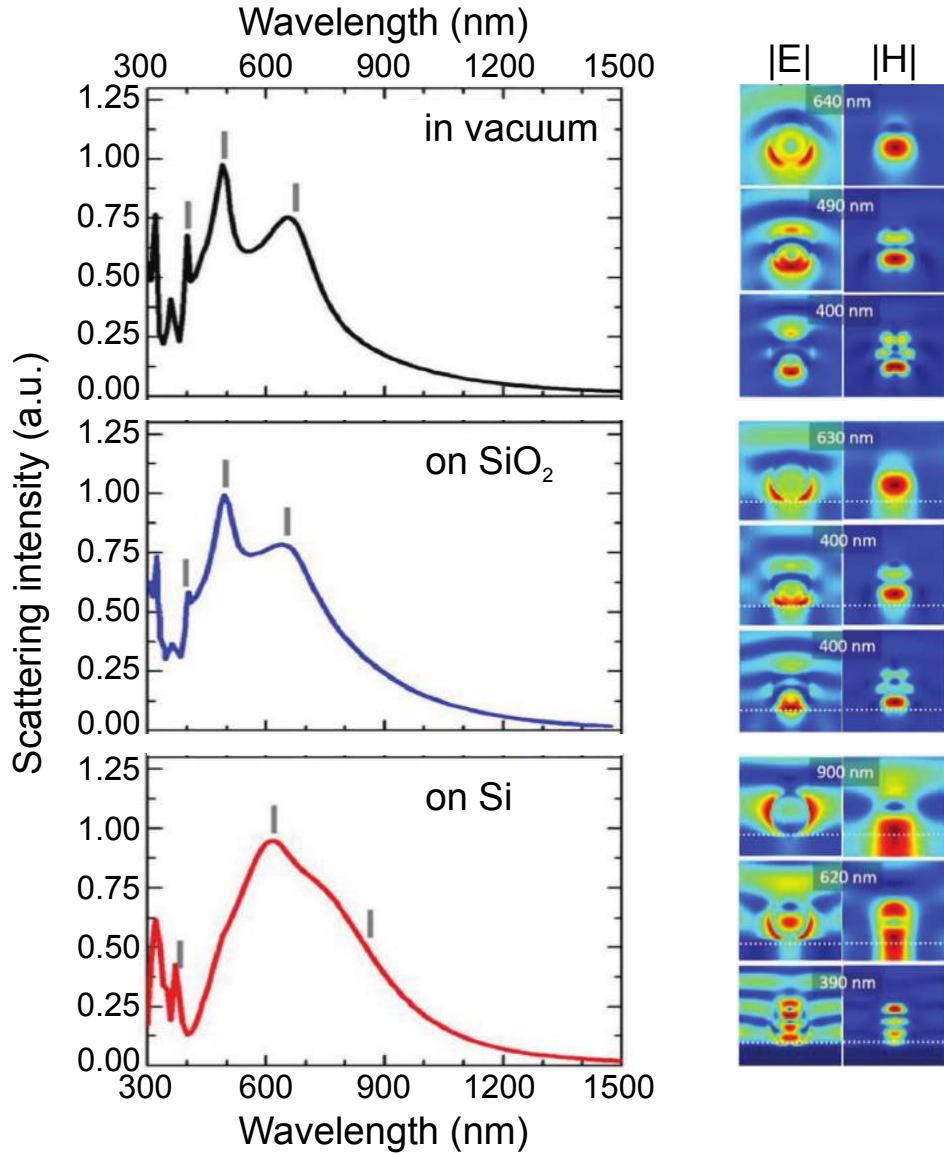


Figure 2.5: FDTD simulations of the total far-field scattering intensity of a TiO_2 particle having a radius of 150 nm. Respectively from the top to the bottom panel are shown the cases of the same particle in vacuum, deposited on a silica substrate and on a silicon substrate. On the right part of the figure the intensities of the corresponding electric ($|E|$) and magnetic field ($|H|$) in the near-field are shown at the wavelengths highlighted by the grey markers.

the first two resonances (respectively ascribed to magnetic and electric dipolar modes [7, 46], as also accounted for by FDTD simulations, fig. 2.5. The large FW/BW value found in theory at 740 nm for a Titania sphere, supports the idea of a Huygens-like source arising from the mutual interference of magnetic and electric dipolar modes (similar to the first Kerker scattering condition [48]) obtained with a dielectric and non-

2. Spherical TiO₂ Mie resonators: single object investigation

magnetic material [9, 29, 30, 37, 49]. This theoretical result is in good agreement with previous predictions for a similar system [31]: zero backward-scattering was predicted at about 800 nm for a TiO₂ particle having $r = 150$ nm and featuring a refractive index of about 2.5. The difference between our findings and those reported in ref. [31] can be ascribed to the slightly lower refractive index used here.

These features are important in view of the exploitation of these particles as low-loss, isotropic meta-materials with a magnetic response [50, 51] at frequencies not accessible by Si and Ge (e.g., for engineering their coupling with near-UV and blue LEDs based on GaN or in general with high- n substrates [7, 46]). However, in spite of the reduced size of the contact region between a sphere and a plane (with respect to disk Mie resonators), the effect of a high refractive index substrate underneath needs to be discussed. Thus, we performed FDTD simulations of the total scattering power from a Titania sphere ($r = 150$ nm) in vacuum, on SiO₂ and Si, under plane wave illumination, at normal incidence with respect to the sample surface (the details of the FDTD method are provided in the devoted section 2.4, Theoretical models) and compared them with light scattering experiments of TiO₂ spheres deposited on silicon and reported on a PDMS slice (Figures 5 and 6).

The comparison between the simulated far-field scattering spectra of a TiO₂ particle in vacuum and on silica shows a minor role of the substrate in determining the Mie modes (fig. 2.5 top and central panels): both cases show well-defined resonances at similar wavelengths and having similar nearfield intensity distribution of the electric and magnetic fields (respectively $|E|$ and $|H|$, right panels in fig. 2.5. Beside the effect of the substrates, FDTD simulations clarify the nature of the different modes and we ascribe the resonance at 640, 490, and 400 nm, respectively, to the magnetic dipolar mode, electric dipolar mode and magnetic quadrupolar mode [50, 51].

FDTD simulations can also be used to benchmark the analytical theory (fig. 3.5d), fourth panel from the bottom). From the comparison, we observe a good agreement in the peak positions in both models, whereas we observe few differences in the relative intensities and mode broadenings.

The same FDTD simulation run for a Titania sphere on a Si substrate shows a different picture (fig. 2.5 bottom panels): the two main peaks previously ascribed to

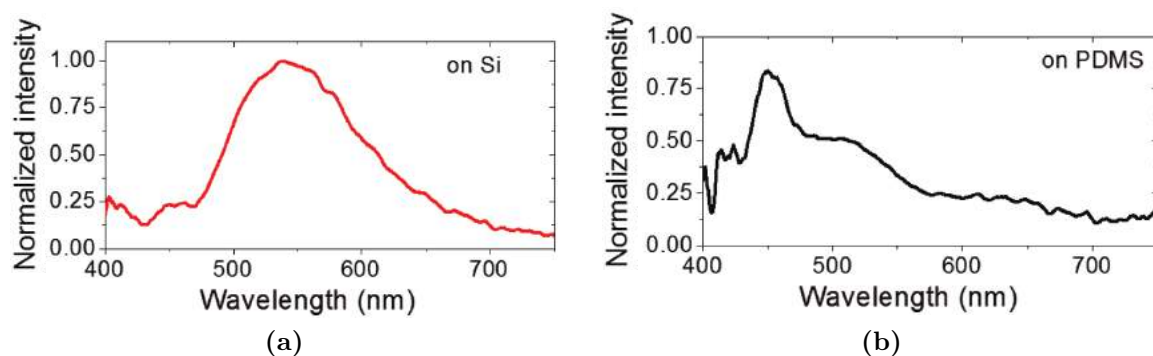


Figure 2.6: Dark-field scattering spectra of the same small particle on a silicon substrate before transfer (a) and after transfer on a PDMS slice (a).

magnetic electric and dipolar modes for the sphere on silica, now appear red-shifted, broadened and spectrally overlapped. Moreover, their near-field distributions present a relevant coupling within the substrate. These effects were predicted for spheres and cylinders made of silicon atop a high-refractive index substrate [47, 50]. However, for TiO_2 spheres, we remark a more pronounced coupling of the magnetic dipolar mode in the underlying silicon substrate with respect to a Si sphere [50]. We ascribe this difference to the reduced refractive index contrast of a TiO_2 sphere on silicon with respect to one made of Si.

Experimental spectra of light scattering of the same TiO_2 particle having a radius of about 120 nm were first measured on a silicon substrate and then, after transfer, on a PDMS slice fig. 2.6. Owing to the different refractive index of the underlying substrates, the spectrum changes as predicted by the FDTD simulations fig. 2.5: from a broad peak at 550 nm on Si, two distinct peaks spring on PDMS, the first one at 450 nm and the second one at about 500 nm.

In the perspective of using this aerosol approach for building structural colors, we show the changes in color response evaluating the 1931 CIE chromaticity coefficients [52] for the scattering in dark-field configuration found in the smaller investigated particles on Si (fig. 2.7, that are the cases of spheres whose spectrum lies in the visible range, r from 96 to 150 nm in fig. 3.5, as colorimetry functions are defined between 380 and 780 nm). In order to assess the scattering colors, the spectra are not normalized to the illumination lamp. In spite of the presence of the high refractive index Si substrate, our Mie resonators show neat colors in the visible range, spanning from blue-green up

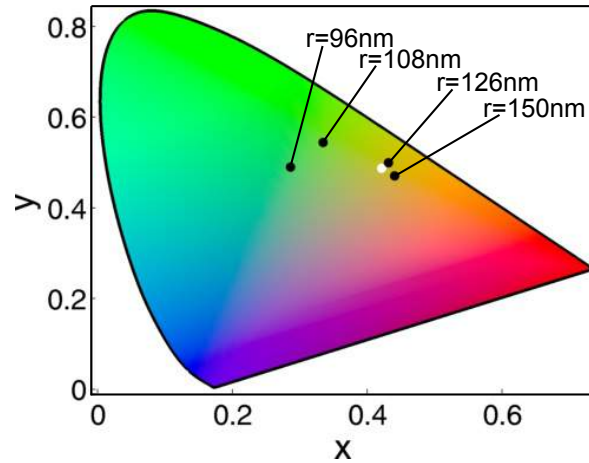


Figure 2.7: CIE chromaticity gamut for light scattering in dark-field configuration (as those shown in fig. 3.5c) for selected TiO₂ spheres with radius ranging from 96 to 150 nm. In these cases the spectra are non-normalized. The position of the light source used for illumination is specified in the map as a white full circle.

to orange of the CIE chromaticity gamut. Thus, even if TiO₂ has a lower refractive index with respect to Si and Ge, Titania spheres have the potential to be exploited for colored metasurfaces [24, 26] in analogy with the group IV counterparts [10, 11, 23, 53–57].

2.3 Conclusions

In conclusion we showed that high-throughput chemical methods, such as aerosol spray, can be used to form Titania-based, sub-micrometric spheres featuring low losses and relatively large refractive index up to blue and near-UV frequencies not accessible by conventional IV–IV compounds. The bright colors at visible frequencies are ascribed to Mie resonances formed within individual spheres, as confirmed by a systematic comparison of the experimental scattering spectra with the theoretical ones.

Theoretical modeling highlights the possibility to obtain a negligible back-scattering, supporting the idea of a Huygens-like source based on individual spheres, an effective isotropic metamaterial toward Yagi-Uda nano-antennas and efficient beam steering in the blue and near-UV frequencies, not accessible with conventional dissipative Si- and Ge-based systems. Nonetheless, the same aerosol method could be exploited for the fabrication of larger particles ($> 1\mu\text{m}$) sustaining whispering gallery modes, for light manipulation with photonic jets [58] or efficient light transport in chains of dielectric

elements [58].

Finally, it is worth mentioning that the versatility of the aerosol technique in use may be adapted for a plethora of applications, as it allows for a direct transformation of the precursors solution in ready-to-use Mie resonators to be sprayed on a surface in a few seconds. In this work, aerosol spray was well adapted to the simultaneous preparation of spheres with very different diameters and the poly-disperse size distribution of the particles would lead to an overall broad-band response of the ensemble. Then our method may be adapted for the production of a structural white paint or, whenever prepared with narrow diameter distribution, and randomly assembled on a substrate by spraying them, for creating a specific metasurface featuring structural colors. To this end, several chemical-related techniques, such as electrospray [59–62], controlled sol-gel colloidal nucleation growth [63, 64], or microfluidic [65] can be exploited to produce TiO_2 particles with much narrower size distribution. Besides, such particles suspension may be used as ink to draw colored pictures by an ink-jet approach, as demonstrated with PMMA particles on fabrics [66]. Since PMMA has a much lower refractive index than TiO_2 , we believe that Titania spheres will be much more adapted to produce structurally colored images over large scale substrates.

2.4 Methods

All chemicals were obtained from Aldrich and used as received. The spherical particles were prepared by atomizing a hydro-alcoholic solution containing 1: TiCl_4 , 20: EtOH and 5: H_2O (molar fractions), in a carrying air flux using a TOPAZ ATM 210 aerosol generator (fig. 2.1).

The nominal size of the droplets varies between 0.1 to several microns. The suspended microdroplets/air mixture passed within a circular furnace at 300 °C for a few seconds to complete evaporation and prestabilization of the dry particles (fig. 2.1). The suspended particles/air mixture was then accelerated at the furnace output using a nozzle and impacted over the target surface (e.g., a Si wafer or a microscope glass slide). This last deposition step lasted for about 10 s preventing the clustering of the particles and keeping their density sufficiently low, thus allowing for spectroscopic in-

2. Spherical TiO₂ Mie resonators: single object investigation

investigation of single objects. The Si wafer sample was then heated at 600 °C for 10 min for densification and crystallization of the spheres. In these configuration droplets of different diameters are generated, which is ideal for the present investigation. Titania particles were transferred from Si to PDMS by gently pressing a PDMS slide for a few seconds on the silicon surface and then peeling it off. A fraction of the spheres were then randomly transferred on the low refractive index PDMS and recognized using predefined marks. The same process is not possible for the SiO₂ case due to technical difficulties (PDMS is sticky whereas glass is not). Thus a direct comparison of the same spheres on Si and on SiO₂ was not possible. However, a systematic investigation of Titania particles on silicon and on a glass slide confirmed the overall picture discussed in the paper (not shown).

In parallel, the same solution was dip-coated using an ACEdip equipment from Sol-gelway to prepare a homogeneous thin layer on a Si wafer. The as-prepared coating was thermally treated in the same conditions, and analyzed by spectroscopic ellipsometry (Woollam M2000V) to extract the (n, k) dispersion used for the analytical model.

Grazing incidence X-ray diffraction (GIXRD) investigation was performed in order to assess composition and crystallinity of the spheres. To this end, the spheres were deposited on a Si wafer for several minutes in order to increase their density without affecting their morphology and heated at 600 °C for 10 min for densification and crystallization. GIXRD patterns were recorded on a conventional diffractometer (PANalytical Empyrean) using Cu radiation ($\lambda = 0.154$ nm), a rapid detector (PANalytical PIXcel) and a parallel plate collimator 0.27°. The incident angle ω was 1.5° (grazing incidence) and the in-plane angle measured from the Si substrate [010] direction was $\phi = 45^\circ$.

The diffraction peaks were fitted by a Gaussian profile function to measure the full width at half maximum (FWHM) of the peaks. In grazing incidence configuration the average crystallite size D (the size of coherent diffracting domains) can be extracted from the FWHM corrected (H_c) from the broadening due to the width of the beam footprint on the sample (H_i), and taking into account the experimental set-up (primary slit in the diffraction plane, goniometer radius, and incident angle): $H_c = (H^2 - H_i^2)^{1/2}$, with H the measured FWHM [67]: $D = 0.89 \lambda / (H_c \cos \theta)$, where θ is the Bragg angle.

Observations by SEM were performed on a FEI Helios 600 NanoLab. Micrographs were acquired using a through-the-lens detector (TLD) secondary electron detector, with a 5 kV acceleration voltage, a probe current of 0.17 nA and a working distance of 4.2 mm.

Spectroscopic measurements were performed on individual spheres to investigate their scattering properties. The spectra were collected by using an optical microscope (LEICA DMI 5000M) mounting a 100 x magnification objective lens (numerical aperture $NA = 0.75$) in dark-field configuration, coupled with a spectrometer and Si-based CCD linear array (Flame-T-VIS-NIR by Ocean Optics). In order to investigate individual spheres, the scattered light coming from each of them was collected using an optical fiber (Ocean Optics multimode fiber, VIS-NIR, core diameter 200 μm).

Spectra from spheres of different radii were analyzed and compared with the expected results from analytical modeling. To this end, the raw experimental spectra were normalized to the excitation light by taking as a reference the spectrum of the light scattered from a dust spot on the sample surface.

Theoretical Models—Analytical Calculations: Theoretical modeling of the spectral properties of the Titania particles was obtained from analytical solutions of Mie scattering from a sphere. They were obtained with an open source code [68]. Excitation and collection geometries were adapted to those used in experiments (figs. 2.3e and 2.3f).

Optical constants (n , k) and particles size used in theory were respectively deduced from ellipsometry and high-resolution SEM images.

Theoretical Models—Finite Difference Time Domain Simulations: Finite difference time domain simulations (FDTD) were performed using a commercial software (Lumerical). The space surrounding the particles was discretized in a 3D grid (resolution 15 nm). The dimensions of the simulation space were $1 \times 1 \times 1 \mu\text{m}$ (in x , y , and z , respectively). The simulation space (substrate in the $\langle xy \rangle$ plane) used periodic boundary conditions on the x and y extrema and absorbing boundary conditions in z .

Light at normal incidence on $\langle xy \rangle$ plane was injected using a broadband plane wave source (source type total field-scattered field). The plane wave was polarized such that the electric field was oriented along the x axis and the magnetic field along the y axis. The near-field distributions were collected by frequency domain monitors in the

2. Spherical TiO_2 Mie resonators: single object investigation

$\langle xz \rangle$ plane (electric field) and $\langle yz \rangle$ plane (magnetic field).

The electromagnetic energy radiated from the resonators was collected by a Poynting monitor box covering all the space surrounding them.

The refractive index used for the Titania composing the particles is that obtained from the experimental ellipsometric measurements.

References

- [1] M. L. Brongersma, Y. Cui, and S. Fan. “Light management for photovoltaics using high-index nanostructures”. In: *Nat. Mater.* 13 (2014), pp. 451–460.
- [2] A. Kuznetsov, A. E. Miroshnichenko, M. L. Brongersma, Y. S. Kivshar, and B. Luk’yanchuk. “Optically resonant dielectric nanostructures”. In: *Science* 354 (2016), pp. 846–853.
- [3] J. S. and J. Z. “All-dielectric metamaterials”. In: *Nat. Nanotechnol.* 11 (2016), pp. 23–36.
- [4] K. Vynck, D. Felbacq, E. Centeno, A. Căbuz, D. Cassagne, and B. Guizal. “All-dielectric rod-type metamaterials at optical frequencies”. In: *Physical review letters* 102.13 (2009), p. 133901.
- [5] A. B. Evlyukhin, C. Reinhardt, A. Seidel, B. S. Luk’yanchuk, and B. N. Chichkov. “Optical response features of Si-nanoparticle arrays”. In: *Physical Review B* 82.4 (2010), p. 045404.
- [6] A. García-Etxarri, R. Gómez-Medina, L. S. Froufe-Pérez, C. López, L. Chantada, F. Scheffold, J. Aizpurua, M. Nieto-Vesperinas, and J. J. Sáenz. “Strong magnetic response of submicron silicon particles in the infrared”. In: *Optics express* 19.6 (2011), pp. 4815–4826.
- [7] J. Van de Groep and A. Polman. “Designing dielectric resonators on substrates: Combining magnetic and electric resonances”. In: *Optics express* 21.22 (2013), pp. 26285–26302.
- [8] I. Staude and J. Schilling. “Metamaterial-inspired silicon nanophotonics”. In: *Nature Photonics* 11.5 (2017), p. 274.
- [9] R. Gomez-Medina, B. Garcia-Camara, I. Suárez-Lacalle, F. González, F. Moreno, M. Nieto-Vesperinas, and J. J. Sáenz. “Electric and magnetic dipolar response of germanium nanospheres: interference effects, scattering anisotropy, and optical forces”. In: *Journal of Nanophotonics* 5.1 (2011), p. 053512.

- [10] X. Zhu, W. Yan, U. Levy, N. A. Mortensen, and A. Kristensen. “Resonant laser printing of structural colors on high-index dielectric metasurfaces”. In: *Science Advances* 3.5 (2017), e1602487.
- [11] T. Wood, M. Naffouti, J. Berthelot, T. David, J.-B. Claude, L. Métayer, A. Delobbe, L. Favre, A. Ronda, I. Berbezier, et al. “All-dielectric color filters using SiGe-based Mie resonator arrays”. In: *ACS photonics* 4.4 (2017), pp. 873–883.
- [12] S. Kim. “Simultaneous determination of refractive index, extinction coefficient, and void distribution of titanium dioxide thin film by optical methods”. In: *Applied optics* 35.34 (1996), pp. 6703–6707.
- [13] T. Siefke, S. Kroker, K. Pfeiffer, O. Puffky, K. Dietrich, D. Franta, I. Ohlídal, A. Szeghalmi, E.-B. Kley, and A. Tünnermann. “Materials pushing the application limits of wire grid polarizers further into the deep ultraviolet spectral range”. In: *Advanced Optical Materials* 4.11 (2016), pp. 1780–1786.
- [14] R. Fenollosa, F. Meseguer, and M. Tymczenko. “Silicon Colloids: From Microcavities to Photonic Sponges”. In: *Advanced Materials* 20 (2008), pp. 95–98.
- [15] M. Garín, R. Fenollosa, R. Alcubilla, L. Shi, L. Marsal, and F. Meseguer. “All-silicon spherical-Mie-resonator photodiode with spectral response in the infrared region”. In: *Nature communications* 5 (2014), p. 3440.
- [16] L. Shi, T. U. Tuzer, R. Fenollosa, and F. Meseguer. “A New Dielectric Metamaterial Building Block with a Strong Magnetic Response in the Sub-1.5-Micrometer Region: Silicon Colloid Nanocavities”. In: *Advanced materials* 24.44 (2012), pp. 5934–5938.
- [17] M. Abbarchi, M. Naffouti, B. Vial, A. Benkouider, L. Lermusiaux, L. Favre, A. Ronda, S. Bidault, I. Berbezier, and N. Bonod. “Wafer scale formation of monocrystalline silicon-based mie resonators via silicon-on-insulator dewetting”. In: *ACS nano* 8.11 (2014), pp. 11181–11190.
- [18] M. Naffouti, T. David, A. Benkouider, L. Favre, M. Cabie, A. Ronda, I. Berbezier, and M. Abbarchi. “Fabrication of core–shell nanostructures via silicon on insulator dewetting and germanium condensation: towards a strain tuning method for

- SiGe-based heterostructures in a three-dimensional geometry”. In: *Nanotechnology* 27.30 (2016), p. 305602.
- [19] M. Naffouti, T. David, A. Benkouider, L. Favre, A. Delobbe, A. Ronda, I. Berbezier, and M. Abbarchi. “Templated Solid-State Dewetting of Thin Silicon Films”. In: *Small* 12.44 (2016), pp. 6115–6123.
- [20] M. Naffouti, T. David, A. Benkouider, L. Favre, A. Ronda, I. Berbezier, S. Bidault, N. Bonod, and M. Abbarchi. “Fabrication of poly-crystalline Si-based Mie resonators via amorphous Si on SiO₂ dewetting”. In: *Nanoscale* 8.5 (2016), pp. 2844–2849.
- [21] M. Khorasaninejad, W. T. Chen, R. C. Devlin, J. Oh, A. Y. Zhu, and F. Capasso. “Metalenses at visible wavelengths: Diffraction-limited focusing and sub-wavelength resolution imaging”. In: *Science* 352.6290 (2016), pp. 1190–1194.
- [22] A. Abarca, P. Gómez-Sal, A. Martín, M. Mena, J. M. Poblet, and C. Yélamos. “Tunable Dielectric Resonator Metasurfaces at Visible Frequencies”. In: *ACS Nano* 10 (2016), pp. 133–141.
- [23] R. C. Devlin, M. Khorasaninejad, W. T. Chen, J. Oh, and F. Capasso. “Broadband high-efficiency dielectric metasurfaces for the visible spectrum”. In: *Proceedings of the National Academy of Sciences* 113.38 (2016), pp. 10473–10478.
- [24] S. Sun, Z. Zhou, C. Zhang, Y. Gao, Z. Duan, S. Xiao, and Q. Song. “All-dielectric full-color printing with TiO₂ metasurfaces”. In: *ACS nano* 11.5 (2017), pp. 4445–4452.
- [25] S. Sun, W. Yang, C. Zhang, J. Jing, Y. Gao, X. Yu, Q. Song, and S. Xiao. “Real-Time Tunable Colors from Microfluidic Reconfigurable All-Dielectric Metasurfaces”. In: *ACS Nano* 12 (2018), pp. 2151–2159.
- [26] T. Bottein, T. Wood, T. David, J. Claude, L. Favre, I. Berbezier, A. Ronda, M. Abbarchi, and D. Grosso. ““Black” Titania coatings composed of sol-gel imprinted Mie resonators arrays”. In: *Adv. Funct. Mater.* (2016).

- [27] T. Bottein, O. Dalstein, M. Putero, A. Cattoni, M. Faustini, M. Abbarchi, and D. Grosso. “Environment-controlled sol–gel soft-NIL processing for optimized titania, alumina, silica and yttria-zirconia imprinting at sub-micron dimensions”. In: *Nanoscale* (2018).
- [28] D. Tzarouchis and A. Sihvola. “Light Scattering by a Dielectric Sphere: Perspectives on the Mie Resonances”. In: *Applied Sciences* 8.2 (Jan. 2018), p. 184.
- [29] A. E. Krasnok, A. E. Miroschnichenko, P. A. Belov, and Y. S. Kivshar. “Huygens optical elements and Yagi—Uda nanoantennas based on dielectric nanoparticles”. In: *JETP letters* 94.8 (2011), pp. 593–598.
- [30] Y. H. Fu, A. I. Kuznetsov, A. E. Miroschnichenko, Y. F. Yu, and B. Luk’yanchuk. “Directional visible light scattering by silicon nanoparticles”. In: *Nature Communications* 4 (2013).
- [31] Y. Zhang, M. Nieto-Vesperinas, and J. J. Sáenz. “Dielectric spheres with maximum forward scattering and zero backscattering: a search for their material composition”. In: *Journal of Optics* 17.10 (2015), p. 105612.
- [32] J. Yan, P. Liu, Z. Lin, H. Wang, H. Chen, C. Wang, and G. Yang. “Magnetically induced forward scattering at visible wavelengths in silicon nanosphere oligomers”. In: *Nature communications* 6 (2015), p. 7042.
- [33] I. Liberal, I. Ederra, R. Gonzalo, and R. W. Ziolkowski. “Superbackscattering from single dielectric particles”. In: *Journal of Optics* 17.7 (2015), p. 072001.
- [34] P. Albella, T. Shibanuma, and S. A. Maier. “Switchable directional scattering of electromagnetic radiation with subwavelength asymmetric silicon dimers”. In: *Scientific reports* 5 (2015), p. 18322.
- [35] M. I. Tribelsky, J.-M. Geffrin, A. Litman, C. Eyraud, and F. Moreno. “Small dielectric spheres with high refractive index as new multifunctional elements for optical devices”. In: *Scientific reports* 5 (2015), p. 12288.
- [36] P. Woźniak, P. Banzer, and G. Leuchs. “Selective switching of individual multipole resonances in single dielectric nanoparticles”. In: *Laser & Photonics Reviews* 9.2 (2015), pp. 231–240.

-
- [37] T. Shibanuma, P. Albella, and S. A. Maier. “Unidirectional light scattering with high efficiency at optical frequencies based on low-loss dielectric nanoantennas”. In: *Nanoscale* 8.29 (2016), pp. 14184–14192.
- [38] A. E. Krasnok, A. Maloshtan, D. N. Chigrin, Y. S. Kivshar, and P. A. Belov. “Enhanced emission extraction and selective excitation of NV centers with all-dielectric nanoantennas”. In: *Laser & Photonics Reviews* 9.4 (2015), pp. 385–391.
- [39] R. S. Savelev, D. S. Filonov, M. I. Petrov, A. E. Krasnok, P. A. Belov, and Y. S. Kivshar. “Resonant transmission of light in chains of high-index dielectric particles”. In: *Physical Review B* 92.15 (2015), p. 155415.
- [40] A. Andres-Arroyo, B. Gupta, F. Wang, J. J. Gooding, and P. J. Reece. “Optical manipulation and spectroscopy of silicon nanoparticles exhibiting dielectric resonances”. In: *Nano letters* 16.3 (2016), pp. 1903–1910.
- [41] J. Yan, P. Liu, Z. Lin, H. Wang, H. Chen, C. Wang, and G. Yang. “Directional Fano resonance in a silicon nanosphere dimer”. In: *Acs Nano* 9.3 (2015), pp. 2968–2980.
- [42] M. I. Tribelsky, J.-M. Geffrin, A. Litman, C. Eyraud, and F. Moreno. “Directional Fano resonances in light scattering by a high refractive index dielectric sphere”. In: *Physical Review B* 94.12 (2016), p. 121110.
- [43] T. Coenen, J. V. D. Groep, and A. Polman. “Resonant Modes of Single Silicon Nanocavities Excited by Electron Irradiation”. In: *ACS nano* 7 (2013), pp. 1689–1698.
- [44] H. Němec, C. Kadlec, F. Kadlec, P. Kužel, R. Yahiaoui, U.-C. Chung, C. Elissalde, M. Maglione, and P. Mounaix. “Resonant magnetic response of TiO₂ microspheres at terahertz frequencies”. In: *Applied Physics Letters* 100.6 (2012), p. 061117.
- [45] M. Navarro-Cía, M. Natrella, F. Dominec, J.-C. Delagnes, P. Kužel, P. Mounaix, C. Graham, C. Renaud, A. Seeds, and O. Mitrofanov. “Terahertz imaging of sub-wavelength particles with Zenneck surface waves”. In: *Applied Physics Letters* 103.22 (2013), p. 221103.

- [46] A. B. Evlyukhin, S. M. Novikov, U. Zywietz, R. L. Eriksen, C. Reinhardt, S. I. Bozhevolnyi, and B. N. Chichkov. “Demonstration of magnetic dipole resonances of dielectric nanospheres in the visible region”. In: *Nano letters* 12.7 (2012), pp. 3749–3755.
- [47] P. Spinelli, M. Verschuuren, and A. Polman. “Broadband omnidirectional antireflection coating based on subwavelength surface Mie resonators”. In: *Nature Communications* 3 (2012), p. 692.
- [48] M. Kerker, D.-S. Wang, and C. Giles. “Electromagnetic scattering by magnetic spheres”. In: *JOSA* 73.6 (1983), pp. 765–767.
- [49] D. L. Markovich, P. Ginzburg, A. K. Samusev, P. A. Belov, and A. V. Zayats. “Magnetic dipole radiation tailored by substrates: numerical investigation”. In: *Optics express* 22 (2014), p. 10693.
- [50] B.-I. Popa and S. A. Cummer. “Compact dielectric particles as a building block for low-loss magnetic metamaterials”. In: *Physical review letters* 100.20 (2008), p. 207401.
- [51] S. Person, M. Jain, Z. Lapin, J. J. Saenz, G. Wicks, and L. Novotny. “Demonstration of zero optical backscattering from single nanoparticles”. In: *Nano letters* 13.4 (2013), pp. 1806–1809.
- [52] T. Smith and J. Guild. “The C.I.E. colorimetric standards and their use”. In: *Transactions of the Optical Society* 33.3 (1931), pp. 73–134.
- [53] W. Yue, S. Gao, S.-S. Lee, E.-S. Kim, and D.-Y. Choi. “Highly reflective subtractive color filters capitalizing on a silicon metasurface integrated with nanostructured aluminum mirrors”. In: *Laser & Photonics Reviews* 11.3 (2017).
- [54] V. Vashistha, G. Vaidya, P. Gruszecki, A. E. Serebryannikov, and M. Krawczyk. “Polarization tunable all-dielectric color filters based on cross-shaped Si nanoantennas”. In: *Scientific Reports* 7.1 (2017), p. 8092.
- [55] C.-S. Park, V. R. Shrestha, W. Yue, S. Gao, S.-S. Lee, E.-S. Kim, and D.-Y. Choi. “Structural color filters enabled by a dielectric metasurface incorporating hydrogenated amorphous silicon nanodisks”. In: *Scientific Reports* 7.1 (2017), p. 2556.

-
- [56] V. Neder, S. L. Luxembourg, and A. Polman. “Efficient colored silicon solar modules using integrated resonant dielectric nanoscatterers”. In: *Applied Physics Letters* 111.7 (2017), p. 073902.
- [57] V. Flauraud, M. Reyes, R. Paniagua-Dominguez, A. I. Kuznetsov, and J. Brugger. “Silicon nanostructures for bright field full color prints”. In: *ACS Photonics* 4.8 (2017), pp. 1913–1919.
- [58] Z. Chen, A. Taflove, and V. Backman. “Photonic nanojet enhancement of backscattering of light by nanoparticles: a potential novel visible-light ultramicroscopy technique”. In: *Optics express* 12 (2004), pp. 1214–1220.
- [59] L. Ding, T. Lee, and C.-H. Wang. “Fabrication of monodispersed Taxol-loaded particles using electrohydrodynamic atomization”. In: *Journal of Controlled Release* 102.2 (2005), pp. 395–413.
- [60] Y. Hong, Y. Li, Y. Yin, D. Li, and G. Zou. “Electrohydrodynamic atomization of quasi-monodisperse drug-loaded spherical/wrinkled microparticles”. In: *Journal of Aerosol Science* 39.6 (2008), pp. 525–536.
- [61] N. Bock, M. A. Woodruff, D. W. Hutmacher, and T. R. Dargaville. “Electrospraying, a reproducible method for production of polymeric microspheres for biomedical applications”. In: *Polymers* 3.1 (2011), pp. 131–149.
- [62] N. Bock, T. R. Dargaville, and M. A. Woodruff. “Electrospraying of polymers with therapeutic molecules: state of the art”. In: *Progress in polymer science* 37.11 (2012), pp. 1510–1551.
- [63] M. Keshmiri and T. Troczynski. “Synthesis of narrow size distribution sub-micron TiO₂ spheres”. In: *Journal of Non-Crystalline Solids* 311.1 (Oct. 2002), pp. 89–92.
- [64] S. Li, Q. Shen, J. Zong, and H. Yang. “Simple preparation of sub-micron mesoporous TiO₂ spheres consisting of anatase nanocrystals”. In: *Journal of Alloys and Compounds* 508.1 (Oct. 2010), pp. 99–105.
- [65] K. Shiba and M. Ogawa. “Microfluidic syntheses of well-defined sub-micron nanoporous titania spherical particles”. In: *Chemical Communications* 44 (2009), p. 6851.

2. Spherical TiO₂ Mie resonators: single object investigation

- [66] G. Liu, L. Zhou, G. Zhang, Y. Li, L. Chai, Q. Fan, and J. Shao. “Fabrication of patterned photonic crystals with brilliant structural colors on fabric substrates using ink-jet printing technology”. In: *Materials & Design* 114 (Jan. 2017), pp. 10–17.
- [67] D. Simeone, G. Baldinozzi, D. Gosset, S. L. Caer, and J.-F. Bérar. “Grazing incidence X-ray diffraction for the study of polycrystalline layers”. In: *Thin Solid Films* 530 (Mar. 2013), pp. 9–13.
- [68] <http://www.philiplaven.com/mieplot.htm>.

Chapter 3

Multifunctional photonic devices with Titania-based metasurfaces

After assessing the scattering properties of individual Titania spheres this chapter addresses a second case of viable solution for high throughput fabrication for dielectric metasurfaces. Here sol-gel deposition and nanoimprint lithography are used to obtain Titania-based Mie resonators over the record size of mm^2 , showing that this platform can potentially be exploited for different multifunctional light management devices. First, it's demonstrated their use for structural colours and band pass filters in the visible region. Then, exploiting Fano resonances in reflection, it's shown their potential for refractive index sensing, obtaining a figure of merit of ~ 20 . Finally, when placing the Titania-based Mie resonators on porous silica, a large and reversible color change rises as a result of water adsorption within the material porosity. These results open the path to Titania submicrometric structures for applications as a multifunctional metamaterial for smart windows, displays and all-optical sensing.

3.1 Introduction

Dielectric metasurfaces composed of high-permittivity and sub-micrometric elements [1, 2] (dielectric Mie resonators) are challenging photonic structures [3–5] for light manipulation at visible and nearinfrared frequencies thanks to their peculiar performances associated to reduced ohmic losses and a higher compatibility with electronic

3. Multifunctional photonic devices with Titania-based metasurfaces

devices. Anti-reflection coatings [6], mirrors [7, 8], lenses [9], polarisers [10], wave-front shaping [11–13], sensing [14, 15] and non-linear phenomena [16–19] are few examples demonstrating the strength of this approach for light management with sub-wavelength dielectric-structures. However, with a few exceptions based on colloidal assembly [20–22], hydrothermal growth [19], solid state dewetting [23–29] and aerosol spray [30], most of these achievements were based on complex and expensive fabrication methods involving several steps (such as e-beam lithography and reactive ion etching), thus limiting their extensive adoption in realistic devices and over broad areas. In particular, given the rapidly rising interest in structural colouring and light filtering with dielectric metasurfaces [31–40] a versatile and scalable method is highly desirable to overcome the gap separating mere proof of principles and industrial applications. For instance, in this framework, a major step forward will be the use of fabrication techniques that are also fully compatible with back-end processing of C-MOS circuitry (e.g. keeping the maximal processing temperature below ~ 450 °C) or more generally, on electronic devices such as LEDs and photovoltaic panels. More generally, a metasurface providing several functions (e.g. tuneable structural colour, sensing small changes in the environment), could be employed as a realistic photonic platform for multifunctional devices.

Thanks to its transparency up to near-UV frequencies and its relatively high refractive index, TiO_2 (Titania) is an excellent material candidate to implement Mie resonators systems [31, 34, 41–44] that can potentially outperform conventional Si- and Ge-based dielectric metasurfaces which suffer from larger absorption at short wavelength [45, 46] (e.g. at 450 nm: $n_{\text{TiO}_2} = 2.55$, $k_{\text{TiO}_2} = 1.2 \cdot 10^{-5}$; $n_{\text{Si}} = 4.5$, $k_{\text{Si}} = 0.13$; $n_{\text{Ge}} = 4$ and $k_{\text{Ge}} = 2.24$). Another relevant advantage of Titania with respect to conventional Si and Ge and metals is its porosity (adjustable by modifying the sol-gel fabrication process) rendering it permeable to liquids and gases. In addition to this, Titania is an abundant, cheap, nontoxic, photo-catalytic, mechanically strong and chemically stable material, featuring a relatively low mass density (~ 3.8 g/cm³ in the anatase form against ~ 5 g/cm³ for MoS_2). Developing a method for large-scale fabrication of Titania on ultra-low per-area mass supports (such as aerogels), would potentially render this material a competitive candidate for light-sails to be employed

in future space exploration [47]. However, in spite of several reports on Titania-based Mie resonators, the implementation of sub-micrometric structures with conventional methods (e.g. e-beam or optical lithography and reactive ion etching) remains limited to small size and hardly scalable. In the precedent chapter, we reported the use of sol-gel chemistry combined with aerosol-spray processing to elaborate Titania sub-micron spheres and investigate their scattering properties on various substrates. This chemistry was also coupled to nano-imprint lithography (soft-NIL) process to form Titania-based Mie resonator arrays [43, 44].

Here, exploiting soft-NIL in porous Titania, we show that tailored dielectric metasurfaces can be extended over large areas up to mm^2 . Then we focus on four different applications.

- A fine size tuning of the resonant elements constituting the dielectric arrays provides neat structural diffusive colors, covering the full visible spectrum.
- The same arrays are proved to act as sharp band-pass filters (up to ~ 40 dB rejection ratio) when impinged by light channeled in the glass slide on which they are printed. The central frequency and band pass can be controlled by designing the dielectric arrays, with potentially interest for optical displays.
- Fano resonances spring from the reflection from the arrays thanks to the interference between sharp grating modes and the broad-band reflection. These resonances allow for a sensitive monitoring of the optical response of the metasurface to slight refractive index changes. We demonstrate a sensitivity (S , spectral shift $\delta\lambda$ over refractive index change δn) of ~ 50 nm/RIU (where RIU represents the refractive index unit) and a figure of merit ($FOM = S/\Gamma$, where Γ is the full width at half maximum of the resonance) exceeding 20.
- Finally, our method can be adapted for dynamic structural colour change by coupling the Titania-based Mie resonators onto a highly porous hydrophilic silica layer deposited on bulk silicon. In these conditions, a reversible spectral shift of about 100 nm (from green-yellow to orange-red) was obtained by varying the refractive index of the underneath porous silica layer between 1.28 and 1.37 using humidity.

3.2 Results

Arrays of TiO_2 sub-micrometric squared pillars are obtained via soft-NIL by following a well established method. Further details are provided in the devoted section section 3.5.1. The master was obtained by e-beam lithography and reactive ion etching on a bulk silicon wafer and was composed of 9 arrays of 150 nm wide trenches milled with variable pitch ($p = 380, 400, 420, 440, 460, 480, 500, 550$ and 600 nm) in a squared geometry and extending over 1 mm^2 (fig. 3.1a). A hard polydimethylsiloxane (PDMS) mould is obtained from the master and used *ad libitum* to replicate its features on freshly deposited sol-gel Titania (moulds have been used dozen of times over several months, without damages. Their lifetimes were not investigated in this work). The Titania replicas are extremely regular as accounted for by scanning electron microscopy (SEM) and atomic force microscopy (AFM) investigations, showing fluctuations of the structural parameters of a few % (figs. 3.1, 3.2a and 3.2b). An

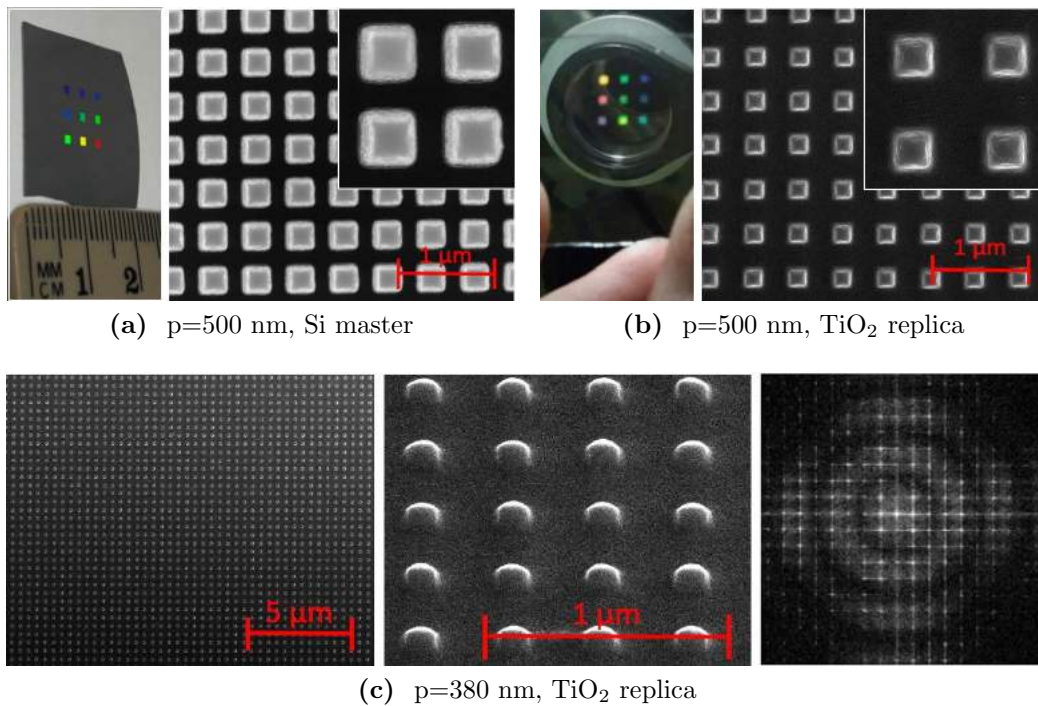


Figure 3.1: **a)** Left panel: photo of the Si master. Right panel: SEM image of the Si master (pitch $p = 500$ nm). **b)** Left panel: photo of the TiO_2 replica. Right panel: SEM image of the TiO_2 replica (pitch $p = 500$ nm). **c)** Left panel: large-scale SEM image of TiO_2 replica ($p = 380$ nm). Middle panel: blow up of the same pattern ($p = 380$ nm) view with a tilt angle of 45 degrees. Right panel: Fourier transform of the left panel.

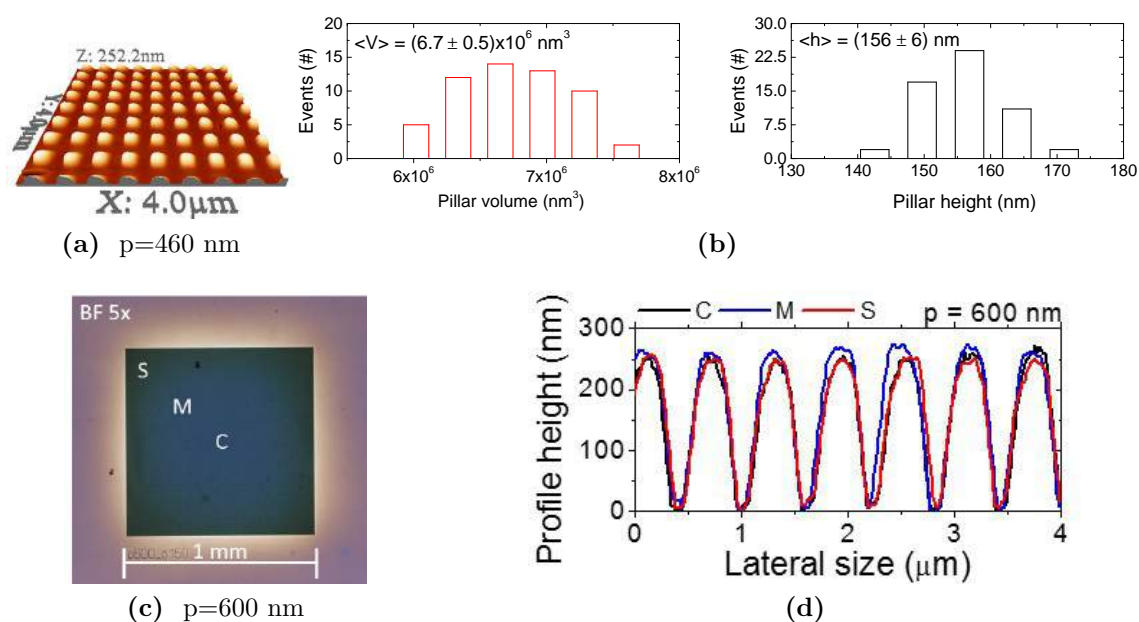


Figure 3.2: **a)** Bird eye 3D view of an AFM image of the TiO_2 replica ($p = 460 \text{ nm}$). **b)** Statistic of the pillar volume (left) and height (right). **c)** Optical microscope image (bright field, 5x magnification, $p = 600 \text{ nm}$). **d)** Height profiles of three AFM images taken at the center of the array (C), at mid diagonal (M) and at the corner (S), as highlighted in fig. 3.2c.

extensive analysis of these morphological images confirms a coherent replication across the arrays (figs. 3.2c and 3.2d). We investigate the light scattering from the dielectric arrays exploring their possible use for structural colour in conventional diffusion (e.g. for ink-free color printing and anti-counterfeiting of banknotes). A tungsten white lamp is used for dark-field illumination in an optical microscope (the scheme of the illumination/collection geometry and of the lamp spectrum are shown in figs. 3.3a and 3.3b, respectively). Dark-field backscattering spectra (DF, non-normalized to the white tungsten lamp spectrum, nor background subtracted; the objective lens was 20x magnification, $\text{NA} = 0.4$ determining a maximum acceptance angle of ~ 23 degrees), show the onset of sharp resonances red-shifting and increasing in number with increasing pitch size (fig. 3.3c). These resonances are attributed to the presence of multipolar Mie modes formed within the Titania pillars as already found in similar systems [48]. An extensive characterization of this kind of devices and an assessment of the nature of their resonant modes can be found in recently published papers [30, 34, 42, 49, 50]. Although a rigorous attribution of the resonances to multi-polar modes is possible only for spherical particles [30], comparing small objects ($p < 460 \text{ nm}$, having base size smaller

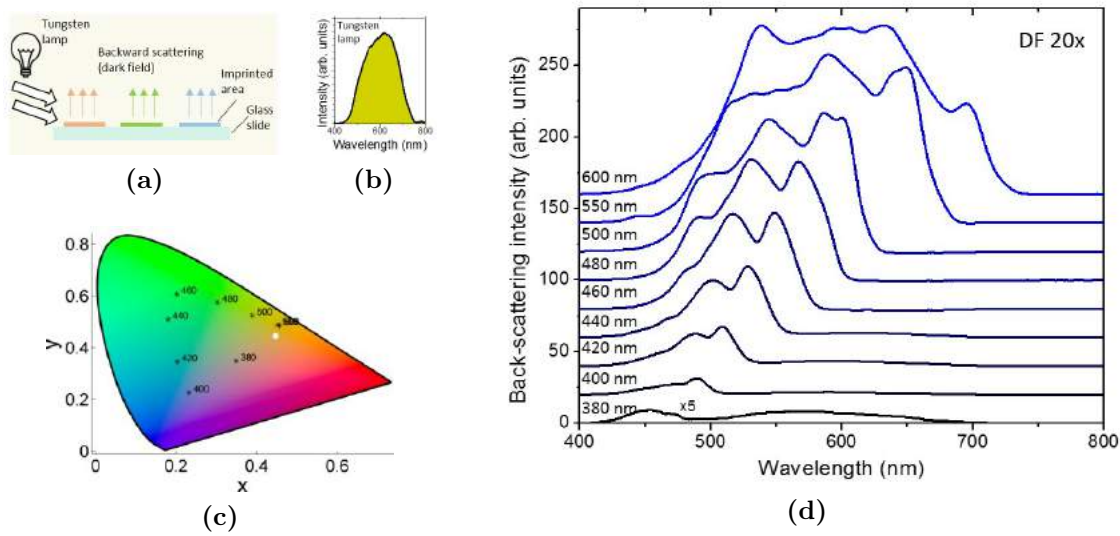


Figure 3.3: **a)** Scheme of the dark-field illumination. **b)** Tungsten lamp spectrum used in this illumination geometry. **c)** CIE chromaticity gamut obtained from spectra in **d)**. The white dot represent the color of the white lamp used for illumination. **d)** Dark-field back-scattering spectra collected with a 20x objective lens from a $\sim 15 \mu\text{m}$ spot. The spectra for pitch ranging from $p = 380$ up to $p = 600$ nm are vertically shifted for clarity and are not normalized to the white tungsten lamp used for illumination.

than ~ 250 nm) with Titania Mie resonators featuring similar size and shape [34, 42], we attribute the longer-wavelength resonance to the magnetic dipolar mode, and the second one to the electric dipolar mode. For larger pillars, the scattering spectrum becomes more complicate and a clear discrimination between the different resonances is not possible owing to the onset of higher order modes, as expected in this kind of systems. Note that a weak spurious scattering of the white illumination light is visible in the spectrum of the small pitches (the broad band peaked at ~ 580 nm), due to their rather low scattering in the visible. The two largest pitches ($p = 550$ and 600 nm) with larger pillars accommodating several Mie resonances show a bandwidth comparable to that of the white tungsten lamp. Overall, the nine arrays cover the visible spectrum from blue to orange (fig. 3.3d). We would like to stress that such scattering modes differ from the sharp spectral features characteristic of a simple diffraction grating. To underline this concept, fig. 3.4 shows the characterization of the angular-resolved specular reflection of one of the printed arrays ($p = 380$ nm). Using a collimated beam for excitation and detecting only the specular reflection from the array $p = 380$ nm we observe 6 narrow peaks. Collecting the reflection parallel to the pillars sides (that is from the Γ to the X point in the first Brillouin zone of a square photonic lattice)

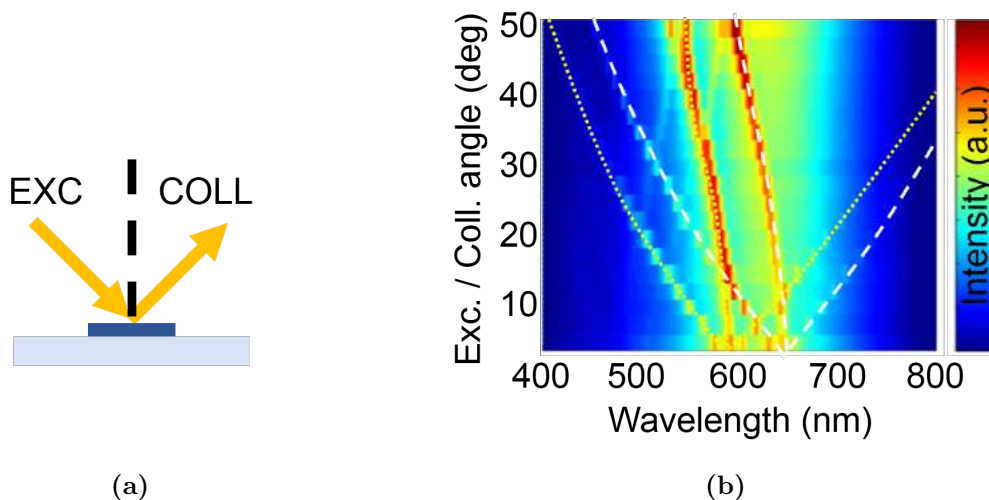


Figure 3.4: **a)** Scheme of the specular reflection geometric configuration. **b)** Specular reflection as a function of wavelength (x axis) and excitation/collection angle (y axis) represented as a color intensity map. The spectra are not normalized nor background-subtracted and are collected over a ~ 1 mm spot. The excitation source was a collimated beam. The white dashed and yellow dotted lines are guides to the eyes highlighting the triplets of TE and TM modes, respectively. The top right inset represents the excitation collection geometry.

the narrow bands are characterized by a specific shift with excitation/collection angle. These modes are characteristic of a 2D high-index contrast grating (a wavelength-scale two-dimensional photonic membrane) with a square geometry (see Sakoda, K. (2004) “Optical properties of photonic crystals (Vol. 80)” Springer Science and Business Media). Note that these spectral features are completely different with respect to those occurring at shorter wavelength and previously identified with the Mie modes (see the data relative to the same array $p = 380$ nm in fig. 3.3d).

Changing the illumination condition and light source, we now address the light filtering from the dielectric arrays exploring their scattering properties for applications in displays. Exploiting the glass slide supporting the arrays, we address their scattering in air of the guided slab modes. We channel the light emitted by a white LED within the slab detecting the light out-coupled by the Mie resonators arrays from the top (figs. 3.5a and 3.5b). With a smart-phone camera, we take images of the pillars arrays showing marked structural colours both in the front and back sides (fig. 3.5c). Spectra registered from the top part (front side scattering) are represented in a semi-logarithmic scale in order to highlight the sharp pass band operated on the LED light (fig. 3.5d);

3. Multifunctional photonic devices with Titania-based metasurfaces

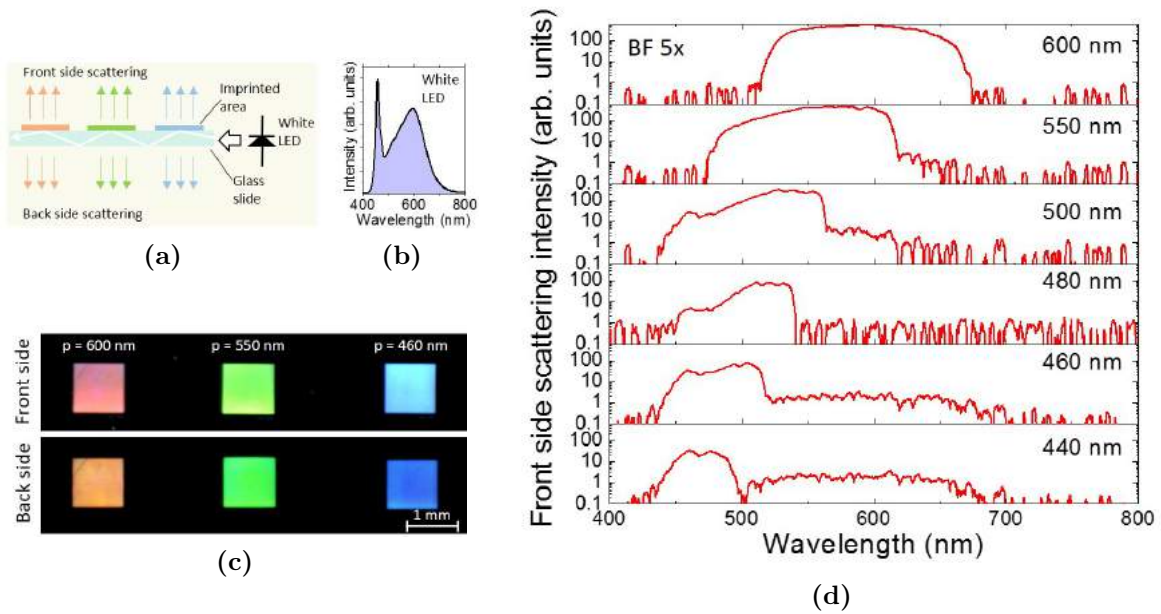


Figure 3.5: **a)** Scheme of the illumination of the Titania arrays through the glass slab. The source was a white LED. **b)** White LED spectrum used for illumination. **c)** Smart-phone camera pictures of the front side (top panel) and back side (bottom panel) scattering. **d)** Spectra of the white light out-coupled through the Titania arrays having pitch p larger than 440 nm. The spectra are detected in bright field collection with a 5x objective lens from a $\sim 60 \mu\text{m}$ spot.

the spectra are not normalized to the LED light, nor background-subtracted). For the largest pitches ($p > 500$ nm) we observe a rejection exceeding 1/1000 of the light out of the pass band (rejection up to 37 dB for $p = 600$ nm) whereas the smaller pitches ($p < 440$ nm) were not visible in this illumination/collection geometry. The data shows that the central frequency and, possibly, the bandwidth, can be controlled by design of the array.

As said in the introduction, the use of sol-gel chemistry allows to have porous Titania, leading to several possible uses, obviously including the sensing via small changes of the refractive index by any analyte in the pores. As proof of principle of the sensor, we use water infiltration of the Titania matrix composing the pillars and detect the reflection with a conventional bright field illumination geometry. In this case, the tungsten lamp light is shined from the top and collected through the same 5x objective lens, thus accessing the reflection from the arrays integrated over the numerical aperture of the optics ($\text{NA} = 0.2$ corresponding to a maximum acceptance angle of about 11 degrees, fig. 3.6a). The reflectance spectra are dominated by broad bands associated

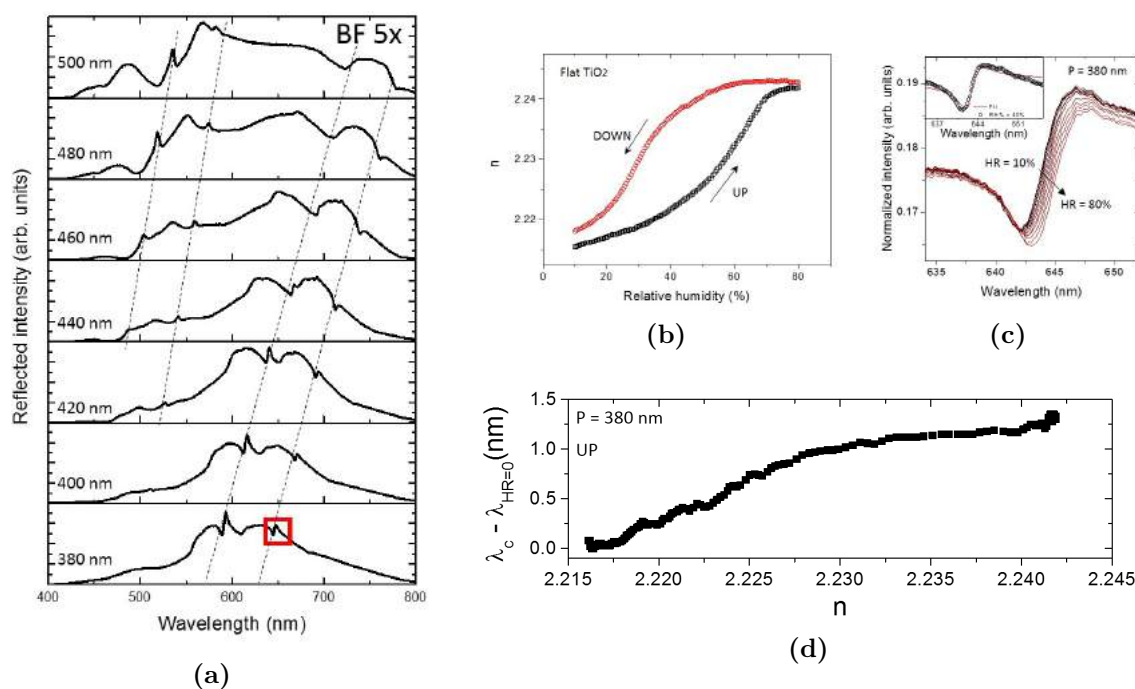


Figure 3.6: **a)** Reflection spectra detected in bright field illumination/collection with a 5x objective lens from a $\sim 60 \mu\text{m}$ spot for $p = 380$ up to $p = 500$ nm. The spectra are not normalized to the hite tungsten lamp, nor background subtracted. The dashed lines are guides to the eyes highlighting the position of sharp resonances. **b)** Refractive index changes as a function of the environmental relative humidity (RH%) measured on the flat Titania nearby the pillars arrays. Black (red) symbol indicate increase (decrease) of RH%. **c)** Fano-like profiles as a function of wavelength for increasing RH% for $p = 380$ nm (highlighted by a red square in a). The inset show the case of RH = 60% with the corresponding fit with a Fano profile function. **d)** Spectral shift $\lambda_C - \lambda_{RH=0}$, as extracted from the fit of the experimental data (e.g. as in the inset of c) relative to a ramp of RH from 10% up to 80%. Data are relative to the Fano profile at ~ 645 nm (highlighted by a red square in a).

to the Mie modes, which red-shift with increasing pillars' size. Note also that relevant spectral differences can be found in different scattering geometry (figs. 3.3, 3.5 and 3.6), due to the peculiar angular patterns of different Mie modes. In addition to this, we also observe narrow resonances which line-shape can be either a Lorentzian or a Fano-like dispersive profile [51], depending on their relative intensity with respect to the broad Mie bands. These sharp spectral features are characteristic of a 2D high-index contrast grating and arise from interference of light due to the ordering of the Mie resonators in a two dimensional photonic crystals. This is a common photonic phenomenon and it has been observed in a plethora of systems including dielectric and plasmonic ordered structures [52, 53].

3. Multifunctional photonic devices with Titania-based metasurfaces

Fano line-shapes characterized by a dispersive-like profile are suitable for detecting small spectral shifts induced by refractive index changes. Exploiting the nano-porosity of the dense Titania composing the pillars (estimated around 8% vol), we induce a slight change in their refractive index by varying the relative humidity (RH%) of the surrounding atmosphere from 10% to 80%. These changes are measured by environmental ellipsometry on the flat Titania film nearby the arrays. Adsorption and desorption of water within the pores follows a different kinetics, which is reflected in the typical hysteresis cycle in the measured refractive index on the 2D, flat Titania layer nearby the arrays (fig. 3.6b) [54]. The study of the hysteresis can lead to get insights into the complex dynamics of water in the Titania nanopores, which is largely outside the scope of this work. In view of application this complexity is not a limit, since it is possible to reset the system at the initial conditions (no water) by heating the device at 200 °C for 10 minutes, thus reproducing the same variation of refractive index in the following humidity cycle (not shown). From this analysis we can also deduce a broad distribution of pore size with an average value centered at about 2.5 ± 0.5 nm.

By fitting the Fano profiles for increasing RH%, we can precisely evaluate the central wavelength λ_C and the line-width Γ of the Fano resonance evolving under different RH% (fig. 3.6c). In this analysis we neglect the cases $\text{RH}\% < 10\%$, as the humidity detector is not sensitive below this value, and $\text{RH}\% > 80\%$, owing to water condensation on the sample surface. Provided a spectral shift of about 1.3 nm against a refractive index variation of ~ 0.027 (fig. 3.8) and a line-width Γ of ~ 2.7 nm, we evaluate an overall sensitivity $S = \delta\lambda/\delta n$ of about 50 nm/RIU and a figure of merit ($\text{FOM} = S/\Gamma$) of ~ 20 .

As a last example of possible use of this metasurface platform, we show a dynamic colour change tuned by modulating the refractive index of a porous silica underneath the Titania arrays. This is obtained by printing the dense Titania pillars ($p = 1500$ nm) atop a mesoporous silica layer (~ 650 nm thick, pore size ~ 7 nm, porosity estimated around 37% vol) deposited via sol-gel on a silicon substrate (a scheme of the sample structure is shown in the inset of fig. 3.7a) and infiltrating water in the pores. As for the previous case, during a humidity cycle the refractive index of the dense TiO_2 shows a rather small variation, whereas that one of the porous silica is about five times larger ($\Delta n(\text{TiO}_2) \sim 0.025$, $\Delta n(\text{SiO}_2) \sim 0.11$, Fig.5 a). In the present case, the refractive

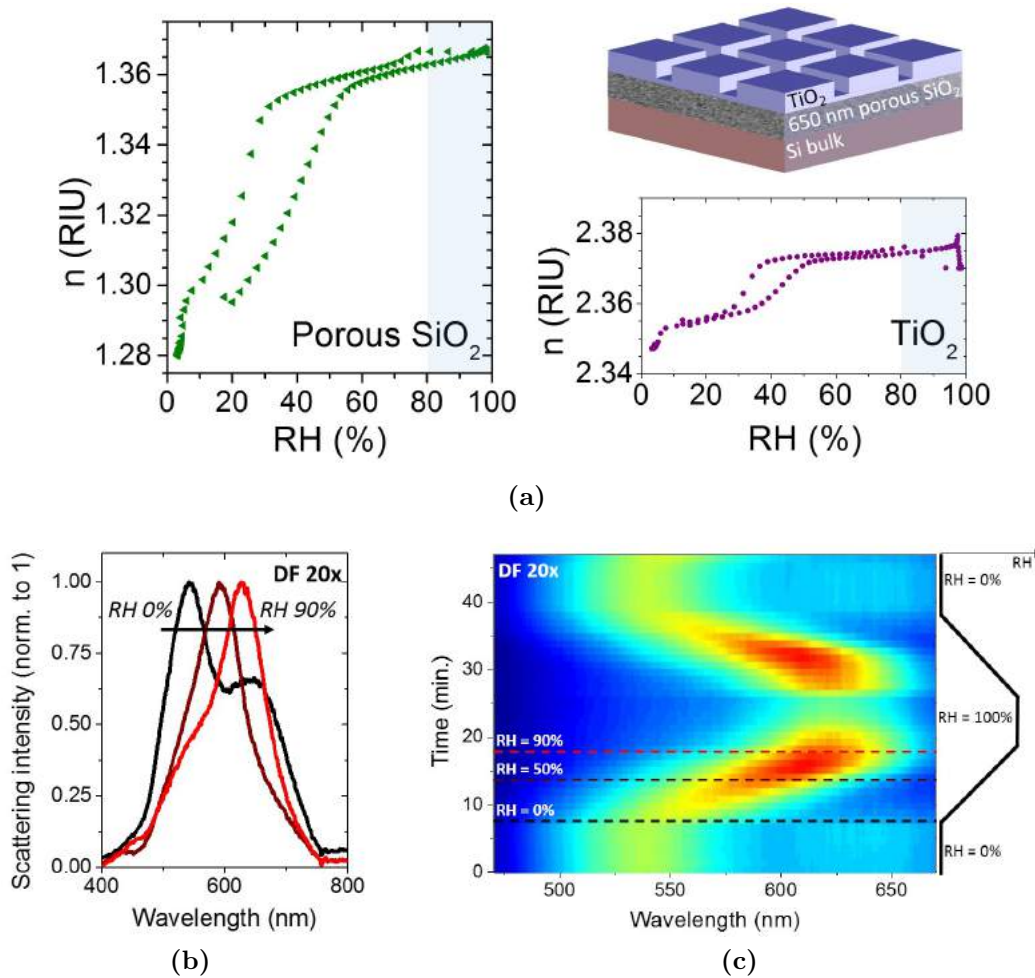


Figure 3.7: **a)** Left (right) panel: refractive index changes for the porous SiO_2 (TiO_2) as a function of the relative humidity RH% measured in flat 2D areas nearby the pillars arrays. For RH% > 80% (shaded light blue area) water condensates on the sample surface. The sketch in the top panel shows a sketch of the sample structure. **b)** Dark-field scattering spectra for a Titania array ($p = 1500$ nm) at increasing relative humidity. The spectra are not normalized to the white tungsten lamp used for illumination, nor background subtracted. **c)** Colour-intensity maps of dark-field spectra as a function of wavelength (x axis) and time (or humidity cycle, y axis). The horizontal dashed lines correspond to the position of the spectra shown in **b)**. A scheme of the humidity cycle as a function of time is shown on the right part.

index of the TiO_2 is slightly higher compared to the previous system (fig. 3.6). This is ascribed to the higher annealing temperature applied to consolidate the sol-gel bi-layers after NIL.

By following the spectral shift of the main resonance measured in dark-field geometry, we observe an overall red-shift of about 100 nm when increasing humidity from 0% to 80% (fig. 3.7b), the spectra are not normalized to the white tungsten lamp used for illumination). The spectra acquired over a full humidity cycle are represented as a

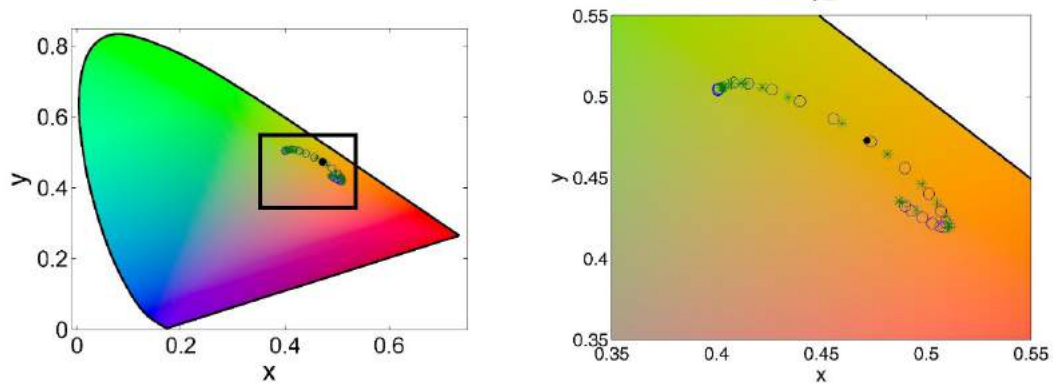


Figure 3.8: Left panel: CIE gamut of the non-normalized spectra shown in c. Circles (stars) indicate increasing (decreasing) RH%. Right panel: blow up of the relevant part of the gamut shown on the left panel. The open circle indicates the initial and final point of the cycle. The black dot represents the white lamp.

colour-intensity map showing a bleaching of the scattering for $RH > 80\%$ owing to water condensation (fig. 3.7c). The color-change dynamics represented on the CIE gamut shows a large and reversible behavior from yellow-green up to orange-red (fig. 3.8). As a consequence of the large broadening of the resonances, in this set of data, the hysteresis cycle is not visible.

3.3 Discussion

Sub-wavelength dielectric structures were implemented on mm-scales by using Titania, a material having a relatively high refractive index and high transparency up to near-UV frequencies, rendering it an ideal platform for manipulating GaN-based LED light. In this sense, this result is important as they extend the range of use of dielectric Mie resonators to frequencies not attainable by Si and Ge owing to their larger extinction coefficient. This method is implemented at relatively low temperature ($\sim 450^\circ\text{C}$, but lower values are in principle possible), potentially rendering it compatible with back-end processing of C-MOS circuitry [55] with the additional advantage of relaxing the need of cumbersome fabrication steps (e.g. a device can be finalized in less than one hour in a laboratory).

We also showed the possibility to fabricate these photonic structures directly on highly porous silica (aerogel layer) having low-index and low weight. Although in the present case we used a mesoporous silica (porosity $\sim 37\%$ vol, mass density 1.7 g/cm^3),

sol-gel process can also be used to form layers of MgF_2 featuring a porosity of 80%, thus providing a very low refractive index (~ 1.08) and mass density ($\sim 0.6 \text{ g/cm}^3$) [56].

Although in this work we addressed the simple case of squared pillars, the high fidelity in the replication over mm-scales and the high lateral resolution (the smaller objects have a side of about 150 nm) allow, in principle, the implementation of advanced devices made of unit cells having sharp features and more complex geometries. This opens the possibility to use soft-NIL for the production of large scale metasurfaces with more exotic optical properties and advanced functionalities [9–15].

These devices can be exploited for several uses accounting for the multifunctionality of Titania based metasurfaces. Neat structural colours spring from scattering by multipolar Mie modes formed within the dense Titania pillars, in analogy to what was found in similar systems [31–40]. Choosing a convenient illumination geometry, where the light of a white LED is coupled within the glass slide, only the fundamental modes of the Mie resonators are illuminated and can out-couple the light from the slab. This is due to the larger coupling of these resonances with the substrate with respect to higher order multi-polar modes that are more strongly confined within the pillars [6, 29, 30, 48, 57] and do not appear in the spectra. This property provides sharp band-pass filters potentially important for the use of these devices as ink-free colours and displays, although in this case a large dynamic tuning of the structural colour is not possible.

In back scattering geometry at normal incidence we observe sharp Fano resonances [51] due to the ordering of the Mie resonators array. Exploiting this sharp spectral line together with the porosity of sol-gel materials, we show that our structures can be suitable for refractive index sensing. We obtain a figure of merit of about 20 which is not very far from what found in the plasmonic counterpart [58, 59]. Our system was not optimized for efficient sensing and better performances could be in principle obtained by using a different excitation/collection configuration or changing the unit cell geometry (see for instance reference [14] where a FOM of ~ 100 was demonstrated). However, the important point here is that the “sensing” occurs within the volume of the Mie resonators, where the water is adsorbed and the intensity of the electromagnetic field is larger [19, 28, 29, 48]. This observation opens up the possibility of functionalizing

the sol-gel with chemical compounds in order to detect specific substances present in the atmosphere or in solution as demonstrated for other sol-gel-based systems⁶⁰. This option is not readily available for conventional Si- and Ge-based Mie resonators which use in sensing or enhanced Raman scattering requires more complex device geometries (such as Mie resonators molecules) where the hot-spots of the electromagnetic field lie outside the pillars.

A large, dynamic and reversible colour change can be obtained when placing the Titania pillars on porous silica and exploiting its large refractive index change (Δn of about 0.11) upon water uptake. The spectral shift of about 100 nm exceeds of about two times what was previously reported on active tuning mechanisms in similar systems [50, 60, 61] and is obtained with a much simpler device. As a first approximation, such a large shift can be simply ascribed to an interference effect springing from the refractive index changes in the porous medium leading to a different illumination of the scatterers. A smaller effect may spring from the coupling of the Mie modes within the substrate [57]. Such a device represents an important example of the flexibility and strength of the sol-gel/NIL approach in coupling different materials featuring different physical properties and giving access to novel functions.

3.4 Conclusion

In conclusion we have implemented record-size arrays of Mie resonators based on Titania with a high-throughput and low temperature method, combining bottom-up assembly via sol-gel deposition and top-down nano-imprint lithography. We presented several possible applications of our platform, such as structural colours for displays, refractive index sensing and dynamic colour change. The strength of this approach relies in the possibility to scale it up to larger surfaces, on arbitrary substrates (e.g, semiconductor, ceramic, metal) eventually exhibiting a curvature. It can be extended to most metal oxides and other advanced functionalities are at hand.

3.5 Methods

3.5.1 Soft-NIL

Masters are fabricated via e-beam lithography and reactive ion etching on a silicon wafer. 9 arrays of squared pillars of height 500 nm, gap (distance between two structures) of 150 nm and pitch varying between 380 and 600 nm were fabricated via e-beam lithography and reactive ion etching in a silicon wafer. The master surface is rendered hydrophobic by grafting with a fluorinated precursor. To fabricate the mould, an h-PDMS blend (h-PDMS from Gelest Inc) is directly poured on the hydrophobized master and partially cured for 10 mins at 50 °C then a thick PDMS buffer layer (RTV615 from Momentive) is added and the stack annealed at 50°C for 12 hours then at 70 °C for 2 hours.

TiO₂ replicas were made using a well-established protocol [44, 49]: a TiO₂ xerogel is first deposited on glass by dip-coating in controlled environment (22 °C, relative humidity RH = 20%) using an ACE dip equipment from SolGelWay then placed in a specially designed chamber with controlled humidity (RH = 70%). After allowing the xerogel to equilibrate with the atmosphere for 1 min, the mould (first degassed under primary vacuum (<10 mbar) for 10 min) is put into contact without any additional pressure on the freshly deposited sol-gel layer. Finally, after 1 min, the assembly (mould and substrate) is annealed at 70 °C for 5 min and unmoulded. The TiO₂ replica is then annealed at 450 °C for 10 min (sample of Fig.1-4) or at 500 °C for 10 min (sample of Fig.5). In this latter case the sample was obtained from a different silicon master etched by focused ion beam in arrays of 15 x 15 μm².

Sol-gel initial solutions were prepared from TiCl₄, Pluronic F127 (Polyethylene oxide-Polypropylene oxide triblock copolymer), deionized water, absolute ethanol (EtOH). TiO₂ precursor solution is composed of 1 TiCl₄; 40 EtOH; 7 H₂O; 2.10⁻⁴ F127 molar ratios. Solutions were stirred 24 hours at room temperature prior to use.

3.5.2 Characterization

Samples were characterized by scanning electron microscopy (SEM, Dual-beam FIB HELIOS 600 nanolab), atomic force microscopy (AFM, PSIA XE-100 AFM) in non-

contact mode, ellipsometry (Woollam M2000V), optical microscopy (LEICA DMI5000 M), confocal spectroscopic microscopy (custom made) and angle resolved reflectance measured with a spectro-polarimetric goniometer (Light Tec).

Ellipsometry. The refractive index dispersion and thickness of the TiO_2 and SiO_2 sol-gel coatings were measured on flat zones of the samples, near the imprinted areas, using a spectroscopic ellipsometry system. The environmental ellipsometric porosimetry investigation was carried out using the spectroscopic ellipsometry equipment combined with an atmospheric control chamber. Water was selected as the adsorbate. The volume of adsorbed (and capillary condensed) water into the pores was followed through a time resolved measurement of the refractive index variation as a function of P/P_0 . The volume of adsorbed water was deduced from the refractive index using the Cauchy models and the Bruggeman effective medium approximation (J. A. Woollam CompleteEASE software). The pore size distribution was then extracted using a modified Kelvin's equation for spherical pores. The structural investigation of the nanoimprinted samples was performed by AFM and high-resolution SEM.

Diffusion spectroscopy. All the presented spectra were collected using a custom made, inverted optical bright- and dark-field microscope mounting 5x and 20x magnification objective lenses (numerical aperture $\text{NA} = 0.2$ and 0.4 respectively) coupled with a spectrometer and Si-based CCD linear array (Flame-T-VIS-NIR by Ocean Optics) through an optical fibre (Ocean Optics multimode fibre, VIS-NIR, core diameter 200 μm). Reflection and diffusion from the sample was studied under white light illumination (OSL2 Thorlabs or a commercial white LED).

Humidity tuning set-up. The sample was placed inside a custom made chamber surrounding the microscope objective. The relative humidity inside the chamber is driven by a flux-control set-up (ACE flow by Solgelway) and does not depend on the surrounding environment. An electronically controlled ramp sets the humidity inside the chamber while diffusion spectra from the sample are acquired. Before each set of measurement the relative humidity is set at $\text{RH}\% = 0\%$, in order to purge the chamber and the sample from the ambient humidity. Furthermore, before each humidity cycle, sample was heated for 10 min at $250\text{ }^\circ\text{C}$ in order to remove adsorbed pollutants and obtain reproducible refractive index shift with humidity variation.

References

- [1] J. S. and J. Z. “All-dielectric metamaterials”. In: *Nat. Nanotechnol.* 11 (2016), pp. 23–36.
- [2] I. Staude and J. Schilling. “Metamaterial-inspired silicon nanophotonics”. In: *Nature Photonics* 11.5 (2017), p. 274.
- [3] D. K. Gramotnev and S. I. Bozhevolnyi. “Plasmonics beyond the diffraction limit”. In: *Nature Photonics* 4 (2010), pp. 83–91.
- [4] H. A. Atwater and A. Polman. “Plasmonics for improved photovoltaic devices”. In: *Nature materials* 9.3 (2010), pp. 205–213.
- [5] N. Meinzer, W. L. Barnes, and I. R. Hooper. “Plasmonic meta-atoms and meta-surfaces”. In: *Nature Photonics* 8 (2014), pp. 889–898.
- [6] P. Spinelli, M. Verschuuren, and A. Polman. “Broadband omnidirectional antireflection coating based on subwavelength surface Mie resonators”. In: *Nature Communications* 3 (2012), p. 692.
- [7] P. Moitra, B. A. Slovick, Z. G. Yu, S. Krishnamurthy, and J. Valentine. “Experimental demonstration of a broadband all-dielectric metamaterial perfect reflector”. In: *Applied Physics Letters* 104 (2014), p. 171102.
- [8] A. Arbabi, E. Arbabi, Y. Horie, S. M. Kamali, and A. Faraon. “Planar metasurface retroreflector”. In: *Nature Photonics* 11 (2017), pp. 415–420.
- [9] M. Khorasaninejad, W. T. Chen, R. C. Devlin, J. Oh, A. Y. Zhu, and F. Capasso. “Metalenses at visible wavelengths: Diffraction-limited focusing and subwavelength resolution imaging”. In: *Science* 352.6290 (2016), pp. 1190–1194.
- [10] Y. Yang, W. Wang, P. Moitra, I. I. Kravchenko, D. P. Briggs, and J. Valentine. “Dielectric Meta-Reflectarray for Broadband Linear Polarization Conversion and Optical Vortex Generation”. In: *Nano Letters* 14 (2014), pp. 1394–1399.
- [11] D. Lin, P. Fan, E. Hasman, and M. L. Brongersma. “Dielectric gradient metasurface optical elements”. In: *science* 345.6194 (2014), pp. 298–302.

- [12] E. Arbabi, A. Arbabi, S. M. Kamali, Y. Horie, and A. Faraon. “Controlling the sign of chromatic dispersion in diffractive optics with dielectric metasurfaces”. In: *Optica* 4 (2017), p. 625.
- [13] E. Maguid, I. Yulevich, M. Yannai, V. Kleiner, M. L. Brongersma, and E. Hasman. “Multifunctional interleaved geometric-phase dielectric metasurfaces”. In: *Light Science and Applications* 6 (2017), e17027.
- [14] Y. Yang, I. I. Kravchenko, D. P. Briggs, and J. Valentine. “All-dielectric metasurface analogue of electromagnetically induced transparency”. In: *Nature Communications* 5 (2014).
- [15] A. Tittl, A. Leitis, M. Liu, F. Yesilkoy, D.-Y. Choi, D. N. Neshev, Y. S. Kivshar, and H. Altug. “Imaging-based molecular barcoding with pixelated dielectric metasurfaces”. In: *Science* 360 (2018), pp. 1105–1109.
- [16] Y. Yang, W. Wang, A. Boulesbaa, I. I. Kravchenko, D. P. Briggs, A. Puretzky, D. Geohegan, and J. Valentine. “Nonlinear Fano-Resonant Dielectric Metasurfaces”. In: *Nano Letters* 15 (2015), pp. 7388–7393.
- [17] S. Liu, M. B. Sinclair, S. Saravi, G. A. Keeler, Y. Yang, J. Reno, G. M. Peake, F. Setzpfandt, I. Staude, T. Pertsch, and I. Brener. “Resonantly Enhanced Second-Harmonic Generation Using III–V Semiconductor All-Dielectric Metasurfaces”. In: *Nano Letters* 16 (2016), pp. 5426–5432.
- [18] L. Carletti, A. Locatelli, D. Neshev, and C. D. Angelis. “Shaping the Radiation Pattern of Second-Harmonic Generation from AlGaAs Dielectric Nanoantennas”. In: *ACS Photonics* 3 (2016), pp. 1500–1507.
- [19] F. Timpu, A. Sergeyev, N. R. Hendricks, and R. Grange. “Second-Harmonic Enhancement with Mie Resonances in Perovskite Nanoparticles”. In: *ACS Photonics* 4 (2017), pp. 76–84.
- [20] R. Fenollosa, F. Meseguer, and M. Tymczenko. “Silicon Colloids: From Microcavities to Photonic Sponges”. In: *Advanced Materials* 20 (2008), pp. 95–98.
- [21] M. Garín, R. Fenollosa, R. Alcubilla, L. Shi, L. Marsal, and F. Meseguer. “All-silicon spherical-Mie-resonator photodiode with spectral response in the infrared region”. In: *Nature communications* 5 (2014), p. 3440.

-
- [22] L. Shi, T. U. Tuzer, R. Fenollosa, and F. Meseguer. “A New Dielectric Metamaterial Building Block with a Strong Magnetic Response in the Sub-1.5-Micrometer Region: Silicon Colloid Nanocavities”. In: *Advanced Materials* 24 (2012), pp. 5934–5938.
- [23] M. Abbarchi, M. Naffouti, B. Vial, A. Benkouider, L. Lermusiaux, L. Favre, A. Ronda, S. Bidault, I. Berbezier, and N. Bonod. “Wafer scale formation of monocrystalline silicon-based mie resonators via silicon-on-insulator dewetting”. In: *ACS nano* 8.11 (2014), pp. 11181–11190.
- [24] M. Naffouti, T. David, A. Benkouider, L. Favre, M. Cabie, A. Ronda, I. Berbezier, and M. Abbarchi. “Fabrication of core-shell nanostructures via silicon on insulator dewetting and germanium condensation: towards a strain tuning method for SiGe-based heterostructures in a three-dimensional geometry”. In: *Nanotechnology* 27.30 (2016), p. 305602.
- [25] M. Naffouti, T. David, A. Benkouider, L. Favre, A. Delobbe, A. Ronda, I. Berbezier, and M. Abbarchi. “Templated Solid-State Dewetting of Thin Silicon Films”. In: *Small* 12.44 (2016), pp. 6115–6123.
- [26] M. Naffouti, T. David, A. Benkouider, L. Favre, A. Ronda, I. Berbezier, S. Bidault, N. Bonod, and M. Abbarchi. “Fabrication of poly-crystalline Si-based Mie resonators via amorphous Si on SiO₂ dewetting”. In: *Nanoscale* 8.5 (2016), pp. 2844–2849.
- [27] M. Naffouti, R. Backofen, M. Salvalaglio, T. Bottein, M. Lodari, A. Voigt, T. David, A. Benkouider, I. Fraj, L. Favre, et al. “Complex dewetting scenarios of ultrathin silicon films for large-scale nanoarchitectures”. In: *Science advances* 3.11 (2017), eaao1472.
- [28] T. Wood, M. Naffouti, J. Berthelot, T. David, J.-B. Claude, L. Métayer, A. Delobbe, L. Favre, A. Ronda, I. Berbezier, et al. “All-dielectric color filters using SiGe-based Mie resonator arrays”. In: *ACS photonics* 4.4 (2017), pp. 873–883.
- [29] M. Bouabdellaoui, S. Checcucci, T. Wood, M. Naffouti, R. P. Sena, K. Liu, C. M. Ruiz, D. Duche, J. le Rouzo, L. Escoubas, G. Berginc, N. Bonod, M. Zazoui, L. Favre, L. Metayer, A. Ronda, I. Berbezier, D. Grosso, M. Gurioli, and

- M. Abbarchi. “Self-assembled antireflection coatings for light trapping based on SiGe random metasurfaces”. In: *Physical Review Materials* 2 (2018).
- [30] S. Checcucci, T. Bottein, J.-B. Claude, T. Wood, M. Putero, L. Favre, M. Gurioli, M. Abbarchi, and D. Grosso. “Titania-Based Spherical Mie Resonators Elaborated by High-Throughput Aerosol Spray: Single Object Investigation”. In: *Advanced Functional Materials* 28 (2018), p. 1801958.
- [31] R. C. Devlin, M. Khorasaninejad, W. T. Chen, J. Oh, and F. Capasso. “Broadband high-efficiency dielectric metasurfaces for the visible spectrum”. In: *Proceedings of the National Academy of Sciences* 113.38 (2016), pp. 10473–10478.
- [32] W. Yue, S. Gao, S.-S. Lee, E.-S. Kim, and D.-Y. Choi. “Highly reflective subtractive color filters capitalizing on a silicon metasurface integrated with nanostructured aluminum mirrors”. In: *Laser & Photonics Reviews* 11.3 (2017).
- [33] V. Vashistha, G. Vaidya, P. Gruszecki, A. E. Serebryannikov, and M. Krawczyk. “Polarization tunable all-dielectric color filters based on cross-shaped Si nanoantennas”. In: *Scientific Reports* 7.1 (2017), p. 8092.
- [34] S. Sun, Z. Zhou, C. Zhang, Y. Gao, Z. Duan, S. Xiao, and Q. Song. “All-dielectric full-color printing with TiO₂ metasurfaces”. In: *ACS nano* 11.5 (2017), pp. 4445–4452.
- [35] C.-S. Park, V. R. Shrestha, W. Yue, S. Gao, S.-S. Lee, E.-S. Kim, and D.-Y. Choi. “Structural color filters enabled by a dielectric metasurface incorporating hydrogenated amorphous silicon nanodisks”. In: *Scientific Reports* 7.1 (2017), p. 2556.
- [36] X. Zhu, W. Yan, U. Levy, N. A. Mortensen, and A. Kristensen. “Resonant laser printing of structural colors on high-index dielectric metasurfaces”. In: *Science Advances* 3.5 (2017), e1602487.
- [37] V. Neder, S. L. Luxembourg, and A. Polman. “Efficient colored silicon solar modules using integrated resonant dielectric nanoscatterers”. In: *Applied Physics Letters* 111.7 (2017), p. 073902.

-
- [38] V. Flauraud, M. Reyes, R. Paniagua-Dominguez, A. I. Kuznetsov, and J. Brugger. “Silicon nanostructures for bright field full color prints”. In: *ACS Photonics* 4.8 (2017), pp. 1913–1919.
- [39] Y. Horie, S. Han, J.-Y. Lee, J. Kim, Y. Kim, A. Arbabi, C. Shin, L. Shi, E. Arbabi, S. M. Kamali, H.-S. Lee, S. Hwang, and A. Faraon. “Visible Wavelength Color Filters Using Dielectric Subwavelength Gratings for Backside-Illuminated CMOS Image Sensor Technologies”. In: *Nano Letters* 17 (2017), pp. 3159–3164.
- [40] Y. Nagasaki, I. Hotta, M. Suzuki, and J. Takahara. “Metal-Masked Mie-Resonant Full-Color Printing for Achieving Free-Space Resolution Limit”. In: *ACS Photonics* 5 (2018), pp. 3849–3855.
- [41] A. Abarca, P. Gómez-Sal, A. Martín, M. Mena, J. M. Poblet, and C. Yélamos. “Tunable Dielectric Resonator Metasurfaces at Visible Frequencies”. In: *ACS Nano* 10 (2016), pp. 133–141.
- [42] S. Sun, W. Yang, C. Zhang, J. Jing, Y. Gao, X. Yu, Q. Song, and S. Xiao. “Real-Time Tunable Colors from Microfluidic Reconfigurable All-Dielectric Metasurfaces”. In: *ACS Nano* 12 (2018), pp. 2151–2159.
- [43] T. Bottein, T. Wood, T. David, J. Claude, L. Favre, I. Berbezier, A. Ronda, M. Abbarchi, and D. Grosso. ““Black” Titania coatings composed of sol-gel imprinted Mie resonators arrays”. In: *Adv. Funct. Mater.* (2016).
- [44] T. Bottein, O. Dalstein, M. Putero, A. Cattoni, M. Faustini, M. Abbarchi, and D. Grosso. “Environment-controlled sol-gel soft-NIL processing for optimized titania, alumina, silica and yttria-zirconia imprinting at sub-micron dimensions”. In: *Nanoscale* (2018).
- [45] S. Kim. “Simultaneous determination of refractive index, extinction coefficient, and void distribution of titanium dioxide thin film by optical methods”. In: *Applied optics* 35.34 (1996), pp. 6703–6707.
- [46] T. Siefke, S. Kroker, K. Pfeiffer, O. Puffky, K. Dietrich, D. Franta, I. Ohlídal, A. Szeghalmi, E.-B. Kley, and A. Tünnermann. “Materials pushing the application limits of wire grid polarizers further into the deep ultraviolet spectral range”. In: *Advanced Optical Materials* 4.11 (2016), pp. 1780–1786.

- [47] H. A. Atwater, A. R. Davoyan, O. Ilic, D. Jariwala, M. C. Sherrott, C. M. Went, W. S. Whitney, and J. Wong. “Materials challenges for the Starshot lightsail”. In: *Nature Materials* 17 (2018), pp. 861–867.
- [48] T. Coenen, J. V. D. Groep, and A. Polman. “Resonant Modes of Single Silicon Nanocavities Excited by Electron Irradiation”. In: *ACS nano* 7 (2013), pp. 1689–1698.
- [49] T. Bottein, T. Wood, T. David, J. B. Claude, L. Favre, I. Berb ezier, A. Ronda, M. Abbarchi, and D. Grosso. ““Black” Titania Coatings Composed of Sol–Gel Imprinted Mie Resonators Arrays”. In: *Advanced Functional Materials* 27.2 (2017).
- [50] J. Sautter, I. Staude, M. Decker, E. Rusak, D. N. Neshev, I. Brener, and Y. S. Kivshar. “Active Tuning of All-Dielectric Metasurfaces”. In: *ACS Nano* 9.4 (Mar. 2015), pp. 4308–4315.
- [51] N. Caselli, F. Intonti, F. L. China, F. Biccari, F. Riboli, A. Gerardino, L. Li, E. H. Linfield, F. Pagliano, A. Fiore, and M. Gurioli. “Generalized Fano lineshapes reveal exceptional points in photonic molecules”. In: *Nature Communications* 9 (2018).
- [52] B. Luk anchuk, N. I. Zheludev, S. A. Maier, N. J. Halas, P. Nordlander, H. Giessen, and C. T. Chong. “The Fano resonance in plasmonic nanostructures and metamaterials”. In: *Nature Materials* 9 (2010), pp. 707–715.
- [53] M. F. Limonov, M. V. Rybin, A. N. Poddubny, and Y. S. Kivshar. “Fano resonances in photonics”. In: *Nature Photonics* 11.9 (2017), pp. 543–554.
- [54] D. R. Ceratti, M. Faustini, C. Sinturel, M. Vayer, V. Dairel, M. Jardat, and D. Grosso. “Critical effect of pore characteristics on capillary infiltration in mesoporous films”. In: *Nanoscale* 7 (2015), pp. 5371–5382.
- [55] Y. H. D. Lee and M. Lipson. “Back-end deposited silicon photonics for monolithic integration on CMOS”. In: *IEEE Journal of Selected Topics in Quantum Electronics* 19.2 (2013), p. 8200207.
- [56] D. Grosso, C. Boiss ere, and C. Sanchez. “Ultralow-dielectric-constant optical thin films built from magnesium oxyfluoride vesicle-like hollow nanoparticles”. In: *Nature Materials* 6 (2007), pp. 572–575.

-
- [57] J. Van de Groep and A. Polman. “Designing dielectric resonators on substrates: Combining magnetic and electric resonances”. In: *Optics express* 21.22 (2013), pp. 26285–26302.
- [58] P. Offermans, M. C. Schaafsma, S. R. K. Rodriguez, Y. Zhang, M. Crego-Calama, S. H. Brongersma, and J. G. Rivas. “Universal Scaling of the Figure of Merit of Plasmonic Sensors”. In: *ACS Nano* 5 (2011), pp. 5151–5157.
- [59] V. G. Kravets, A. V. Kabashin, W. L. Barnes, and A. N. Grigorenko. “Plasmonic Surface Lattice Resonances: A Review of Properties and Applications”. In: *Chemical reviews* 118 (2018), pp. 5912–5951.
- [60] A. Komar, Z. Fang, J. Bohn, J. Sautter, M. Decker, A. Miroshnichenko, T. Pertsch, I. Brener, Y. S. Kivshar, I. Staude, and D. N. Neshev. “Electrically tunable all-dielectric optical metasurfaces based on liquid crystals”. In: *Applied Physics Letters* 110 (2017), p. 071109.
- [61] P. Gutruf, C. Zou, W. Withayachumnankul, M. Bhaskaran, S. Sriram, and C. Fumeaux. “Mechanically Tunable Dielectric Resonator Metasurfaces at Visible Frequencies”. In: *ACS Nano* 10.1 (Dec. 2015), pp. 133–141.

Chapter 4

SiGe-based Mie resonators as antireflection elements

Here is demonstrated another possible bottom-up approach for the fabrication of dielectric Mie resonators over large scales: solid state dewetting of thin silicon films. This method is a distinct self-assembly technique which, as for the other techniques introduced in the previous chapters, provide a very high throughput. Here it is shown that efficient antireflection coatings on silicon can be easily obtained when solid state dewetting of silicon is joined with germanium deposition for the fabrication of SiGe islands with a high surface density, randomly positioned and broadly varied in size. This particular feature is demonstrated to be efficient for light trapping. A large portion of the impinging light ($\sim 40\%$) is trapped within the wafer also below the band gap, where the Si substrate is non absorbing. Reflectance is then reduced to low values in a broad spectral range (from 500 nm to 2500 nm) and a broad angle (up to 55°). Theoretical simulations agree with the experimental results, showing that the efficient light coupling into the substrate is mediated by Mie resonances formed within the SiGe islands. This lithography-free method can be implemented on arbitrarily thick or thin SiO_2 layers and its duration only depends on the sample thickness and on the annealing temperature.

4.1 Introduction

Efficient anti-reflection coatings (ARC) have been intensively studied and many different approaches were explored for this purpose [1–3]. Multi-layered thin-films [4, 5], graded index matching via surface texturing with micro- and nano-structures [6–11], plasmonic metasurfaces [12–14] are just few examples. More recently, metasurfaces [15–21] based on ordered arrays of sub-micrometric dielectric antennas (dielectric Mie resonators [22–28]) are also taking ground to this purpose. Depending on the application of the AR different aspects (lowest value of the total reflectance, broad spectral range, broad acceptance angle, transparency or light trapping) determine the optimal features and fabrication method.

A convenient and efficient solution for enhancing light absorption relies on the exploitation of disordered structures[13, 29–33]. The peculiar AR properties of disordered systems account for the importance of this approach with respect to its ordered counterparts and this alternative has been recently proposed [20] and implemented [19] using dielectric Mie resonators. The performances obtained with such random all-dielectric structures demonstrate that *top-down* methods are a valuable technique to combine disorder and Mie resonators for efficient AR coatings at visible frequencies. However, the ease of fabrication at affordable prices on reasonable timescales, are major requirements for realistic devices implemented on large scales and conventional *top-down* methods are unable to meet such criteria.

Random metasurfaces offer the basis for the development of less costly and large-scale bottom-up fabrication methods based on self-assembly. One viable and promising route is solid-state dewetting of ultra-thin films of metals [18, 34–41] and semiconductors [42–45], a natural phenomenon exploited for the self-assembly of high-quality photonic structures. Arrays of well separated islands, featuring a random spatial organization and a relatively large spread of sizes and shapes can be produced. The potential of this method in semiconductors has not been completely exploited and, for example, AR formed by self-assembly have not yet been reported. In fact, one of the main limits of this method is the relatively low density of the dewetted particles: in solid state dewetting, as in other self-assembly methods for 3D nanostructures (e.g. Stranski Krastanov growth in IV-IV and III-V compounds) a linear dependence links

the initial thickness of the Si(Ge) layer and the final size (and density) of the dewetted islands [46]. This feature naturally leads to large inter-particle distances and limits the exploitation of dewetting for nanophotonics.

In this chapter, is reported the implementation of a self-assembly method based on dewetting and epitaxial growth for the fabrication of AR coatings. Here we manage to overcome the well-known limitations of most common self-assembly processes: the correlation between size and density of the islands. Furthermore, in contrast with previous reports of SiGe dewetting where marked spatial anisotropies affected the size distribution of the islands [43, 47, 48], in our samples large and small particles are perfectly mixed, providing a homogeneous arrangement of randomly positioned islands.

Such a structure already exhibits broad-band and broad angle AR properties with respect to bare silicon wafer. Moreover, the resonant behaviour of the SiGe islands was studied thanks to finite difference time domain simulations (FDTD), highlighting that Mie resonances enhance the coupling and light trapping of the impinging light towards the underlying Si wafer. This feature, not accessible by thin film based AR, can represent a useful trait for photovoltaic and detector applications.

To improve the AR properties of the bare SiGe metasurfaces, we include a double layer of Si_3N_4 and SiO_2 on top of the islands and on the backside of the samples, taking inspiration to similar approaches in literature [15], where *ad hoc* Si_3N_4 conformal layers were used. Thus, we target specific wavelength ranges optimizing the AR for below band-gap frequencies, where the total reflectance (R_{tot}) reaches 7-20%, and for above band-gap frequencies, where R_{tot} is reduced to few percentages. Angle-resolved measurements confirm that these properties are maintained within an acceptance angle of about ± 55 degrees.

4.2 Solid state dewetting for SiGe-based Mie resonators

Intrinsic features of solid state dewetting of silicon films are set by the initial thickness of the thin, crystalline layer determining the period of the underlying Rayleigh-like instability, and setting all the built-in structural parameters of the islands, such as

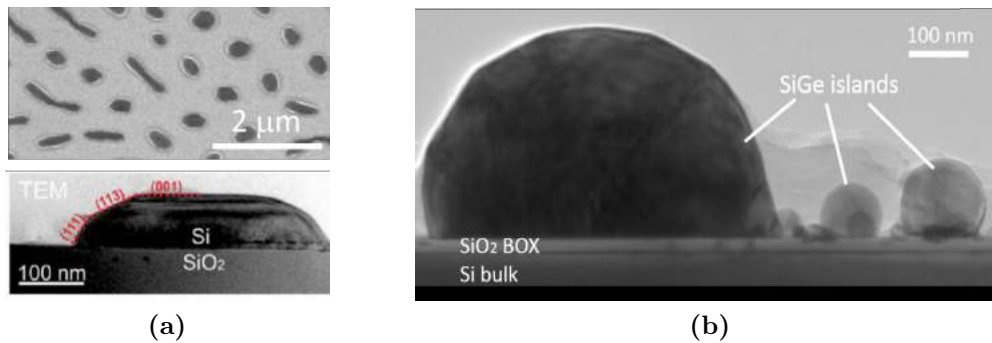


Figure 4.1: *a) SEM (top) and TEM (bottom) images of a dewetted sample of Silicon islands. b) TEM image of a large island and a few smaller Germanium islands.*

their density, size, and equilibrium shape [49–53]. All these properties can be modified by adding Ge before, during, or after dewetting [43, 44, 47, 48, 53–55], potentially providing full control over their physical properties. However, in precedent works exploiting dewetting in SiGe-based samples [47, 48, 53], Si-rich and Ge-rich particles rest spatially separated, leading to large inhomogeneities of the morphological properties over micrometric distances that make this method unsuitable for performing devices.

Another important condition for the formation of intense and sharp resonances in dielectric Mie resonators, is a relatively large vertical aspect ratio ($\eta = h/r$, where h is the particle’s height and $r = d/2$ is the half of its base size) [56]. While η remains low in pure Si islands, it is higher in SiGe [44, 48].

Here we modify solid state dewetting of ultrathin silicon on insulator (UT-SOI), by adding a large amount of Ge (300 monolayers MNLs at 800°) during the annealing step (an accurate description of the fabrication process is reported in section 4.6.1).

As result of this growing technique, SiGe islands exhibit a vertical aspect ratio remarkably bigger than pure Silicon islands, as is shown in fig. 4.1, where a TEM image of pure Si island (bottom inset of fig. 4.1a) is compared to a TEM image of SiGe islands (fig. 4.1b). Moreover, we highlight (i) a random formation of the islands and a complete lack of spatial organization (as accounted for by the Fourier transform of a SEM image of sample II in the inset of the top panel of fig. 4.2b); (ii) a homogeneous distribution of large and small islands perfectly mixed together eventually showing a bimodal size distribution (figs. 4.2a to 4.2c); (iii) a lack of elongation of the islands along preferential crystallographic directions or a more pronounced symmetry for a

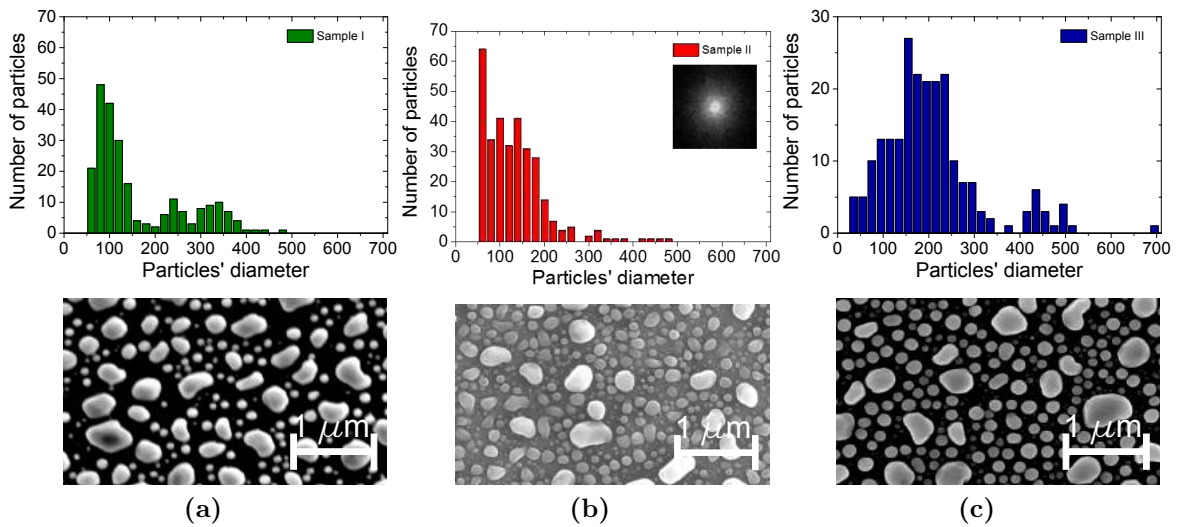


Figure 4.2: Statistical distribution of particle size and high-resolution SEM images of the dewetted samples for sample I **a)**, II **b)** and III **c)**. For sample II inset shows also the two-dimensional Fourier transform of a $9 \times 9 \mu\text{m}^2$ SEM image.

family of islands [43, 47, 48]; this has to be compared with the corresponding situation for bare Si islands, exhibiting a preferential distribution and a pronounced elongation (bottom inset of fig. 4.1). (iv) The presence of dislocations in both families of particles (fig. 4.1b). All these features are unique of this fabrication procedure and very similar results were obtained with samples grown in slightly different experimental conditions (e.g., at $780 \text{ }^\circ\text{C}$) accounting for the robustness of the approach (not shown).

From this picture it emerges that solid state dewetting of SiGe has a great potential for nanophotonics on large scales.

After dewetting and Ge supply, we deposited conformal layers of SiO_2 and Si_3N_4 on top of the islands as well as on the back face of the samples via plasma enhanced chemical vapor deposition. This step allows the optimization of their antireflection properties as detailed later. The list of the samples and their features are summarized in figs. 4.2a to 4.2c. In section (d) of table 4.1 is reported a sketch of the SiGe metasurface with the conformal layers realized on the top and on the bottom.

Further details of morphological characterization of the realized samples is given in section 4.6.2.

4. SiGe-based Mie resonators as antireflection elements


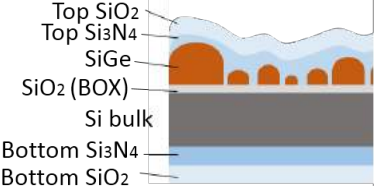

	Sample I-A	Sample I-B	Sample I-C		Sample III-A	Sample III-B	Sample III-C	
T	130 nm Si ₃ N ₄	100 nm Si ₃ N ₄	70 nm Si ₃ N ₄		T	130 nm SiO ₂	100 nm SiO ₂	70 nm SiO ₂
B	100 nm Si ₃ N ₄	100 nm Si ₃ N ₄	100 nm Si ₃ N ₄		B	100 nm SiO ₂ 100 Si ₃ N ₄	100 nm SiO ₂ 100 nm Si ₃ N ₄	100 nm SiO ₂ 100 nm Si ₃ N ₄
(a)				(b)				
	Sample II-A	Sample II-B	Sample II-C					
T	120 nm SiO ₂ 120 Si ₃ N ₄	100 nm SiO ₂ 100 nm Si ₃ N ₄	80 nm SiO ₂ 80 nm Si ₃ N ₄					
B	100 nm SiO ₂ 100 Si ₃ N ₄	100 nm SiO ₂ 100 nm Si ₃ N ₄	100 nm SiO ₂ 100 nm Si ₃ N ₄		(c)			
(c)				(d)				

Table 4.1: *a-c)* List of samples with corresponding thicknesses of the SiO₂ and Si₃N₄ layers deposited on top of the SiGe islands (T) and on the backside (B). All the reported thicknesses are expressed in nm. *d)* Sketch of the SiGe island with conformal layers on the top and on the bottom (not on scale).

4.3 Optical characterization and simulations

A description of the instruments and methods used for spectroscopy is reported in the devoted section 4.6.3. The total reflectance R_{tot} of a Si wafer is determined by the refractive index contrast with air, and by its thickness: for frequencies below the Si band gap, the transparency of the material calls into play the reflection from the backside of the wafer. This determines a sharp increase of R_{tot} at about 1050 nm (fig. 4.3a). This increased value of R_{tot} can be quantified in about 15%–20% by simulating the reflection from the top face and from both top and bottom faces of a thick Si slab (respectively thick, purple line and thin, green line in fig. 4.3a).

The total reflectance R_{tot} for a dewetted 12 nm thick UT-SOI is compared to that of a Si wafer in fig. 4.3b, empty squares line. The small effect of the dewetted sample on the impinging light implies that, per se, dewetting is not suitable for efficient AR. Samples I, II, and III with SiGe island, however, show a pronounced AR effect with respect to the bare Si wafer (fig. 4.3b, green, red and blue lines). At frequencies larger than the Si band gap the value of R_{tot} is about 4%–12%, whereas at larger wavelengths, this value rises to about 25%–30% due to the transparency of the substrate and the backface reflection. We can observe that samples I and III feature a more pronounced

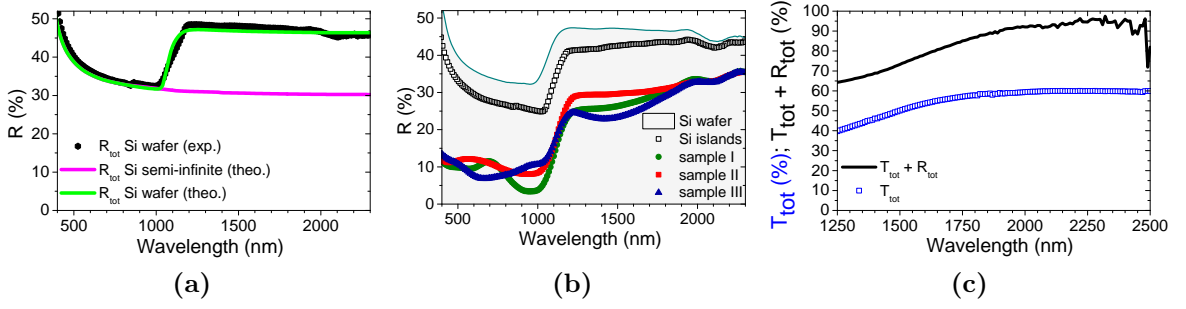


Figure 4.3: Total reflectance R_{tot} for Si- and SiGe-based metasurfaces. **a)** R_{tot} in the full investigated spectral range for a Si wafer. Experimental data, black circles; theoretical simulation for the top face only, thick purple line; theoretical simulation for the both top and bottom faces, thin, orange line. The shaded area highlights the transition from above- to below band-gap frequencies. **b)** Experimental data for R_{tot} measured on: Si wafer (gray line and shaded area), bare Si islands (empty black squares) and bare SiGe islands sample I, II and III (respectively green circles, red squares and blue triangles). **c)** Total transmission T_{tot} (blue squares) and total transmission plus total reflection $T_{tot} + R_{tot}$ (black line) for samples III. The error in the measured light intensity is less than 2% in at longer wavelengths where the white lamp used for illumination is less intense.

fluctuation of R_{tot} with respect to II, which springs from their particles' larger average size and the more pronounced bimodal size distribution (fig. 4.2, bottom panels).

While the minimum of R_{tot} for bare SiGe islands is not very low, the most remarkable feature of the AR effect of our metasurface is its extension to all the investigated frequencies with a very smooth spectral dependence. In fact, even if conventional ARs based on thin film coatings can provide lower values of R_{tot} at specific wavelengths, they fail in matching the performances of our AR when considering the full spectrum from visible to near infrared. These features are systematically investigated in figs. 4.4a to 4.4c, where the spectra of simulated interferential ARs based on a SiO_2 single layer, a Si_3N_4 single layer, and a SiO_2 on Si_3N_4 double layer are compared with the spectra of samples I, II, and III. While the average value of R_{tot} for the best interferential layer is above 26%, the SiGe-based metasurfaces are always below 25% (fig. 4.4g). A summary of this investigation is provided in Table II.

Another relevant parameter necessary for defining the range of uses of a device is its total transmission T_{tot} . Bare SiGe islands exhibit values of T_{tot} between about 35% and 60% in the range 1200 to 2500 nm (fig. 4.3c). By adding to T_{tot} the corresponding value of R_{tot} , we can see that a significant portion of light is neither transmitted nor

4. SiGe-based Mie resonators as antireflection elements

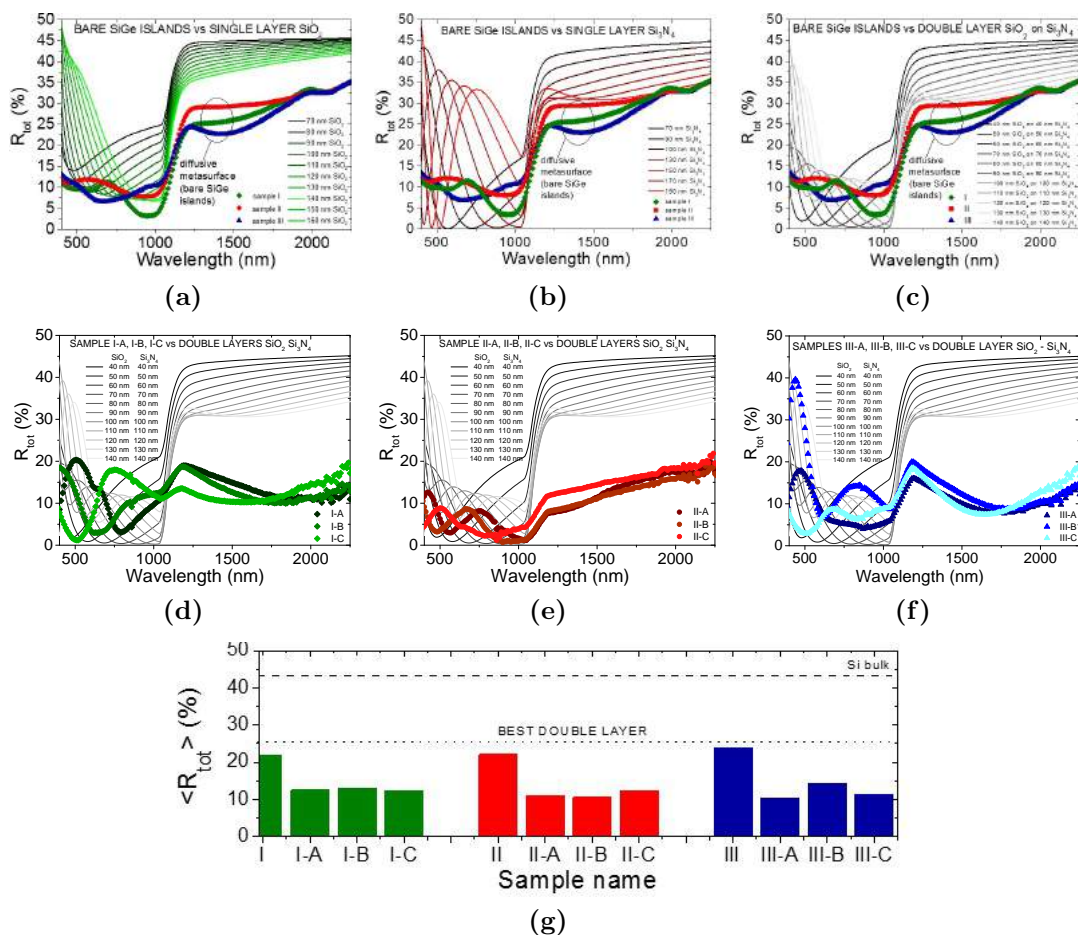


Figure 4.4: Total reflectance R_{tot} for SiGe-based metasurfaces and flat anti-reflection coating made of SiO_2 and Si_3N_4 . **a)** R_{tot} for bare SiGe islands in the full investigated spectral range (from visible to near-infrared frequencies): samples I (green diamond), II (red circles) and III (blue triangles). These experimental spectra are compared with those obtained from theoretical simulations (transfer matrix method) for SiO_2 layers on Silicon bulk. The SiO_2 thickness is varied from 70 to 170 nm. The effect of transparency of Si at frequencies smaller than the band gap is taken into account. **b)** Same as **a)** for a single layer of Si_3N_4 on Silicon bulk. The thickness of the Si_3N_4 is changed from 70 nm to 190 nm. **c)** Same as **a)** and **b)** for a double layer of SiO_2 on Si_3N_4 on Silicon bulk. The thickness of the two layers is changed from 40 nm SiO_2 on 40 nm Si_3N_4 up to 140 nm SiO_2 on 140 nm Si_3N_4 . **d)** R_{tot} for SiGe islands covered with conformal layers and interferential AR on the bottom face of the sample, in the full investigated spectral range (from visible to near-infrared frequencies): samples I-A, I-B and I-C from dark to light green respectively. These spectra of R_{tot} are compared to those obtained for a double layer of SiO_2 and Si_3N_4 on Silicon bulk (same as those shown in **c)**). **e)** Same as in **d)** for samples II-A, II-B and II-C from dark to light red respectively. **f)** Same as in **d)** for samples III-A, III-B and III-C from dark to light blue respectively. **g)** Average value of the total reflectance $\langle R_{tot} \rangle$ integrated over the full investigated range of frequencies for the 3 samples series with SiGe islands. The top horizontal dashed line sets the value of $\langle R_{tot} \rangle$ for Silicon bulk. The bottom horizontal dashed line sets the value of $\langle R_{tot} \rangle$ for the most performing AR based on SiO_2 and Si_3N_4 double layer on Silicon.

4.3 Optical characterization and simulations

$\langle R_{tot} \rangle$			$\langle R_{tot} \rangle$			$\langle R_{tot} \rangle$		
	Above BG	Full range		Above BG	Full range		Above BG	Full range
I	22.0	21.9	II	25.0	22.0	III	21.8	23.9
I-A	10.5	12.4	II-A	12.7	11.0	III-A	8.1	10.3
I-B	10.2	13.1	II-B	4.9	10.5	III-B	16.7	14.3
I-C	11.4	12.2	II-C	14.1	12.3	III-C	7.7	11.4

(a) (b) (c)

	$\langle T_{tot} \rangle$	$\langle A_{tot} \rangle$		$\langle T_{tot} \rangle$	$\langle A_{tot} \rangle$		$\langle T_{tot} \rangle$	$\langle A_{tot} \rangle$
I	56.3	13.9	II	53.5	16.4	III	54.7	16.3
I-A	77.7	9.1	II-A	71.9	13.3	III-A	80.4	8.2
I-B	77.7	9.3	II-B	75.0	10.7	III-B	79.0	8.2
I-C	77.7	8.2	II-C	71.0	12.0	III-C	79.3	7.4

(d) (e) (f)

Table 4.2: *a,b,c*) Values of $\langle R_{tot} \rangle$ for above band-gap (BG) frequencies (300-1050 nm) and for the full investigated range (300-2500 nm), for all the investigated samples. *d,e,f*) $\langle T_{tot} \rangle$ and $\langle A_{tot} \rangle = \langle 1 - T_{tot} - R_{tot} \rangle$ (absorbed light) for below band-gap frequencies (1200-2500 nm), are reported for all the investigated SiGe-based samples.

reflected ($T_{tot} + R_{tot} < 100\%$, (fig. 4.3c): about 40% of the total intensity at 1200 nm is retained within the wafer (see also the data summarized in Table II). We interpret it as a light-trapping phenomenon already reported in similar systems based on dielectric Mie resonators [21]: the presence of 3D resonant scatterers on the sample surface imposes strong modifications to the propagation of the impinging light beam, leading to its partial trapping within the wafer. This feature represents a very important characteristic of our AR and differentiates them from conventional flat AR where, at these frequencies, $T_{tot} + R_{tot} = 100\%$ (not shown) and no light trapping is possible irrespective of the performance in terms of AR (see also table 4.2 for details relative to the amount of trapped light). Importantly, the possibility to enhance the light absorption could be a valuable tool for extending the quantum efficiency of Si-based light detectors (such as CCD cameras) in this frequency range.

FDTD simulations were used to model the experimental findings (see the dedicated section 4.6.4 for details). They were first used to address the scattering intensity of individual small and large islands (respectively diameter $d = 150$ nm and $d = 450$ nm). The scattering intensity of small islands features a sharp peak at ~ 650 nm (resonance α of fig. 4.5 with relative near field distribution in fig. 4.5a). The electric and magnetic field intensity maps at 650 nm, respectively, show that $|E|$ is rather confined below the island within the buried oxide (BOX), whereas $|H|$ is well channeled into the substrate

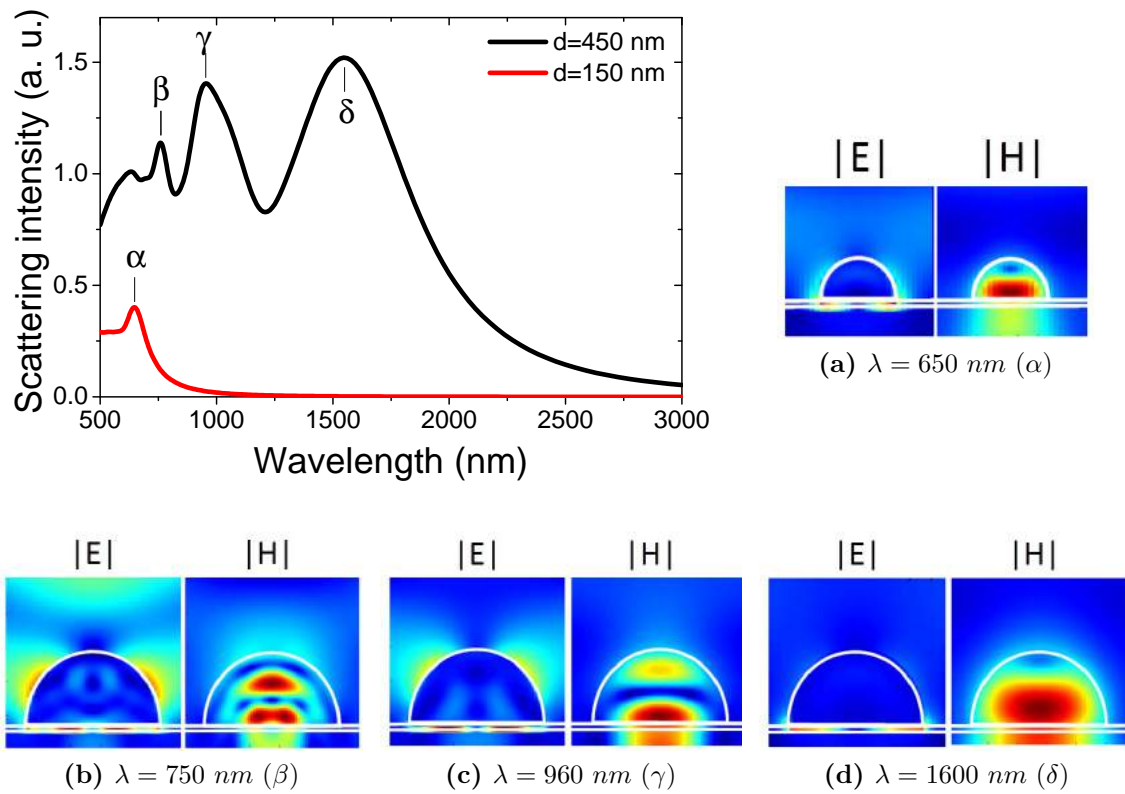


Figure 4.5: FDTD simulations. Scattering intensity of an individual island having base size of 150 nm (red line) and 450 nm (black line), with vertical aspect ratio 1/2. **a)** Near-field maps of the intensity of the electric field ($|E|$) and magnetic field ($|H|$) at 650 nm for the small particle simulated in the plot (red line). The white lines highlight the shape of the island and the BOX. **b)** Near-field maps of the intensity of the electric field and magnetic field at 750 nm for the large particle simulated in the plot (red line). **c)** Near-field maps of the intensity of the electric field and magnetic field at 960 nm for the large particle simulated in the plot (red line). **d)** Near-field maps of the intensity of the electric field and magnetic field at 1600 nm for the large particle simulated in the plot (red line). [**a)** is not in scale with **b)** to **d).**]

(fig. 4.5b). These features are quite similar to what was shown for SiGe islands [44]. However, in the present study the very thin BOX favors a more efficient light coupling within the Si wafer [15, 56]. The scattering intensity of large islands exhibits three main peaks in the investigated spectral range (resonances β , γ and δ of fig. 4.5; near field distributions in figs. 4.5b to 4.5d). As for the previous case of small islands, the field intensity maps at ~ 750 nm, ~ 960 nm, and ~ 1600 nm show that $|E|$ is rather confined within the BOX, whereas $|H|$ is well coupled into the substrate. These simulations show that SiGe-based Mie resonators are able to channel light from the ambient in the substrate thanks to the presence of resonantly confined fields extending in the underlying Si wafer. The low Q-factor, characteristic signature of Mie resonances,

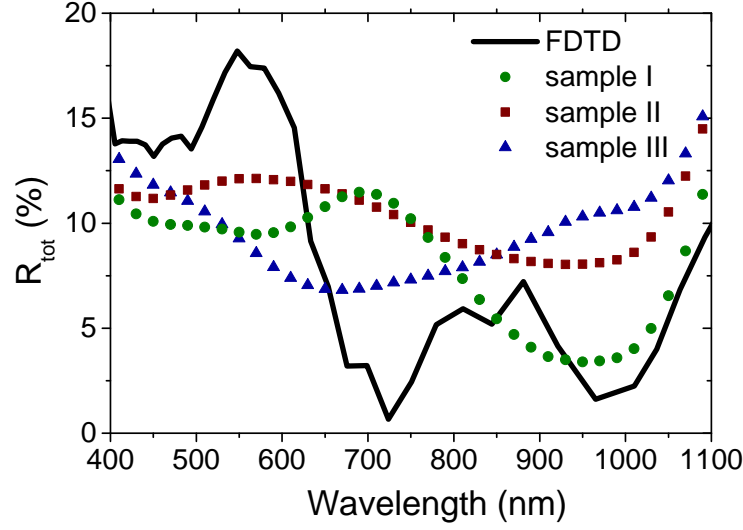


Figure 4.6: Comparison between the measured R_{tot} for samples I, II and III and the FDTD simulation taking into account a random distribution of small (150 nm in diameter) and large (450 nm in diameter) SiGe islands.

ensures a brief permanence of the light inside the islands, before it is transferred to the Si substrate, limiting possible losses due to the absorbance of germanium. Furthermore, the spread in size and the large density of the particles allows for a broad and smooth light coupling.

Simulations of R_{tot} on randomly distributed resonators of two size family show rather strong fluctuations between $\sim 18\%$ and 1% in a spectral interval spanning from ~ 400 nm to 1100 nm (black line in fig. 4.5); for R_{tot} we limit our investigation to above band-gap frequencies as the FDTD method does not allow one to easily take into account the effect of the backside of the sample. Despite the rough approximations used for describing the particles' size distribution in FDTD simulations, the overall agreement with experiments is fairly good (fig. 4.6). Clearly, the presence of many differently sized particles in experiments smooths the features of R_{tot} , but its average value in simulations and experiments are quite similar.

A complete and precise assessment of the AR properties should go beyond the values of R_{tot} and T_{tot} and include also the angular dependence of the reflected intensity and polarization properties, as well as a precise discrimination between light diffusion and specular reflectance. Improved performances with respect to the bare SiGe islands are obtained for all the samples when covered with conformal single or double layers made of Si_3N_4 and SiO_2 [15] (tables 4.1 and 4.2). Samples I-A, I-B, and I-C and III-A, III-B,

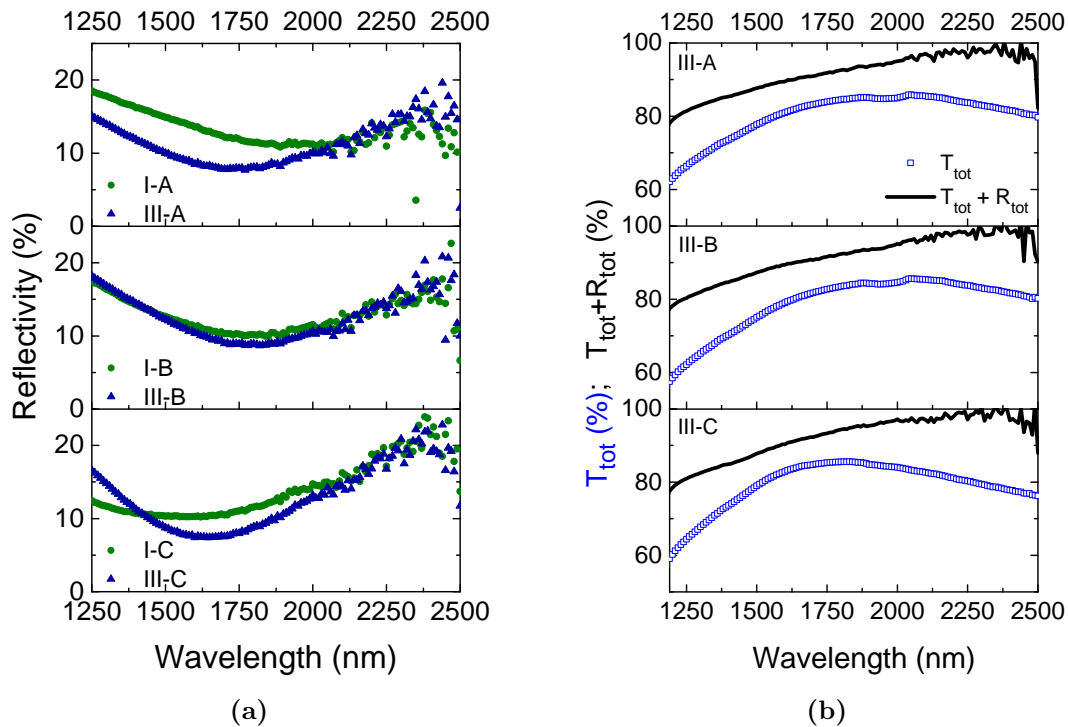


Figure 4.7: Below band-gap anti-reflection coating: samples I-A, -B, -C and III-A, -B and -C **a)** From the top to the bottom panel: total reflectance R_{tot} at quasi-normal incidence for samples I-A and III-A, I-B and III-B, and I-C and III-C. **b)** From the top to the bottom panel: total transmission T_{tot} (blue squares) and $T_{\text{tot}} + R_{\text{tot}}$ (black line) at quasi-normal incidence for samples III-A, III-B and III-C. The error in the measured light intensity is less than 2% in at longer wavelengths where the white lamp used for illumination is less intense.

and III-C were optimized for below band-gap frequencies: the total reflectance remains between 7% and 20% (fig. 4.7a), whereas it varied between 25% and 35% for the bare samples (fig. 4.3b). The different thicknesses of the conformal Si_3N_4 coatings allows for a slight tuning of the minimum of R_{tot} (e.g., from ~ 1500 nm for sample I-C up to ~ 2000 nm for sample I-A). For sample III a more pronounced dip in R_{tot} is observed in a narrower spectral range (up to 7%) owing to the presence of larger particles on sample III with respect to sample I (fig. 4.2).

Remarkably, when taking into account the full investigated spectral range spanning from visible to near-infrared frequencies, these metasurfaces outperform conventional flat ARs (see fig. 4.4g). While the best double layer coating features an average R_{tot} of about 26%, our samples are in the 8%–13% range. A summary of this investigation is shown in fig. 4.4g.

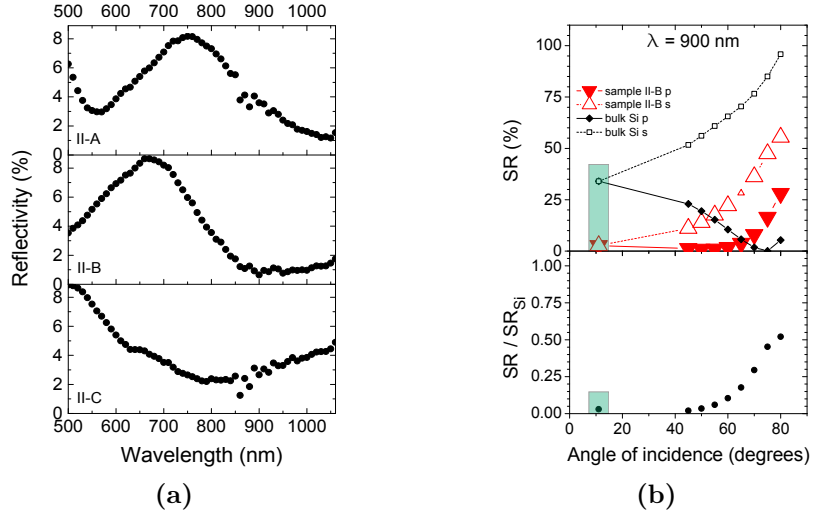


Figure 4.8: Above band-gap anti-reflection coating: sample II-A, -B and -C. **a)** From the top to the bottom panel: total reflectance R_{tot} at quasi-normal incidence for samples II-A, II-B and II-C. **b)** Top panel: specular reflectance SR for s- (open symbols) and p-polarized (full symbols) incident beam for sample II-B (triangles) and Si wafer (squares). SR for a beam incident on the sample surface at angles larger than 45 degrees is measured with an ellipsometer. SR at 11 degrees (shaded) is obtained from R_{tot} in graph a) and it thus also contains the reflected scattering ($R_{tot} = SR + RD$, see also fig. 4.10). Thus it represents an overestimation of SR. Bottom panel: Specular reflectance SR at 900 nm for sample II-B as a function of the incidence angle normalized to SR of Si wafer at the same wavelength. The error in the measured light intensity is less than 1%.

Finally, as for the bare SiGe islands case, we estimate the light trapping for samples III-A, III-B, and III-C fig. 4.7b. For these samples, covered with a conformal layer and with additional AR on the backside, T_{tot} is in the range of 60%–80% and it is enhanced with respect to the bare SiGe islands fig. 4.3c. $T_{tot} + R_{tot}$ increases monotonically providing a light trapping of about 20% at 1200 nm up to negligible values at 2500 nm table 4.2. Thus, in spite of a better performance in terms of R_{tot} owing to the layers on the backside of the wafer, at these frequencies, the light trapping is about two times less effective for capped islands with respect to the bare case (see fig. 4.3c, to be compared with fig. 4.7b). This is an important observation in view of the exploitation of these structures for specific applications where light trapping should be enhanced with respect to transparency.

Samples II-A, II-B, and II-C were optimized as AR for frequencies above the Si band gap (table 4.1 and fig. 4.8). For all these samples, R_{tot} can reach values as small as a few % accounting for the good performances of the AR coating. A tuning of the minimum of

4. SiGe-based Mie resonators as antireflection elements

R_{tot} is possible thanks to the different thicknesses of the additional conformal coatings. This leads to a shift in the minimum of R_{tot} from about 850 nm for sample II-C up to 1050 nm for sample II-A. Thus, also in this narrower spectral range, the effect of the additional conformal layers deposited atop the SiGe islands is to improve the AR properties of a factor of two or more with respect to bare islands. Furthermore, at normal incidence, sample II-B is more than a factor two more performing than a double layer composed of SiO_2 on Si_3N_4 (fig. 4.9).

Angle-resolved measurements of the specular reflectance SR are collected with an ellipsometer (thus disregarding the reflected scattering RD, fig. 4.8b). Averaging the specular reflectance for s and p polarizations and normalizing this value to that one measured on a Si wafer allows one to observe an excellent AR performance up to about 55° (fig. 4.8b, bottom panel).

In order to address the composition of the reflected light in terms of scattered and specular reflection we take into account the case of sample II-B for above band-gap frequencies. The reflected scattering (RD, defined as the total reflection minus the specular reflection: $\text{RD} = R_{\text{tot}} - \text{SR}$) at quasinormal incidence and integrated over the half solid angle is compared to the corresponding value of R_{tot} (fig. 4.10a). The similar values and spectral features of R_{tot} and RD allow us to conclude that most of the reflected light can be ascribed to the resonant backscattering from the SiGe Mie resonators distributed over the half solid angle atop the sample. The difference between R_{tot} and RD represents the specular reflectance SR and seems to play a minor role.

In order to better assess the composition and features of R_{tot} we characterized SR and RD at different incidence and collection angles by measuring the spectrally and angularly resolved bidirectional reflectance distribution function (BRDF) [70,71]. Here the incident beam and the detector are scanned along the same meridian and all the measured intensities are normalized to a Lambertian reference (the setup is shown in fig. 4.10c).

Spectrally integrated measurements show that the BRDF is composed by two distinct parts: a low-intensity, broad pedestal and a sharp peak which correspond to the scattered part RD and the specular reflection SR. The scattering RD (from 0.02 sr^{-1} to 0.06 sr^{-1} , fig. 4.10a) is about 2-3 times lower than that of bare SiGe islands on

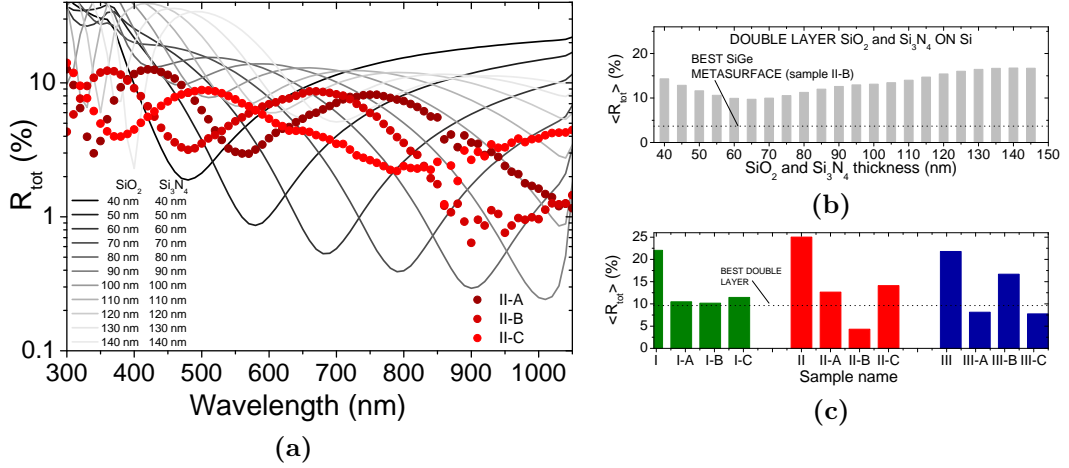


Figure 4.9: **a)** R_{tot} for samples II-A, -B and -C at above band-gap frequencies compared with that of a double layer of SiO_2 on Si_3N_4 on Si-bulk. The thickness of the two layers is changed from 40 nm on 40 nm up to 140 nm on 140 nm. **b)** Average value of the total reflectance $\langle R_{tot} \rangle$ integrated at frequencies larger than the Si band-gap for a double layer of SiO_2 on Si_3N_4 on Si-bulk as a function of the SiO_2 and Si_3N_4 thickness (some of the corresponding spectra are shown in **a**). The top horizontal dashed line sets the value of $\langle R_{tot} \rangle$ for Si-bulk. The bottom horizontal dashed line sets the value of $\langle R_{tot} \rangle$ for the best sample with SiGe islands and conformal layers (sample II-B). **c)** Average value of the total reflectance $\langle R_{tot} \rangle$ integrated at frequencies larger than the Si band-gap for the 3 samples series with SiGe islands. The top horizontal dashed line sets the value of $\langle R_{tot} \rangle$ for Si-bulk. The bottom horizontal dashed line sets the value of $\langle R_{tot} \rangle$ for the most performing AR based on SiO_2 on Si_3N_4 double layer on Si in this spectral range.

sample II [RD from 0.06 sr^{-1} to 0.1 sr^{-1}].

In a small cone (about 10°), the specular reflection is about two orders of magnitudes larger than the scattering and stays rather constant up to $\sim 50^\circ$, in agreement with fig. 4.8b. For excitation beams at angles larger than $\sim 40^\circ$, a slightly enhanced backscattering can be observed (highlighted by an arrow in the inset of fig. 4.10b).

By taking into account the case of excitation at 10° for sample II-B, it is possible to compare this result with those obtained with the spectrophotometer for the same sample (fig. 4.8a central panel) discriminating and quantifying SR and RD independently. Owing to the randomized position and size of the Mie resonators on our samples, the BRDF is invariant for revolutions around the vertical direction (not shown). Thus it is possible to integrate the scattered part over the half solid angle and the specular part over a small solid angle of about $\pm 5^\circ$ around its maximum, for both angular coordinates. From this analysis, we deduce that the SR is only a few % of R_{tot} , confirming

4. SiGe-based Mie resonators as antireflection elements

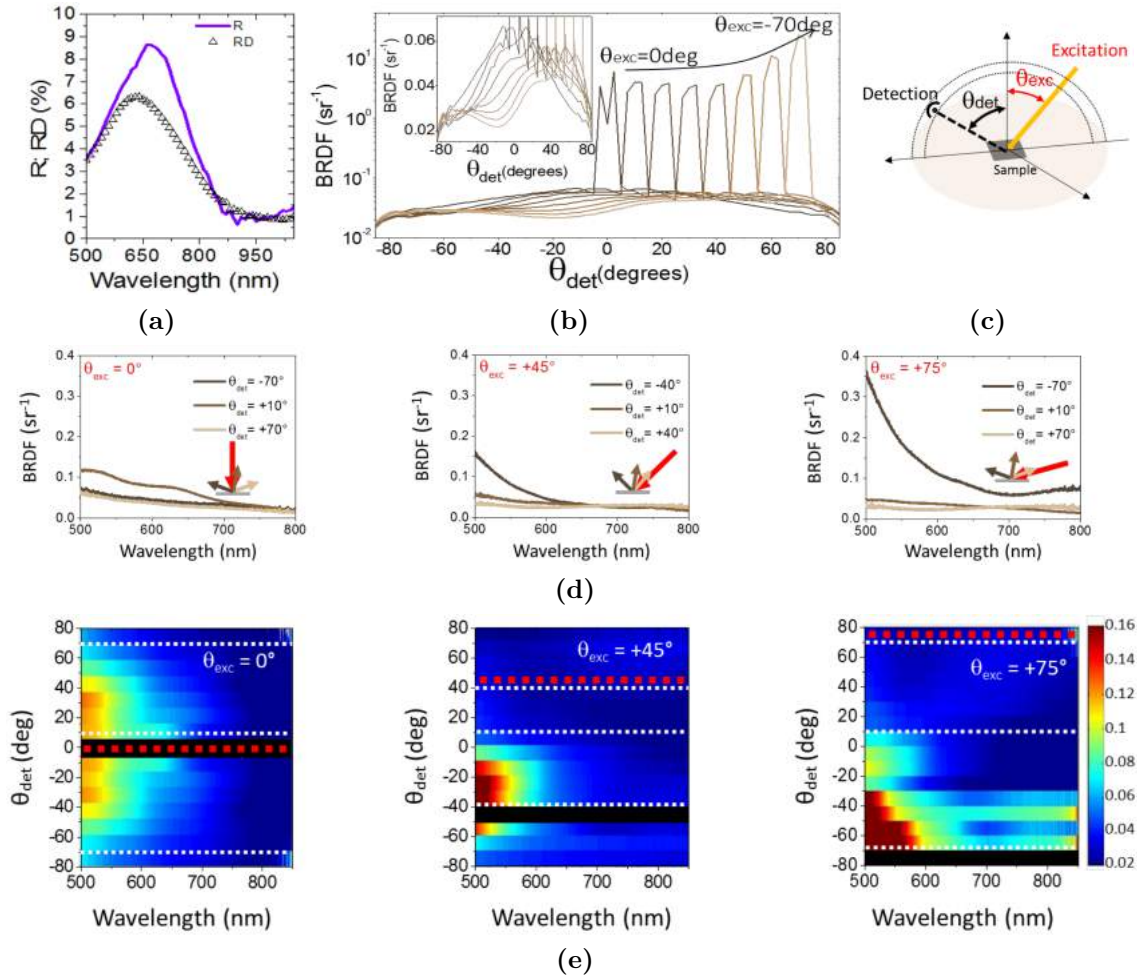


Figure 4.10: Comparison between reflected scattering (RD) and specular reflectance (SR) for sample II-B. **a)** Reflected scattering RD (black triangles) and R_{tot} (violet line) for sample II-B at quasi-normal incidence and integrated over the half solid angle atop the sample. **b)** Sketch of the experimental setup (diffusometer) used for detecting the bidirectional reflectance distribution function (BRDF). The angle of incidence of the excitation (θ_{exc}) and that of the detection (θ_{det}) can be scanned independently over the half solid angle on the same meridian. **c)** BRDF integrated from 400 nm to 800 nm for sample II-B measured for θ_{exc} from 0 to -70 degrees with respect to the normal to the sample surface and θ_{det} moving from -70 to +70. The sharp and intense peak is SR whereas the low-intensity pedestal is RD. Inset: zoom of the broad pedestal ascribed to RD. The black arrow highlights a slight increase of the RD for incident beam at large angles. **d)** Full dataset of the spectrally-resolved BRDF for sample II-B for $\theta_{exc} = 0, +45$ and $+75$ degrees (respectively from the top to the bottom panel). Each panel reports the intensity of the BRDF as a color-scale as a function of wavelength and of θ_{det} . The red dashed lines highlight θ_{exc} whereas the white dashed lines highlight the θ_{det} represented in **e)**. The black shaded areas hide the specular reflection. **e)** Spectrally-resolved BRDF for sample II-B at $\theta_{exc} = 0, +45$ and $+75$ degrees (respectively from the top to the bottom panel) for $\theta_{det} = -70, +10, +70$ degrees (top panel), $-40, +10, +40$ (central panel) and $-70, +10, +70$ (bottom panel). On each panel the inset displays the excitation (red arrow) and collection (brown arrows) geometry.

the result previously shown in fig. 4.8a for the integrated R_{tot} and RD.

Finally, the spectrally resolved BRDF for sample II-B is measured for three different directions of the incident beam, $\theta_{\text{exc}} = 0^\circ, +45^\circ$, and $+75^\circ$ (fig. 4.10e), whereas the detection is scanned from -80° to $+80^\circ$. From the full data sets, we select spectra at quasispecular, quasicollinear, quasivertical direction and large angles (fig. 4.10d). For all the incident angles, the BRDF features higher values at shorter wavelengths. For nearly specular detection, the BRDF is larger in all the investigated wavelength range and shows a marked increase at shorter wavelengths. Remarkably, for wavelengths larger than 600 nm the spectral and angular features are rather flat.

4.4 Discussion

The extensive optical characterization and simulations performed on our random metasurfaces give a precise insight in the redistribution of the impinging light and its enhanced coupling towards the Si substrate. The analysis of the BRDF demonstrates that the large part of the reflected light is scattered over the half solid angle atop the sample (about 95% of R_{tot}), while the intensity of specular reflection is very limited.

Reflectivity and transmission measurements reveal light trapping within the substrate, pointing at the completely different nature of our ARs with respect to conventional flat thin film coatings. In this latter case, R_{tot} is fully ascribed to specular reflection, rendering the coatings less adapted to all the applications where an increased propagation path of the photons in the device is necessary (e.g., for thin film photovoltaic). The working principle of our samples is similar to that of textured surfaces [9, 10] with the additional feature of resonances mediating the light coupling. In view of applications of our AR on thin-film photovoltaic cells or light detectors, the merit of our method is to avoid a direct texturing of the Si wafer, thus potentially preserving a high carrier mobility and lifetime [16].

The total reflectance in our disordered samples is strongly reduced over a broad band and a broad angle, in agreement with ordered Mie resonator arrays [15, 16, 18, 21]. We observe that, for ordered arrays of Si-based dielectric particles obtained with top-down methods, the best reported value of R_{tot} is about 2% for above band-gap frequencies,

whereas in the same spectral interval our best device reaches a value of less than 5%. However, for ordered arrays of Si-based Mie resonators a relevant effect reducing the value of R_{tot} is associated to the well-known Rayleigh anomaly [15] (grating effect), whereas in our case all the AR effect can be truly ascribed to the energy channeling mediated by the Mie resonances formed within the SiGe particles. Thus, owing to the randomness of our samples, we obtain a flatter spectral shape of R_{tot} with respect to previous reports [15].

In contrast with previous reports which focused only on above band-gap frequencies [15, 16, 18, 19, 21], we extended this idea to below band-gap frequencies in the near infrared ($\sim 1050\text{--}500\text{ nm}$), where R_{tot} can be as low as 7%. Moreover, we showed the possibility of tuning the minimum of R_{tot} both for below and above band-gap frequencies by adjusting the thickness of additional conformal layers deposited atop the SiGe islands. In addition, these conformal layers have the function of encapsulating the SiGe islands, rendering the metasurface more robust against mechanical damage and protecting the underlying structures from humidity.

A full assessment of the performances of our spontaneously assembled structures with respect to existing examples of dielectric Mie resonators in the literature should take into account the full range of frequencies addressed here, as well as the light trapping effect and the composition of light in terms of scattered reflection and specular reflection. Unfortunately, these data are not available in the literature and a comparison is not possible, which further accounts for the importance of our findings and characterizations.

In principle, this fabrication method can be performed at relatively low temperature [57] (e.g., at $300\text{ }^\circ\text{C}$ for thin, amorphous Ge layers) and it can be used on custom-made arbitrary SiO_2 layers [43, 44], relaxing the need of a commercial UT-SOI. Importantly, the duration of the dewetting process does not depend on the sample size, but only on the thickness of the thin Si(Ge) layer and lowering the temperature budget is possible, in spite of a longer annealing time. In principle, this fabrication method offers the possibility to implement efficient AR coatings on existing devices [58] (e.g., photovoltaic cells, C-MOS and CCD cameras, and Si- and Ge-based photodetectors).

4.5 Conclusions

We showed that joining annealing of these silicon films with epitaxial growth enables the formation of high density SiGe-based islands featuring a large vertical aspect ratio, a large spread of size with a good spatial isotropy of the particles' size distribution. Our method represents a step forward in self-assembly of 3D structures where the size and the density of the particles are usually correlated.

The performances of our device can be adapted and improved employing an optimized *ad hoc* buried oxide [43, 44, 56] and targeting specific wavelength ranges with an appropriate choice of particle size. These possibilities bring the additional advantage of relaxing the need for expensive commercial UT-SOI [43, 44], opening up the use of this method on other substrates (e.g., glass, Ge, and SiC).

The strengths of this method are manifold: (I) the duration of the process does not depend on the extension of the wafer but only on the composition and thickness of the top thin layer; (II) dewetting can be exploited at relatively low temperature [57] and thus it can be compatible with back-end processing of C-MOS circuitry [58]; (III) it is a lithography-free approach avoiding multiple, polluting, chemical cleaning steps as it relies only on deposition and annealing; (IV) it provides efficient AR in extremely broad ranges of frequencies exceeding those shown so far for similar systems [15, 16, 18, 19, 21].

4.6 Methods

4.6.1 Samples' fabrication

A scheme of the process used is shown in fig. 4.11. The UT-SOI substrates used here were commercial single-crystal (001) oriented, 12 nm thick Si films atop 20 nm thick buried oxide on a Si (001) wafer. The wafer was double polished. After a chemical cleaning for 30 sec in a 10% $HF-H_2O$ solution under nitrogen atmosphere, the samples were transferred to the ultra-high vacuum (UHV $\sim 10^{-10}$ Torr) of a molecular beam epitaxy reactor. The annealing was performed in two steps: first at 700 ° C for 30 sec in order to remove any residual native oxide from the sample surface. Following

4. SiGe-based Mie resonators as antireflection elements

this, the temperature was increased up to at 800 °C and 2 monolayers (MNLs) of Ge were supplied a rate of 6.5Å/ min in order to trigger the dewetting. After annealing for 4 hours 300 MNLs of Ge were supplied at a deposition rate of 6.5Å/ min at the same temperature. The deposition lasted for about 125 min. We fabricated 3 samples (I, II, III) by using slightly different orientation of the sample holder with respect to direction of the molecular Ge flux (respectively 20, 25 and 30 degrees in the reference frame of the growth machine). The final Ge content of the SiGe islands is nominally ~90% even if small differences in the Ge content in the 3 samples are possible. The growth via molecular beam epitaxy represents the pinnacle of the deposition quality and of the purity of the atomic species and with a control over the deposited amount of material as precise as 1/10 of an atomic monolayer (e.g. by monitoring the deposition rate in situ with a RHEED, or after calibration of the effusion cells). Other sources of error during fabrication are the temperature of the sample surface during dewetting and Ge deposition (a few percentages) and the orientation of the sample surface with respect to the molecular beam (a few percentages). Thus, we evaluate the error in the samples reproducibility by fabricating two nominally identical samples and measuring the corresponding value of the total reflectivity R_{tot} . The difference in the measured R_{tot} for the two samples is less than ~1% accounting for a good control over the sample properties (not shown). In order to protect the SiGe islands, tune and improve the AR performances of the implemented devices, the as-grown samples I, II and III were coated with conformal layers of Si_3N_4 and SiO_2 formed via plasma-enhanced chemical

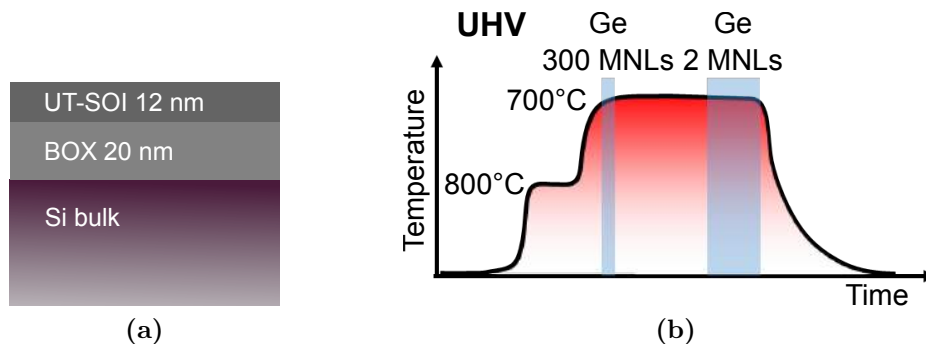


Figure 4.11: **a)** Diagram of the UT-SOI sample composition (12 nm of monocrystalline Si atop 20 nm of buried oxide, BOX) and description of the fabrication steps (i-iv). **b)** The bottom part describes the annealing cycle in the ultra-high vacuum (UHV) of the molecular beam reactor and the Ge deposition steps.

vapor deposition [59]. Two dimensional interferential layers were also deposited on the backside of the samples in order to reduce the reflection from this interface for blow band-gap frequencies. The description of the different samples with the corresponding thickness of the SiO₂ and Si₃N₄ layers is provided in table 4.1.

4.6.2 Morphological characterization techniques

The structural characterization of the islands' morphology (size, shape and composition of the SiGe islands) was performed ex situ by scanning electron microscopy (SEM, Dualbeam FIB HELIOS 600 nanolab), atomic force microscopy (AFM, PSIA XE-100 AFM) in non-contact mode and cross section transmission electron microscopy (TEM Jeol JEM - 2010).

SEM characterization

The size of SiGe islands for sample I, II and III show a bimodal distribution with a large number of small particles (below 100 nm in diameter) and a second family of large islands (above 100 nm in diameter) as accounted for by a statistical investigation of high- resolution SEM images (figs. 4.12a and 4.12b). The absence of bright spots in the two-dimensional Fourier transform of a SEM image of sample II accounts for the completely randomized island formation (cf. inset in the central panel of fig. 4.2b). Islands' average base size ($\langle L \rangle = (L_M + L_m)/2$, where L_M and L_m are respectively the longer and shorter particle' diameter, fig. 4.12a)) and the corresponding in-plane asymmetry ($\epsilon = (L_M - L_m)/(L_m + L_M)$, fig. 4.12b) are respectively in the range of few tens of nm up to ~ 500 nm and from 0 up to ~ 0.6 . No marked dependency of the asymmetry on particles' size is highlighted.

AFM characterization

The islands morphology and its evolution with the increasing thickness of a conformal layer deposited via chemical vapor deposition was monitored by AFM imaging (fig. 4.13). Here we show the case of sample II, II-A, -B and -C (see table 4.1 for the details of the conformal layers on the SiGe islands). Typical height profiles extracted from AFM measurements show islands featuring geometrical aspect ratios (h/r , where

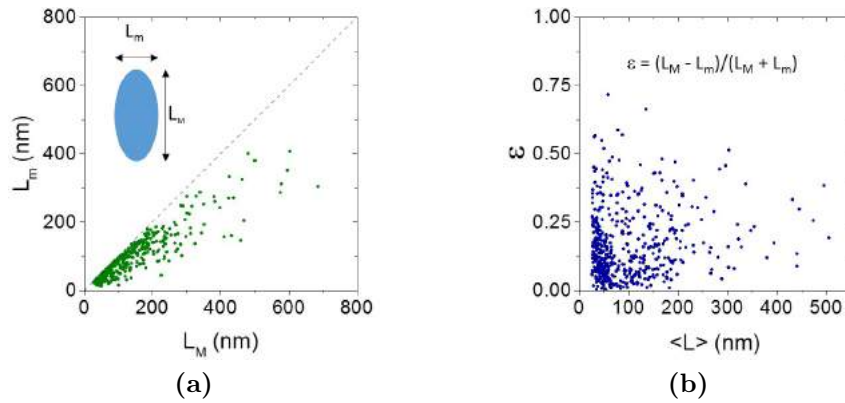


Figure 4.12: **a)** Shorter island side (L_m) as a function of the corresponding longer islands side (L_M). The diagonal line represents the symmetric island case $L_m = L_M$, $\epsilon = 0$. The smaller size limit is set at 30 nm (due to the limited lateral resolution of the SEM image), thus the size distribution is artificially cut. **b)** Island asymmetry ϵ as a function of the average island side $\langle L \rangle$.

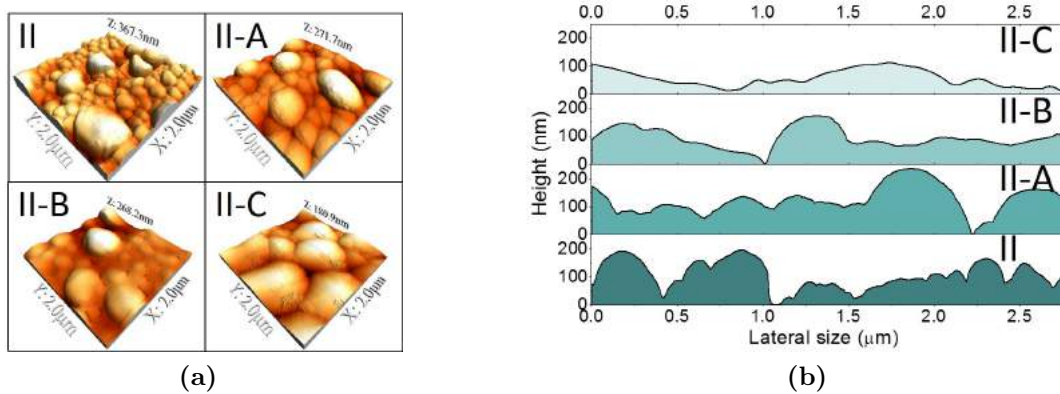


Figure 4.13: **a)** AFM characterization. Starting from the left-top panel, in clockwise order are respectively represented 3D perspective view of sample II, II-A, II-B and II-C. **b)** Height profiles extracted from **a)**. From the bottom to the top panels are respectively shown samples II, I-A, II-B and II-C.

h is the particle's height and $r = d/2$ is the half of its base size) exceeding 0.7 in agreement with recent reports for SiGe-based dewetted islands [44, 48]. A progressive smoothing of the samples' roughness when increasing the thickness of the conformal double layer atop the SiGe islands is observed, as expected (root mean square, RMS from ~ 58 nm for sample I up to ~ 35 nm for sample II-C, fig. 4.13b). We mention that the value of the roughness for the bare islands (and thus also their vertical aspect ratio) may be slightly underestimated owing to their close packing.

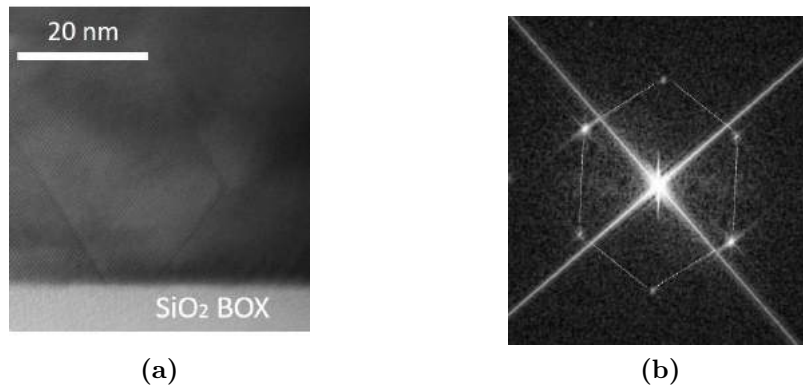


Figure 4.14: **a)** Detail of misfit dislocations at the interface between the base of a large SiGe island and the underlying buried oxide. **b)** The top right inset displays the Fourier transform of the crystalline part shown in the main panel. The hexagonal pattern of bright spots is highlighted by dashed lines.

TEM characterization

TEM investigation of large and small islands is performed, confirming their large aspect ratio ($h/r > 0.5$) in agreement with AFM data (fig. 4.1b) and previous reports on similar systems [43, 47]. A closer inspection of high-resolution TEM images reveals the presence of misfit dislocations (figs. 4.14a and 4.14b) eventually crossing the full islands or annihilating one with the other. This feature is found in both families of particles and was never observed before. Here it is worth noting that in previous reports of SiGe dewetting, larger temperature were used (e.g. 820 °C in reference [53] and 850 °C in [60]). In this cases strong spatial inhomogeneities of particles' size and shape together with preferential alignment of the islands along the crystallographic axes and relatively large in-plane elongations were found. Thus, we conclude that keeping the dewetting temperature below ~ 800 °C induces the simultaneous break-up of the thin SiGe film starting from many void-nucleation points while avoiding local accumulation of Ge at the receding rims. This leads to a complete lack of inhomogeneity in the spatial arrangement and anisotropy in the particles' shape.

4.6.3 Spectroscopic techniques

The spectroscopic characterization of light reflection, transmission and reflected scattering was performed on the Mie resonators ensemble with a spectrophotometer mounting an integrating sphere for near-normal light incidence (11 degrees with respect to

4. SiGe-based Mie resonators as antireflection elements

the sample normal). Angle-resolved measurements of specular reflectance (at incident angles between 45 and 80 degrees) for s and p polarizations were performed with an ellipsometer (Woollam M2000V). The bidirectional reflectance distribution function (BRDF) was measured with a spectro-polarimetric goniometer (Light Tec). For spectrally integrated measurements at visible (near-infrared) frequencies a Si-based (InGaAs-based) photo-diode was used. For spectrally-resolved measurements of the BRDF at visible frequencies the spectro-polarimetric goniometer was coupled to a spectrometer (FLAME, Ocean Optics) via a 200 μm core, multi-mode optical fiber.

4.6.4 Theoretical simulations

FDTD simulations were performed with a commercial software (Lumerical) by taking into account 2 families of islands (perfectly bimodal size distribution, approximating the statistical distribution of the particles' size found in experiments): smaller islands featuring a diameter of 150 nm, and larger islands of 450 nm. The islands' shape is assumed to be a half sphere (this is a rather good approximation for Ge-rich SiGe islands [44, 53]). The islands' positions is obtained with a random number generator while avoiding overlaps between them. The FDTD simulations take into account the eventual lateral photonic coupling between islands (e.g. for particles working at visible frequencies a lateral coupling is possible when the border-to-border distance is lower than ~ 100 nm). The density of the islands is set in order to reproduce that one of the experimental case according to the filling factor associated to each family. A sketch of the particles' distribution for each family is shown in fig. 4.15. The refractive index dispersion and the absorption of the SiGe alloy is taken into account (by comparing n and k for bare Si and bare Ge, $\text{Si}_{0.1}\text{Ge}_{0.9}$ is shown assuming an effective medium

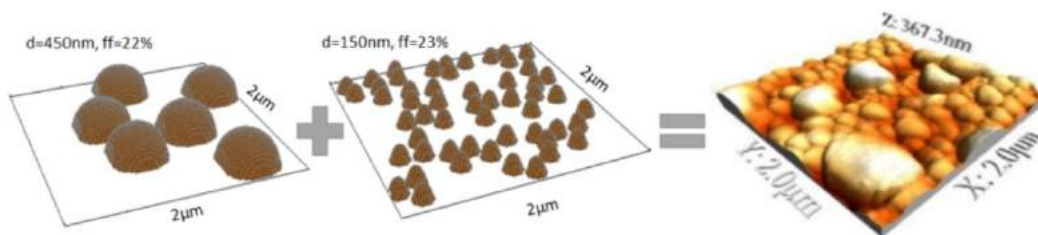


Figure 4.15: Spatial distribution of large (450 nm in diameter) and small (150 nm in diameter) islands used for the FDTD simulation of R_{tot} are shown respectively in the left and central panels.

model). The impinging white light is assumed to be a plane wave at normal incidence with respect to the sample surface. The scattering cross section is evaluated for individual particles (no lateral coupling is considered). Finally, the total reflectance R_{tot} is obtained as the sum of two parts, one from the large islands and the other one from the small ones. In this case the eventual lateral coupling is taken into account in the FDTD simulation.

References

- [1] S. Chattopadhyay, Y. Huang, Y.-J. Jen, A. Ganguly, K. Chen, and L. Chen. “Anti-reflecting and photonic nanostructures”. In: *Materials Science and Engineering: R: Reports* 69.1 (2010), pp. 1–35.
- [2] H. K. Raut, V. A. Ganesh, A. S. Nair, and S. Ramakrishna. “Anti-reflective coatings: A critical, in-depth review”. In: *Energy & Environmental Science* 4.10 (2011), pp. 3779–3804.
- [3] M. L. Brongersma, Y. Cui, and S. Fan. “Light management for photovoltaics using high-index nanostructures”. In: *Nature materials* 13.5 (2014), pp. 451–460.
- [4] I.-S. Yu, Y.-W. Wang, H.-E. Cheng, Z.-P. Yang, and C.-T. Lin. “Surface passivation and antireflection behavior of ALD on n-type silicon for solar cells”. In: *International Journal of Photoenergy* 2013 (2013).
- [5] K. Kim, G. Y. Song, Y. T. Kim, J. H. Moon, and J. Heo. “Simulation and deposition of near-IR anti-reflection layers for silicon substrates”. In: *Surface and Coatings Technology* (2017).
- [6] E. Yablonovitch and G. D. Cody. “Intensity enhancement in textured optical sheets for solar cells”. In: *IEEE Transactions on Electron Devices* 29.2 (1982), pp. 300–305.
- [7] L. Escoubas, J. Simon, M. Loli, G. Berginc, F. Flory, and H. Giovannini. “An antireflective silicon grating working in the resonance domain for the near infrared spectral region”. In: *Optics communications* 226.1 (2003), pp. 81–88.
- [8] Y.-F. Huang, S. Chattopadhyay, Y.-J. Jen, C.-Y. Peng, T.-A. Liu, Y.-K. Hsu, C.-L. Pan, H.-C. Lo, C.-H. Hsu, Y.-H. Chang, et al. “Improved broadband and quasi-omnidirectional anti-reflection properties with biomimetic silicon nanostructures”. In: *Nature nanotechnology* 2.12 (2007), pp. 770–774.
- [9] X. Sheng, S. G. Johnson, J. Michel, and L. C. Kimerling. “Optimization-based design of surface textures for thin-film Si solar cells”. In: *Optics Express* 19.104 (2011), A841–A850.

-
- [10] V. Ganapati, O. D. Miller, and E. Yablonovitch. “Light trapping textures designed by electromagnetic optimization for subwavelength thick solar cells”. In: *IEEE Journal of Photovoltaics* 4.1 (2014), pp. 175–182.
- [11] J. Yang, F. Luo, T. S. Kao, X. Li, G. W. Ho, J. Teng, X. Luo, and M. Hong. “Design and fabrication of broadband ultralow reflectivity black Si surfaces by laser micro/nanoprocessing”. In: *Light: Science & Applications* 3.7 (2014), e185.
- [12] H. A. Atwater and A. Polman. “Plasmonics for improved photovoltaic devices”. In: *Nature materials* 9.3 (2010), pp. 205–213.
- [13] R. H. Siddique, J. Mertens, H. Hölscher, and S. Vignolini. “Scalable and controlled self-assembly of aluminium-based random plasmonic metasurfaces”. In: (2017).
- [14] N. Odebo Länk, R. Verre, P. Johansson, and M. Käll. “Large-scale silicon nanophotonic metasurfaces with polarization independent near-perfect absorption”. In: *Nano Letters* 17.5 (2017), pp. 3054–3060.
- [15] P. Spinelli, M. Verschuuren, and A. Polman. “Broadband omnidirectional antireflection coating based on subwavelength surface Mie resonators”. In: *Nature Communications* 3 (2012), p. 692.
- [16] P. Spinelli, B. Macco, M. Verschuuren, W. Kessels, and A. Polman. “Al₂O₃/TiO₂ nano-pattern antireflection coating with ultralow surface recombination”. In: *Applied Physics Letters* 102.23 (2013), p. 233902.
- [17] N. Fofang, T. Luk, M. Okandan, G. Nielson, and I. Brener. “Substrate-modified scattering properties of silicon nanostructures for solar energy applications”. In: *Optics express* 21.4 (2013), pp. 4774–4782.
- [18] J. Proust, A.-L. Fehrembach, F. Bedu, I. Ozerov, and N. Bonod. “Optimized 2D array of thin silicon pillars for efficient antireflective coatings in the visible spectrum”. In: *Scientific reports* 6 (2016), p. 24947.
- [19] J. Choi, T. S. Lee, D. S. Jeong, W. S. Lee, W. M. Kim, K.-S. Lee, D. Kim, and I. Kim. “Random Si nanopillars for broadband antireflection in crystalline silicon solar cells”. In: *Journal of Physics D: Applied Physics* 49.37 (2016), p. 375108.

- [20] V. E. Babicheva, M. I. Petrov, K. V. Baryshnikova, and P. A. Belov. “Reflection compensation mediated by electric and magnetic resonances of all-dielectric metasurfaces”. In: *JOSA B* 34.7 (2017), pp. D18–D28.
- [21] T. Bottein, T. Wood, T. David, J. B. Claude, L. Favre, I. Berb ezier, A. Ronda, M. Abbarchi, and D. Grosso. ““Black” Titania Coatings Composed of Sol–Gel Imprinted Mie Resonators Arrays”. In: *Advanced Functional Materials* 27.2 (2017).
- [22] J. A. Schuller, R. Zia, T. Taubner, and M. L. Brongersma. “Dielectric metamaterials based on electric and magnetic resonances of silicon carbide particles”. In: *Physical review letters* 99.10 (2007), p. 107401.
- [23] Q. Zhao, J. Zhou, F. Zhang, and D. Lippens. “Mie resonance-based dielectric metamaterials”. In: *Scientific Reports* 12 (2009), pp. 60–69.
- [24] A. B. Evlyukhin, C. Reinhardt, A. Seidel, B. S. Luk’yanchuk, and B. N. Chichkov. “Optical response features of Si-nanoparticle arrays”. In: *Physical Review B* 82.4 (2010), p. 045404.
- [25] A. B. Evlyukhin, S. M. Novikov, U. Zywiets, R. L. Eriksen, C. Reinhardt, S. I. Bozhevolnyi, and B. N. Chichkov. “Demonstration of magnetic dipole resonances of dielectric nanospheres in the visible region”. In: *Nano letters* 12.7 (2012), pp. 3749–3755.
- [26] A. B. Evlyukhin, C. Reinhardt, E. Evlyukhin, and B. N. Chichkov. “Multipole analysis of light scattering by arbitrary-shaped nanoparticles on a plane surface”. In: *JOSA B* 30.10 (2013), pp. 2589–2598.
- [27] D. Lin, P. Fan, E. Hasman, and M. L. Brongersma. “Dielectric gradient metasurface optical elements”. In: *science* 345.6194 (2014), pp. 298–302.
- [28] J. S. and J. Z. “All-dielectric metamaterials”. In: *Nat. Nanotechnol.* 11 (2016), pp. 23–36.
- [29] X. Li, J. Gao, L. Xue, and Y. Han. “Porous Polymer Films with Gradient-Refractive-Index Structure for Broadband and Omnidirectional Antireflection Coatings”. In: *Advanced Functional Materials* 20.2 (2010), pp. 259–265.

-
- [30] K. Vynck, M. Burrese, F. Riboli, and D. S. Wiersma. “Photon management in two-dimensional disordered media”. In: *Nature materials* 11.12 (2012), pp. 1017–1022.
- [31] M. Burrese, F. Pratesi, K. Vynck, M. Prasciolu, M. Tormen, and D. S. Wiersma. “Two-dimensional disorder for broadband, omnidirectional and polarization-insensitive absorption”. In: *Optics express* 21.102 (2013), A268–A275.
- [32] C. Rockstuhl and T. Scharf. *Amorphous nanophotonics*. Springer Science & Business Media, 2013.
- [33] H. Yasuda, R. Matsuno, N. Koito, H. Hosoda, T. Tani, and M. Naya. “Anti-reflective coating for visible light using a silver nanodisc metasurface with a refractive index of less than 1.0”. In: *Applied Physics Letters* 111.23 (2017), p. 231105.
- [34] Y. Wu, J. D. Fowlkes, and P. D. Rack. “The optical properties of Cu-Ni nanoparticles produced via pulsed laser dewetting of ultrathin films: The effect of nanoparticle size and composition on the plasmon response”. In: *Journal of Materials Research* 26.02 (2011), pp. 277–287.
- [35] S. Hong, T. Kang, D. Choi, Y. Choi, and L. P. Lee. “Self-assembled three-dimensional nanocrown array”. In: *ACS nano* 6.7 (2012), pp. 5803–5808.
- [36] A. B. Tesler, B. M. Maoz, Y. Feldman, A. Vaskevich, and I. Rubinstein. “Solid-state thermal dewetting of just-percolated gold films evaporated on glass: development of the morphology and optical properties”. In: *The Journal of Physical Chemistry C* 117.21 (2013), pp. 11337–11346.
- [37] S. Morawiec, M. J. Mendes, S. Mirabella, F. Simone, F. Priolo, and I. Crupi. “Self-assembled silver nanoparticles for plasmon-enhanced solar cell back reflectors: correlation between structural and optical properties”. In: *Nanotechnology* 24.26 (2013), p. 265601.
- [38] F. Bisio, R. Proietti Zaccaria, R. Moroni, G. Maidecchi, A. Alabastri, G. Gonella, A. Giglia, L. Andolfi, S. Nannarone, L. Mattera, et al. “Pushing the high-energy limit of plasmonics”. In: *ACS nano* 8.9 (2014), pp. 9239–9247.

- [39] S. V. Makarov, V. A. Milichko, I. S. Mukhin, I. I. Shishkin, D. A. Zuev, A. M. Mozharov, A. E. Krasnok, and P. A. Belov. “Controllable femtosecond laser-induced dewetting for plasmonic applications”. In: *Laser & Photonics Reviews* 10.1 (2016), pp. 91–99.
- [40] R. Yu, P. Mazumder, N. F. Borrelli, A. Carrilero, D. S. Ghosh, R. A. Maniyara, D. Baker, F. J. Garcia de Abajo, and V. Pruneri. “Structural coloring of glass using dewetted nanoparticles and ultrathin films of metals”. In: *ACS Photonics* 3.7 (2016), pp. 1194–1201.
- [41] S. Kunwar, M. Sui, Q. Zhang, P. Pandey, M.-Y. Li, and J. Lee. “Various Silver Nanostructures on Sapphire Using Plasmon Self-Assembly and Dewetting of Thin Films”. In: *Nano-Micro Letters* 9.2 (2017), p. 17.
- [42] M. Abbarchi, M. Naffouti, B. Vial, A. Benkouider, L. Lermusiaux, L. Favre, A. Ronda, S. Bidault, I. Berbezier, and N. Bonod. “Wafer scale formation of monocrystalline silicon-based mie resonators via silicon-on-insulator dewetting”. In: *ACS nano* 8.11 (2014), pp. 11181–11190.
- [43] M. Naffouti, T. David, A. Benkouider, L. Favre, A. Ronda, I. Berbezier, S. Bidault, N. Bonod, and M. Abbarchi. “Fabrication of poly-crystalline Si-based Mie resonators via amorphous Si on SiO₂ dewetting”. In: *Nanoscale* 8.5 (2016), pp. 2844–2849.
- [44] T. Wood, M. Naffouti, J. Berthelot, T. David, J.-B. Claude, L. Métayer, A. Delobbe, L. Favre, A. Ronda, I. Berbezier, et al. “All-dielectric color filters using SiGe-based Mie resonator arrays”. In: *ACS photonics* 4.4 (2017), pp. 873–883.
- [45] M. Naffouti, R. Backofen, M. Salvalaglio, T. Bottein, M. Lodari, A. Voigt, T. David, A. Benkouider, I. Fraj, L. Favre, et al. “Complex dewetting scenarios of ultrathin silicon films for large-scale nanoarchitectures”. In: *Science advances* 3.11 (2017), eaao1472.
- [46] M. Aouassa, I. Berbezier, L. Favre, A. Ronda, M. Bollani, R. Sordan, A. Delobbe, and P. Sudraud. “Design of free patterns of nanocrystals with ad hoc features via templated dewetting”. In: *Applied Physics Letters* 101.1 (2012), p. 013117.

-
- [47] E. Sutter and P. Sutter. “Assembly of Ge nanocrystals on SiO₂ via a stress-induced dewetting process”. In: *Nanotechnology* 17.15 (2006), p. 3724.
- [48] M. Naffouti, T. David, A. Benkouider, L. Favre, A. Delobbe, A. Ronda, I. Berbezier, and M. Abbarchi. “Templated Solid-State Dewetting of Thin Silicon Films”. In: *Small* 12.44 (2016), pp. 6115–6123.
- [49] D. T. Danielson, D. K. Sparacin, J. Michel, and L. C. Kimerling. “Surface-energy-driven dewetting theory of silicon-on-insulator agglomeration”. In: *Journal of applied physics* 100.8 (2006), p. 083507.
- [50] F. Cheynis, E. Bussmann, F. Leroy, T. Passanante, and P. Müller. “Dewetting dynamics of silicon-on-insulator thin films”. In: *Physical Review B* 84.24 (2011), p. 245439.
- [51] M. Aouassa, L. Favre, A. Ronda, H. Maaref, and I. Berbezier. “The kinetics of dewetting ultra-thin Si layers from silicon dioxide”. In: *New Journal of Physics* 14.6 (2012), p. 063038.
- [52] F. Leroy, F. Cheynis, T. Passanante, and P. Müller. “Dynamics, anisotropy, and stability of silicon-on-insulator dewetting fronts”. In: *Physical Review B* 85.19 (2012), p. 195414.
- [53] M. Naffouti, T. David, A. Benkouider, L. Favre, M. Cabie, A. Ronda, I. Berbezier, and M. Abbarchi. “Fabrication of core-shell nanostructures via silicon on insulator dewetting and germanium condensation: towards a strain tuning method for SiGe-based heterostructures in a three-dimensional geometry”. In: *Nanotechnology* 27.30 (2016), p. 305602.
- [54] P. Zhang, B. Yang, P. Rugheimer, M. Roberts, D. Savage, F. Liu, and M. Lagally. “Influence of germanium on thermal dewetting and agglomeration of the silicon template layer in thin silicon-on-insulator”. In: *Journal of Physics D: Applied Physics* 42.17 (2009), p. 175309.
- [55] M. Abbarchi, M. Naffouti, B. Vial, A. Benkouider, L. Lermusiaux, L. Favre, A. Ronda, S. Bidault, I. Berbezier, and N. Bonod. “Wafer scale formation of monocrystalline silicon-based mie resonators via silicon-on-insulator dewetting”. In: *ACS nano* 8.11 (2014), pp. 11181–11190.

- [56] J. Van de Groep and A. Polman. “Designing dielectric resonators on substrates: Combining magnetic and electric resonances”. In: *Optics express* 21.22 (2013), pp. 26285–26302.
- [57] Y. Wakayama, T. Tagami, and S.-i. Tanaka. “Three-dimensional islands of Si and Ge formed on SiO₂ through crystallization and agglomeration from amorphous thin films”. In: *Thin Solid Films* 350.1 (1999), pp. 300–307.
- [58] Y. H. D. Lee and M. Lipson. “Back-end deposited silicon photonics for monolithic integration on CMOS”. In: *IEEE Journal of Selected Topics in Quantum Electronics* 19.2 (2013), p. 8200207.
- [59] P. Spinelli, M. Verschuuren, and A. Polman. “Broadband omnidirectional antireflection coating based on subwavelength surface Mie resonators”. In: *Nature Communications* 3 (2012), p. 692.
- [60] P. P. Zhang, B. Yang, P. P. Rugheimer, M. M. Roberts, D. E. Savage, F. Liu, and M. G. Lagally. “Influence of germanium on thermal dewetting and agglomeration of the silicon template layer in thin silicon-on-insulator”. In: *Journal of Physics D: Applied Physics* 42 (2009), p. 175309.

Chapter 5

Ongoing activities

After discussing the settled results appeared in scientific publications, and before addressing conclusions and long term perspectives, this short chapter ventures out to a pair of topics, still remained in progress at the end of this thesis. In these works, the experimental part has already been performed, but the theoretical analysis needs more development before publication. These issues are in close relationship with all the techniques described previously and the starting points are from one side the Titania spheres presented in chapter 2, from the other side dewetted metasurfaces, as the ones described in chapter 4, integrated on soft sol-gel substrates via nano-imprint lithography (chapter 3). In particular here we are going to present a work in which dielectric Titania spheres are integrated with light emitters, in this case perovskite nano-crystals, exploiting these structures as all-dielectric antennas. Furthermore, still keeping in mind the possibility of integration between single emitters and Mie resonators, we will present a method for transfer dielectric nanoresonators obtained via solid state dewetting on low refractive index substrates. In contrast to silicon wafer, where typically grew up dewetted structures, low refractive index substrates have less influence on Mie resonances, rendering this solution more suitable in exploitation the antenna properties of such devices.

5.1 Integrated all-dielectric photonic with perovskite nano-crystals

The integration of photon emitters with dielectric [1] or metallic [2] structures is one of the most explored fields of nano-photonics. Spontaneous emission from light sources, such as quantum dots, active semiconductor or nitrogen–vacancy centres in diamond, can be enhanced and controlled by coupling their electric field with nanoantennas. In particular, modification of the emission rate by changing the local density of state [3] and beaming of emission from dipole-like pattern to directional profile [4] are some results achievable by using such kind of integrated system. In addition, the peculiar Kerker conditions of Mie resonators (i.e. forward scattering when electric and magnetic resonances overlap -section 1.2.1) can indeed enhance the collection efficiency for single photon sources. One main challenge is then the integration of single emitters with all-dielectric nanoantennas, potentially tuning the Mie resonance to the wavelength of spontaneous emission. Such goal requires fabrication methods suitable for realizing single all-dielectric resonators in combination with a technique that allows the emitter to be placed in the close proximity of the antenna itself. As we have seen, these techniques, when high throughput and possibly cost-effective, represent the state of the art of Mie resonators fabrication and the capability of coupling with single nano-emitters constitutes a further step forward.

Going in this interesting direction, we started to explore the coupling between single

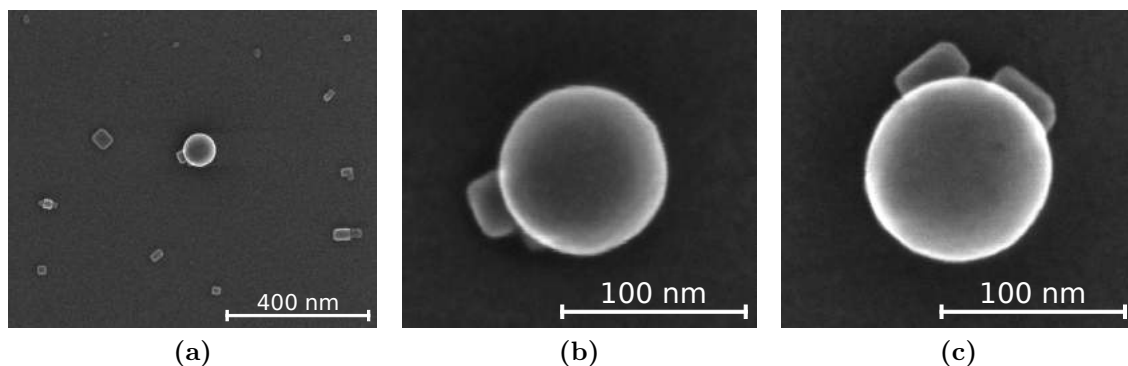


Figure 5.1: Scanning electron images of the realized sample on which PNCs are coupled with Titania spheres. **a)** Wide field SEM image where are shown single and isolated PNCs and PNCs coupled with a sphere. **b)** PNCs couple with spheres both individually and in clusters **c)**

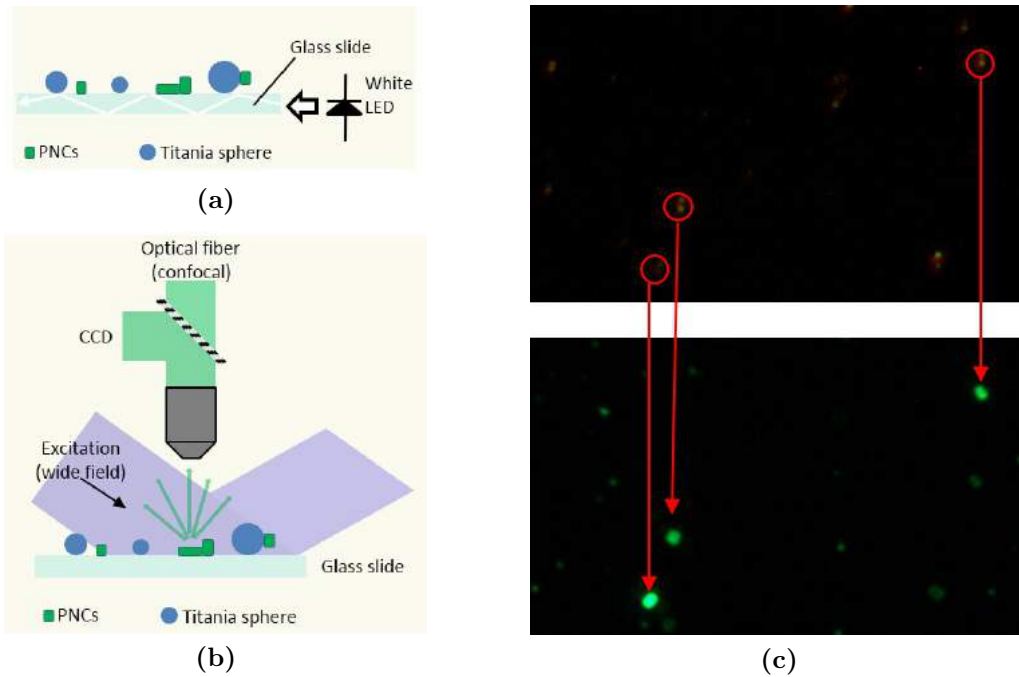


Figure 5.2: **a)** Sketch of the setup used for exciting resonances inside Titania sphere: the white light channeled into the slab is used for coupling with Mie resonances. **b)** Sketch of the setup used for wide field excitation of PL from perovskites. Here the excitation source is a 400 nm laser source. **c)** Scattering from the Titania spheres (top) and PL signal from the sample where PNCs are coupled with the spheres. Here the width of the field of view is about $100\ \mu\text{m}$.

Titania spheres and individual perovskite nanocrystals. Titania spheres were realized as described in section 2.4 of chapter 2, by using aerosol spray on glass substrate. Regarding the fabrication of perovskite nano-crystals, the procedure described in [5] was followed. This allows for the realization of Methylammonium Lead Bromide Nanocrystals (PNCs) dispersed in toluene and maintained as a colloidal dispersion. The PNCs synthesized with this method have diameter in the 30-50 nm range, and form large assemblies both in suspension and after drop-cast deposition on substrates. Scanning electron microscope images show how PNCs form on top of the substrate where Titania spheres are placed (fig. 5.1). Here we can see that some PNCs rest coupled with the spheres while the most of them are spread along the glass, individually or in small clusters.

In order to investigate the effect of the coupling between perovskites and Mie resonators, photoluminescence of PNCs was studied. Perovskites were excited by 400 nm laser source, collecting their photoluminescence (PL) with CCD camera for imaging and

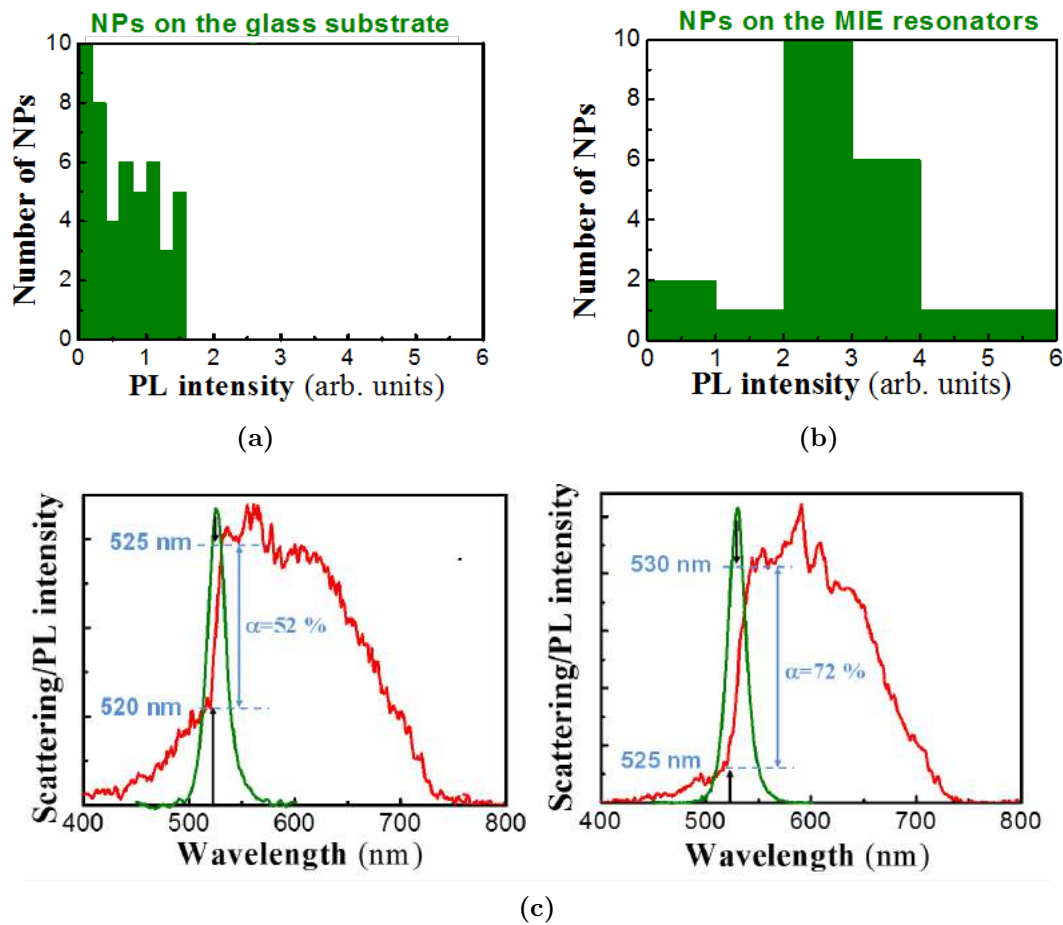


Figure 5.3: a) Photoluminescence distribution from isolated perovskites on glass substrate. b) Photoluminescence distribution from perovskites coupled with Titania spheres. c) Scattering from spheres coupled to perovskites (red lines) and relative PL from the PNC (green lines), for different systems perovskite-Mie sphere. Scattering measurements were performed with the set-up sketched in fig. 5.2a, while PL measurements with the set-up in fig. 5.2b.

with a confocal optical fiber for spectral analysis of a single nano-object.. A simplified sketch of the set-up is represented in fig. 5.2. Mie resonances supported by Titania spheres were excited by channeling the light into the glass substrate, as it behaves like a light guide. This allows to know the right position of the spheres on the substrate, in order to compare, once PL measurements were done, the relative position between spheres and perovskites, making possible to relate PL coming from PNCs isolated and coupled to the resonators. This relationship is underlined in fig. 5.2c, where is shown on the top a map of the scattering from the Titania spheres and on the bottom the PL from the perovskites. Here, we can observe how PL is enhanced by the coupling with the resonators. This result is assessed by statistical investigation of emission centers,

both single and coupled with spheres. In figs. 5.3a and 5.3b is reported a bar chart of the PL intensity distribution coming from isolated perovskites and PNCs in close proximity with the spheres, respectively, from which it's possible to confirm the precedent claim.

Moreover, by looking at the scattering signal from the spheres, when these are coupled with the perovskites, we observed a sharp decreasing at the of the absorption edge of the perovskites, as reported in fig. 5.3c for different integrated systems perovskite-Mie sphere. Our data point out a large sensitivity in absorption measurement of single nano particle when Mie antenna are used. This can be explained as a nanoscopic effect in the near field: the dielectric nanoresonators act as a near field probe able to modify the excitation surface up till a hundred nanometers. Our findings are in agreement with reference [6] where a scanning near field optical tip replaces our Titania sphere in detecting a single molecule.

As conclusion, coupling perovskite nano-crystals with Titania spheres makes from one side the PL signals from perovskites stronger, from the other side allows for a great sensitivity in detecting the absorption of light from single PNC in the far field. This latter element has a particular relevance, since open the way of detection of single emitter in the far field in a relative simple experimental configuration.

5.2 Solid state dewetting combined with soft nano-imprint transfer

When approaching Mie resonators based nanophotonics for practical applications, the well-rounded physical device has to be considered, not only by looking at the single dielectric resonators, but also considering the surrounding medium as, for first, the substrate where it lies. We have already analyzed how high refractive index substrates influence the resonances of Mie particles, by spreading their full width half maximum and by slightly shifting their center wavelength (see section 1.3.1 and section 2.2).

In approaching Titania based Mie resonators, as the single spheres but also the ordered array described in chapter 3, the substrate doesn't constitute a significant limitation (see the argumentation in section 2.2, in particular fig. 2.5), as it consists

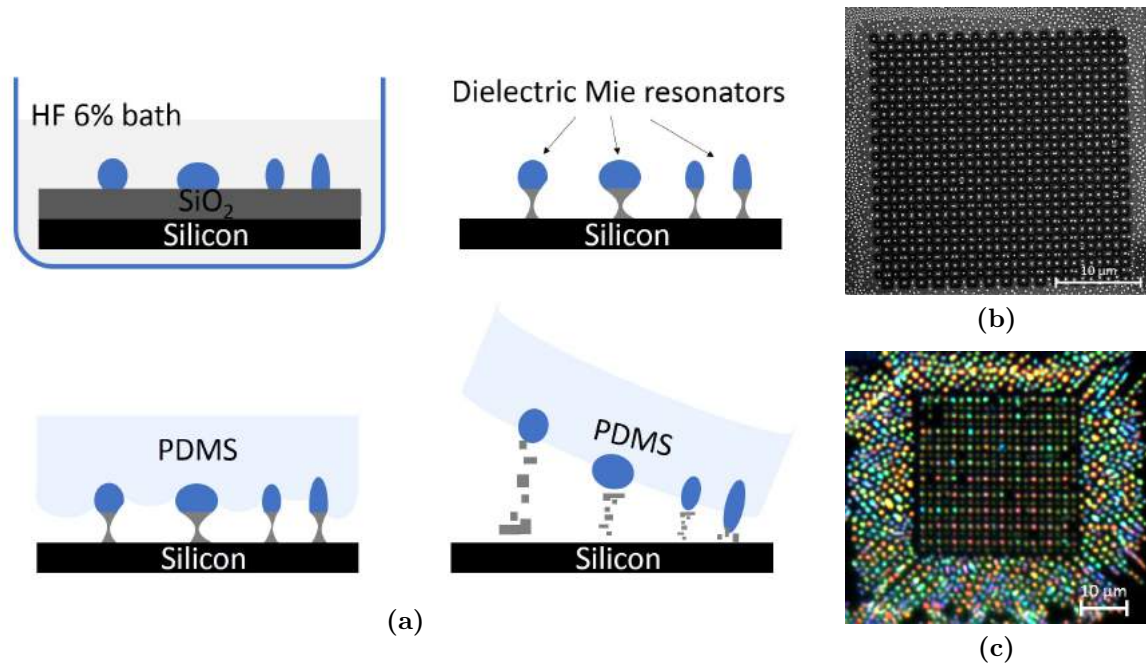


Figure 5.4: **a)** Chemical and mechanical procedure for transferring dewetted islands on a Polydimethylsiloxane (PDMS) substrate. **b)** SEM image of a dewetted sample before transfer on PDMS. **c)** Dark field image of the same sample after transfer on PDMS.

of glass. However, when other dielectric materials are explored, as e.g. silicon or germanium, different growing methods are used, that cannot be implemented on glass. We are speaking, for instance, of solid state dewetting.

Despite the several advantages offer by Titania, deeply analyzed in this dissertation, silicon and germanium, with their higher refractive index allowing for sharper resonances with respect to Titania, represent a more mature photonic platform. Moreover, the potentiality of solid state dewetting (SSD) in term of high-throughput, surface extension and control (when driven via etching techniques) constitutes a viable method for inexpensive and large scale fabrication of photonic systems. Consequently, we believe that trying to overcome the limitation of silicon substrate in silicon and germanium dewetted metasurfaces is a point of interest for several photonic applications.

Here we would address this challenge by proposing a method for transfer an ensemble of dielectric islands, obtained via SSD, on a soft substrate transparent to visible and near-infrared wavelength [7]. The transfer procedure is sketched in fig. 5.4a.

Starting from a dewetted sample, where usually a thin oxide layer stays in between Mie resonators and silicon wafer, the first step consists in removing the most of this

oxide by a chemical bath (hydrofluoric acid 6% for several minutes depending on the thickness of the oxide). At the end of this procedure, single Mie resonators rest attached to the silicon substrate only thanks to tiny columns of oxide. The next step consists in deposition of Polydimethylsiloxane (PDMS), a dense polymer dissolved in water. As the polymer dries (30 minutes at 750 °C), it results as a soft transparent layer on top of the sample and it can be removed from this, just by picking it up mechanically. During this step, the tiny columns of silicon oxide are supposed to break. At the end, in the new sample, dielectric Mie resonators are embedded in a soft transparent polymer matrix of PDMS. This can be applied to any dewetted metasurface and allow for a transfer of more than 90 % of the original dielectric structure on silicon wafer (see figs. 5.4b and 5.4c for a comparison between a sample before and after transfer on PDMS).

The samples thus obtained are suitable for different applications. During this thesis we started to exploit them as nano-antennas for third harmonic generation, taking advantages of the third order non linear susceptibility of silicon-germanium, as well as integrated with dye emitters.

Third harmonic generation (THG) phenomena are non-linear effects and, therefore, are commonly characterized by very low efficiency. A viable solution to observe such phenomena lies in enhancing the density of the electromagnetic field inside the non-linear material. In this perspective, Mie resonators constitute good candidates since the supported resonances offer the desired trapping of the electromagnetic radiation. Figure 5.5 shows a first proof of THG excited with a pulsed laser at 1550 nm from SiGe islands (the sample is analogue to the ones described in chapter 4), after transfer them on PDMS. Differences in intensities and in central wavelength take into account the different dimensions of the islands (and then different resonances supported) and the frequency dispersion of the pulsed source.

We then probed how these structures work as nano-antennas, by coupling them with dye emitters luminescent between 500 and 600 nm. The emitters, dispersed in buthanol solution, are spread on the sample via spin coating, leading a random distribution on the surface (optical image of the dried drop as result on the sample substrate is reported in fig. 5.6a). Lifetime measurements are performed on the sample covered with emitters.

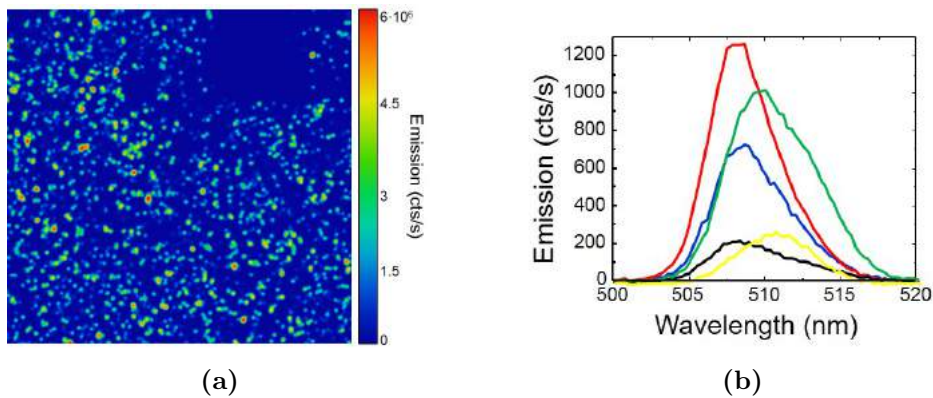


Figure 5.5: **a)** Map of THG signal coming from a sample of SiGe islands obtained via solid state dewetting and transfer on PDMS. **b)** THG spectra of single islands from the same sample in **a)**.

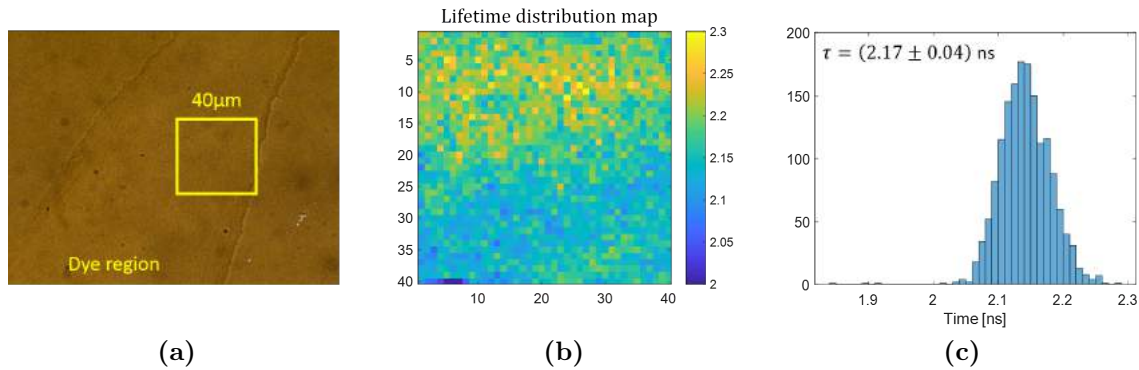


Figure 5.6: **a)** Optical image of a droplet of dye spin-coated on the sample. **b)** Map of lifetime signal coming from a sample of SiGe islands obtained via solid state dewetting and transfer on PDMS. **c)** Lifetime distribution from the map in **a)**.

Measurements of lifetime are shown in figs. 5.6b and 5.6c: statistic on them is obtained by doing a map of lifetime by scanning the relative position of the sample with respect to the laser source. As reference is taken a substrate of glass where a droplet of dye solution is spin-coated. The lifetimes distribution from different dye-covered areas on the reference sample doesn't present any variation with respect to the case of emitters on Mie resonators. The lack of lifetime reduction due to the Mie nano-antenna can be explained by the too high concentration of dye molecules within the detection spot, linked to the quite disperse distribution of Mie resonators. This can be easily seen also by looking at the map in fig. 5.6b, where the signal is uniformly distributed on the all area. Therefore, the resolution in the scan doesn't allow to resolve single emitter coupled with a resonators and lifetime measurements are mediated on more emitters,

the most of them not coupled with any SiGe island. To clarify this point more work is still needed, such as new experiments with different concentration of emitters in solution.

References

- [1] K. G. Lee, X. W. Chen, H. Eghlidi, P. Kukura, R. Lettow, A. Renn, V. Sandoghdar, and S. Göttinger. “A planar dielectric antenna for directional single-photon emission and near-unity collection efficiency”. In: *Nature Photonics* 5.3 (2011), pp. 166–169.
- [2] A. G. Curto, G. Volpe, T. H. Taminiau, M. P. Kreuzer, R. Quidant, and N. F. van Hulst. “Unidirectional Emission of a Quantum Dot Coupled to a Nanoantenna”. In: *Science* 329.5994 (Aug. 2010), pp. 930–933.
- [3] K. J. Vahala. “Optical microcavities”. In: *Nature* 424 (2003), pp. 839–846.
- [4] S. Checcucci, P. Lombardi, S. Rizvi, F. Sgrignuoli, N. Gruhler, F. B. Dieleman, F. S. Cataliotti, W. H. Pernice, M. Agio, and C. Toninelli. “Beaming light from a quantum emitter with a planar optical antenna”. In: *Light: Science & Applications* 6.4 (Dec. 2016), e16245–e16245.
- [5] V. S. Chirvony, S. González-Carrero, I. Suárez, R. E. Galian, M. Sessolo, H. J. Bolink, J. P. Martínez-Pastor, and J. Pérez-Prieto. “Delayed Luminescence in Lead Halide Perovskite Nanocrystals”. In: *The Journal of Physical Chemistry C* 121.24 (2017), pp. 13381–13390.
- [6] G. Zumofen, N. M. Mojarad, V. Sandoghdar, and M. Agio. “Perfect Reflection of Light by an Oscillating Dipole”. In: *Physical Review Letters* 101.18 (Oct. 2008).
- [7] M. Naffouti, R. Backofen, M. Salvalaglio, T. Bottein, M. Lodari, A. Voigt, T. David, A. Benkouider, I. Fraj, L. Favre, et al. “Complex dewetting scenarios of ultrathin silicon films for large-scale nanoarchitectures”. In: *Science advances* 3.11 (2017), eaao1472.

Conclusions and perspectives

This thesis showcased several aspects of all-dielectric photonic structures supporting Mie resonances accounting for their relevance as ultra-thin optical devices for applications at visible and near-infrared frequencies. Sub-micrometric particles featuring a sufficiently large refractive index and reduced absorption losses, can sustain electric or magnetic dipolar modes, quadrupolar modes etc., providing a distinct approach for light management in several contexts of practical interest such as structural color, directional scattering, sensing, dynamic color tuning and efficient anti-reflection coatings. However, despite the recent interest of the scientific community in this topic, several items rest still unexplored both in terms of applications and, above all, in terms of fabrication methods.

This thesis aims to overcome some limitations of the most common used fabrication methods exploited for realizing Mie resonators, as for instance the cumbersome and low-yielding lithographic techniques or reactive ion etching. Therefore, the challenge of this work was exploiting high-throughput, affordable and high reproducibility fabrication techniques and demonstrating the wide versatility of Mie resonators based devices to a wide plethora of photonic application in the optical range. To answer such requests we proposed three different all-dielectric structures realized thanks to three different fabrication techniques. Particular emphasis was devoted to establish performances and limitations of such techniques and devices, focusing the attention on their scalability and affordability for realistic exploitation. Thus, this thesis provides a first proof of concept of possible implementations of Mie resonators thanks to alternative fabrication solutions, that are aerosol deposition, sol-gel dip coating and nano imprint lithography and solid state dewetting, which do not suffer from the limitations of conventional top-down methods.

For each proposed technique we realized archetypal dielectric structures, starting from quasi-perfect Titania spheres, passing through record sized ordered arrays of Titania pillars and ending with silicon-germanium random metasurfaces. Thanks to the deep optical and morphological characterizations of such structures, their capability in light management is underlined and their suitability for photonic applications rises up. We demonstrated, to cite some examples, the possibility of active color tuning, band pass filters and anti-reflection coating just by modulating shape, size and material components of Mie resonators.

Other relevant applications for nano-photonics, such as optical antennas for single nano-emitters or third harmonic generation, have been addressed with encouraging results even more work is still needed to conclude the study.

In conclusion, we believe that our achievements could develop, in the mid term future, in several interesting directions. One example over many, is improving the combination of solid state dewetting and soft nano-imprint lithography over large scales. In fact, dewetted samples can provide large hard masters (up to 8 inches wafers) for soft nano-imprint lithography. This step will open the way to Mie resonators in real-life optical devices (e.g. anti-reflection coatings for solar panels and smart windows) as well as all-optical sensors (e.g. gas and pollution) when functionalising the sol-gel with proper surfactants.